Structure and Electronic Properties of Point Defects at Semiconductor Oxide Interfaces

Trinity College Dublin

Eric Mehes

October, 2015

Declaration

This thesis has been submitted to the University of Dublin for examination for the degree of Doctor in Philosophy by the undersigned.

This thesis has not been submitted as an exercise for a degree to any other university.

With the exception of the assistance noted in the acknowledgements, this thesis is entirely my own work.

I agree that the Library of the University of Dublin may lend or copy this thesis upon request.

Eric Mehes, October 2015

School of Physics,

University of Dublin,

Trinity College,

Dublin

Abstract

Semiconductor-oxide interfaces, particularly Si/SiO_2 and Si/HfO_2, are the centrepieces of transistor technology. Defects at such interfaces can massively affect device performance. Experimental studies on Si/SiO_2 and Si/HfO_2 interfaces accurately describe the structure of some of these defects, but the local atomic structure of others remains unknown. The exact positions of individual atoms at semiconductor-oxide interfaces can not yet be determined experimentally. Theoretical simulations are thus required to analyse the possible structural and electronic properties of the interface defects.

This work aims to answer two questions: which defects appear in $(001)Si/SiO_2$ and $(001)Si/HfO_2$ interfaces and what states do such structure produce in the band gap region of the structures. For this a mix of molecular dynamics and density functional theory methods were used to generate valid interface structures. Recurring interface defects were identified. The contribution of these defects to the total density of states of the structure was determined.

The most frequently occurring defect in the oxide layer of Si/SiO_2 interface structures were E'-type structures such as the ones previous studies observed in bulk SiO_2. The two recurring interface defects observed in this study were a dangling bond on a (2×1) (001)Si dimer reconstruction (dimer defect) and a threefold coordinated Si bonded to two substrate Si and one O from the oxide layer ("broken dimer" defect). Hydrogen passivation is extremely effective in removing the gap states of E' and dimer type defects, and moderately effective in removing the gap states caused by "broken dimer" defects.

For Si/HfO_2 structures the adsorption of O atoms at the silicon interface layer resulted in reducing the amount of gap states created by surface Si and surface Hf-Si bonds. The O adsorption at the interface led to a lower O coordination for Hf atoms within the bulk layer, which results in the creation of gap states by undercoordinated Hf atoms and Hf-Hf bonds.

While the Si/SiO_2 and Si/HfO_2 stacks used in this work are only simplifications of real life devices, it is reasonable to assume that dimer and broken dimer type defects described appear in semiconductor-oxide interfaces and are likely to have a role in phenomena such a near bias temperature instability. As SiO_2-free Si/HfO_2 stacks are being created, understanding the role of Hf-O coordination in creating gap states is needed. This work shows that at least a sixfold O coordination for Hf atoms is required to obtain a functional interface.

Acknowledgements

This work could have never been done without the professional and emotional support of the people that were by my side for these past few years. First, my supervisor Prof. Charles H. Patterson for his patience in offering guidance and advice. When looking for a PhD position abroad, finding a supervisor who is not just a good scientist but also a good mentor is a matter of luck, and I was indeed lucky to stumble under the supervision of such a person.

I would like to thank TCHPC and ICHEC for the computational resources provided. Alin deserves special thanks for being extremely helpful in helping me set up the needed software to run the calculations presented in this thesis. And the after work long discussions about politics were pretty nice too.

Working in front of a monitor in a gray dim-lit room for four years sounds like a dreadful experience, but it was far from it. People like James, John, Paul, Karaca and Pankaj made the office feel more like a second home. I would also like to thank the co-workers I didn't get to share an office with, Soumya and Aurab — their help is much appreciated.

My girlfriend Sissi, for being great and putting up with me during this time. I could have never arrived at this point in life without the support of loving family: Adalbert and Dorina, my parents and Donna and Sonja, my sisters.

Last but not least, the teachers that nurtured my interest in physics throughout the years — Mihail Szasz, Petrică Plitan and Vasile Chiș.

Contents

Chapter 1

Introduction

The invention of transistors by Shockley, Bardeen and Brattain in 1947 completely revolutionised computing, paving the way for ubiquity of digital devices in the modern world [1]. It is difficult to overstate the importance of transistors today. We do and will continue to rely on improvements in the design and manufacturing process of these fundamental units of computing as faster, smaller and more energy efficient transistors are required for our desktops, laptops, phones, television sets, cars, etc.

A transistor essentially functions as an on/off switch in circuits. Current through the source and the drain of the transistor can flow if a voltage is applied at the gate. Metal oxide semiconductor (MOS) transistors have a metallic contact applied on an insulating oxide gate layer, the oxide layer itself being sandwiched between the metal gate and the n or p-doped semiconducting substrate [2]. When a voltage is applied across the gate of the transistor a region known as the transistor channel enters a state known as inversion in which holes become the charge carriers in n-doped transistors and electrons in p-doped ones. Once the gate voltage is removed, the channel exits the inversion state and charge is no longer transported from the source to the drain.

Fifty years ago Gordon Moore made an observation that is now the driving force of progress in computing [4]. He observed that the number of transistors per microprocessor doubled essentially

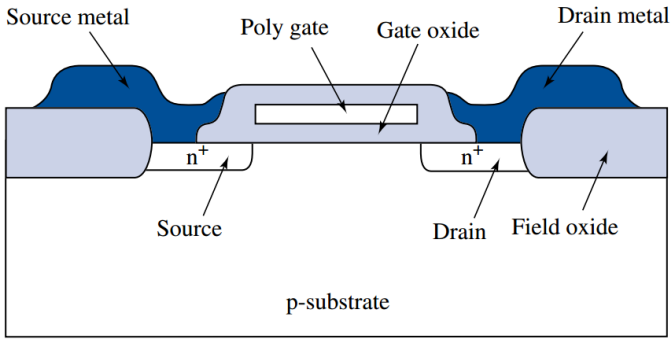

Figure 1.1: Transistor diagram for p-type substrates reproduced from Neamen [3]. By applying a threshold voltage on the polycrystalline Si gate an n-type inversion channel forms between the source and the drain, and current flows through it. In such transistors the gate oxide material choice is SiO_2 and the substrate is doped Si.

every two years. This continuous scaling resulted in the reduction of the oxide gate thickness. As the insulating oxide layer thickness decreases, electrons are more likely to tunnel through it, resulting in decreasing device performance.

For decades silicon dioxide[1] has been the main material used for gate oxides. In fact, it was the excellent qualities of silicon dioxide, which has a large band gap and a relatively defect and strain free interface with the (001) surface of Si that resulted in Si being the main semiconductor used in transistors today [5, 6] — virtually all other semiconductors have a rather poor native oxide. Using an amorphous oxide alleviates problems arising due to the lattice mismatch at the oxide-semiconductor interface.

The shrinkage of transistors implied a reduction of the SiO_2 layer thickness. This was made possible through advances in lithography, while the materials used in the fabrication of transistors have remained essentially the same. Silica-based gate oxide thickness reached its limit with the Intel 65 nm technology [7] where the SiO_2 oxide layer reached a thickness of 1.2 nm, less than five atomic layers thick. This also proved to be the limiting thickness for SiO_2 gates as leakage currents and loss of carrier mobility in the transistor became excessive [8].

[1] Also known as silica or SiO_2

A new paradigm for transistor gate design was needed and the search for alternative oxide metals began. Using a material with a high dielectric constant (high-k) decreases the likelihood of electron tunnelling — allowing the use of a thicker oxide while maintaining the capacitance of the gate [6]. Ultimately the research began to focus on hafnium dioxide[2] based materials [6]. Defect free interfaces with high-k materials were difficult to make, and phonon scattering affected carrier mobility in the substrate. Such problems were eventually eliminated with the Intel Penryn 45 nm technology introduced in 2007 [9, 10] — see Chapter 4 for further details on how common issues with the high-k oxide material were circumvented. Further progress came along in 2011 with the introduction of the Ivy Bridge 22 nm [11] transistor technology. This technology departed from the traditional 2 dimensional layered design of transistors shown in figure 1.1 towards a 3-dimensional structure. Recently the Intel Broadwell 14 nm transistor architecture was released [12], continuing Moore's law up to the present day.

Defects at oxide semiconductor interfaces and defects in the bulk of the oxide layers are responsible for pinning the Fermi level and affecting transistor performance [5]. The atomic structure of defects cannot be observed directly through experimental methods yet. Techniques such as electron paramagnetic resonance (EPR) measurements can give some insight to the properties of defects that have an unpaired electron spin [13]; capacitance voltage (CV) measurements can measure the charge trap density in structures, vibrational spectra can shed some light on the strains present at the interface and within the bulk of materials, and X-ray photoelectron spectroscopy (XPS) measurements can show the distribution of oxidation states at the semiconductor oxide interface layers [5].

Theoretical methods can provide a detailed description of the electronic properties of the defects in Si/SiO_2 and Si/HfO_2 structures [6, 14]. Molecular dynamics (MD) techniques can be used to create amorphous structures and reproduce the different crystallisation phases of oxides [15] and can handle systems containing several thousand atoms. However they cannot provide any information about the electronic properties of the systems simulated. Density functional theory (DFT) [16, 17] does provide information about the electron energy and distribution in the system, as well as a more rigorous first principles description of the interatomic bonding in the system. The

[2] Also known as hafnia or HfO_2

study of device-sized systems with DFT methods is computationally unfeasible at the moment.

This work aims to provide a description of the structure of defects appearing in Si/SiO_2 and Si/HfO_2 interfaces and to determine the gap states that are created by such defects. The existence of defect types at Si/SiO_2 interfaces not categorised in EPR measurements [18, 19] could influence processes such as fermi level pinning or near bias temperature instability [20]. Fermi level pinning is responsible for charge accumulation at the interface between the oxide and the semiconductor which effectively screens the electric field responsible for activating the transistor. Near bias temperature instability is a phenomenon causing an increase in threshold voltage due to the generation of defects at the surface and in the bulk of the oxide — the exact causes and phenomenology of negative bias temperature instability are still a matter of debate [20]. Interface defects in Si/HfO_2 interfaces have not yet been properly described through EPR methods, as the formation of a SiO_2 interlayer resulted in the detection of interface defects found in Si/SiO_2 stacks.

A mix of MD and DFT techniques was used to analyse the electronic properties of defects at semiconductor oxide interfaces by simulating Si/SiO_2 and Si/HfO_2 stacks. DFT studies on bulk Si/SiO_2 and Si/HfO_2 interfaces do exist (and will be addressed in chapters 3 & 4), and some even focus on interface and near-interface defects. Such studies generally take the approach of manually creating defects in structures rather than using MD and then observing the defects emerging after optimising the geometry of the structures at the DFT level of theory. The focus on observing defects that emerge from from simulations rather than manually generating possible defect structures is an approach that to the best of our knowledge has only been tried in bulk oxide systems [21].

Here we use molecular dynamics (MD) methods to generate the atomic positions of the oxide and density functional theory to optimise the geometry and extract the electronic structure properties of the structures. MD calculations can handle a rather large amount of atoms, whereas DFT calculations can quickly hit a computational wall when upscaling to large systems. In order to avoid this we simulate several small (< 200 atoms) structures, roughly $1 \times 1 \times 2$ nm in size. While a single such cell could present an arbitrary number of defects, repeating the calculation on several stacks gives us a glimpse of the typical defects that would occur. By imposing periodic boundary conditions on our calculations we effectively obtain two ~ 1 nm^2 interfaces per structure.

Obviously, the systems we obtain are only rough approximations to the real life atomic structure present in transistors. Structural parameters such as bond lengths and angles obtained from the MD run can be corrected during a DFT-level optimisation.

Calculations were done on the crystalline bulk cells of Si, SiO_2 and HfO_2 and on bulk cells for the amorphous oxides. The obtained results were compared with the existing literature on similar calculations. The method was validated and calculations on Si/SiO_2 and Si/HfO_2 interface structures were performed afterwards. By calculating the projected electron density of states for each atom in our structures we managed to identify the defects creating localised states in the gap region. Paramagnetic defects were identified the Fermi contact terms in the hyperfine Hamiltonian were calculated. Undercoordinated atoms in Si/SiO_2 interface structures were identified, and passifying hydrogen atoms were added — this allowed us to observe how the gap states of various defects change under passivation. In Si/HfO_2 the coordination of Hf atoms was identified and the contribution to gap states as a function of Hf coordination was analysed.

A brief summary of the theoretical concepts used in our calculations are presented in Chapter 2. The fundamentals of molecular dynamics and density functional theory are covered, as well as a short introduction to the calculation of the electron paramagnetic resonance isotropic and anisotropic hyperfine parameters.

The experimental and theoretical studies on the properties of Si/SiO_2 interfaces are reviewed in Chapter 3. Conflicting views by several authors as to the structure of various defects at the Si/SiO_2 surface and the SiO_2 bulk are, and how such defects interact with hydrogen are presented. Studies that discuss the interaction of bulk silicon dioxide and surface silicon defects in charge and hydrogen trapping phenomena are summarised.

Chapter 4 reviews some experimental and theoretical studies on crystalline and amorphous bulk HfO_2 and its interface with Si. Works dealing with the oxygen vacancy and interstitial defects in bulk amorphous and bulk crystalline hafnia are summarised. Theoretical studies on the coordination of Hf atoms in amorphous hafnia and the formation energies of oxygen vacancies in crystalline HfO_2 interfaces with Si are presented.

Chapter 5 presents results on the bulk properties of Si, SiO_2 and HfO_2. The structure of the amorphous phase of the oxides is also computed and its electronic structure is analysed. The conclusions are used in the analysis of the more complex Si/SiO_2 and Si/HfO_2 interfaces.

Chapter 6 presents the generation of Si/SiO_2 stacks and the calculations of the electronic properties of these structures. Recurrent defects and a few unique defects are identified and their electronic properties are analysed. The effect of hydrogen passivation on such defects is investigated.

Chapter 7 presents the calculations on structural and electronic properties of Si/HfO_2 interface structures. The effect of various degrees of coordination for Hf atoms in producing gap states in the Si/HfO_2 structures is calculated.

Finally our conclusions are presented in Chapter 8. The importance of this work is stated and eventual directions for future work are discussed.

Chapter 2

Theoretical Background

In this work we used molecular dynamics techniques implemented in the LAMMPS code [22] to generate the atomic position for the amorphous SiO_2 and HfO_2 oxides as well as to run a short geometry relaxation on the Si/SiO_2 and Si/HfO_2 stacks before optimising their geometry with density functional theory using the CASTEP code [23]. The hybrid DFT calculations were run on the resulting optimised structures with the local orbital CRYSTAL code [24]. Using the results obtained with CRYSTAL, the EXCITON code [25] was used to calculate the atom projected density of states for the bulk and interface structures. An overview of the basic principles of molecular dynamics, Hartree Fock and density functional theory follows.

2.1 Molecular Dynamics

Molecular dynamics (MD) is the simulation of the physical movement of atoms and molecules. The technique determines atomic trajectories by numerically solving Newton's equations of motion propagating under quantum mechanical forces [26]. Calculations can be made in the microcanonical ensemble, the canonical ensemble or the isothermal/isobaric ensemble. In the microcanonical ensemble the moles, volume and energy of the system are kept constant. The canonical ensemble

keeps the number of atoms, the volume and the temperature constant, i.e. the system is couplet to a thermostat. For the isothermal/isobaric ensemble a barostat is also coupled to the system to ensure constant pressure. All our MD calculations are done in the isothermal/isobaric ensemble – ensuring the equilibration of the temperature and the pressure in the system as the oxide deposition methods themselves require isobaric and isothermal conditions.

2.1.1 Basic Theory and Principles

For an atom i of atomic mass m_i at position $\mathbf{r}_i$ we have the relations

$$\mathbf{F}_i = m_i \mathbf{a}_i \tag{2.1}$$

$$\mathbf{a}_i = \frac{d^2 \mathbf{r}_i}{dt^2}, \tag{2.2}$$

where $\mathbf{F}_i$ is the force acting on atom i and $\mathbf{a}_i$ is its acceleration. Interatomic potential energy functions V are used to describe the two, three and four-body interactions, thus the force on an atom is described by

$$\mathbf{F}_i \equiv -\frac{\partial V}{\partial \mathbf{r}_i}. \tag{2.3}$$

The interatomic potential can be either a pairwise interaction such as a Lennard-Jones potential, or it can include bond angles, bond torsions or the Coulomb interaction of the atomic partial charges, q_i. The choice of the interatomic potentials is crucial in MD simulations, given that various potentials are created to reproduce different properties of various materials. We will also discuss many-body potentials, and describe the properties of the potential used in the simulations presented in this report.

In order to simulate a macroscopic system, we apply periodic boundary conditions (PBCs). However, it is impossible to observe some long range phenomena when using small cells. Such problems can occasionally be circumvented by simulating a very large cluster of atoms.

For studying the time evolution of a system for a time t equation 2.1 is integrated using an algorithm such as Verlet integration [27] or the Gear predictor-corrector technique [28]. In the case of the Verlet integration (used in this work) the position $\mathbf{r}_i$ of an atom i at time $t + dt$ is determined from its positions at time t and time $t - dt$ using the relation

$$\mathbf{r}_i(t + dt) = 2\mathbf{r}_i(t) - \mathbf{r}_i(t - dt) + \mathbf{a}_i(t)dt^2 + \mathcal{O}(dt^4), \tag{2.4}$$

which is simply a symmetric difference approximation to Newton's equations.

One may observe that the velocity $\mathbf{v}_i(t)$ does not appear in the previous relation. Velocities do not need to be computed in order to simulate the time evolution of a system since they cancel each other out in the Taylor expansion of $\mathbf{r}(t)$

$$\begin{cases} \mathbf{r}_i(t + dt) &= \mathbf{r}_i(t) + \mathbf{v}_i(t)dt + \frac{1}{2}\mathbf{a}_i(t)dt^2 + \dots \\ \mathbf{r}_i(t - dt) &= \mathbf{r}_i(t) - \mathbf{v}_i(t)dt + \frac{1}{2}\mathbf{a}_i(t)dt^2 - \dots \end{cases}. \tag{2.5}$$

Thermostats are used in MD to regulate the temperature of the system. Since temperature is obtained through averaging over the ensemble consisting of the configurations generated by the molecular dynamics simulation at each time step, temperature regulation is obtained by modifying the atomic velocities $\mathbf{v}_i$. In this work we use the Nosé-Hoover thermostat formalism [29, 30], which introduces an extra degree of freedom ζ to act as a heat reservoir

$$\frac{d\mathbf{r}_i}{dt} = \frac{\mathbf{p}_i}{m_i} \tag{2.6}$$

$$\frac{d\mathbf{p}_i}{dt} = -\frac{\partial V}{\partial \mathbf{r}_i} - \zeta \mathbf{p}_i. \tag{2.7}$$

For the reservoir we have the equation of motion

$$\frac{d\zeta}{dt} = g k_B T_0 \frac{1}{Q}\left(\frac{T}{T_0} - 1\right), \tag{2.8}$$

where g is the number of independent momentum degrees of freedom in the system, k_B is the Boltzmann constant, T is the system temperature, T_0 is the temperature of the reservoir, and Q is a parameter which determines the rate at which the temperature of the system T_0 will tend toward T.

Constant pressure is achieved using the Martyna-Tobias-Klein (MTK) [31] barostat which uses the equations

$$\frac{d\mathbf{p}_i}{dt} = -\frac{\partial E}{\partial \mathbf{r}_i} - \eta \mathbf{p}_i \tag{2.9}$$

$$\frac{d\eta}{dt} = V\frac{P - P_0}{\tau_p^2}, \tag{2.10}$$

where η is an extra degree of freedom associated with the volume change, P is the system pressure, P_0 is the imposed system pressure, and τ_p is a time constant that controls the relaxation strength of the system pressure.

The Nosé-Hoover thermostat and the MTK barostat allow us to perform calculations in the isothermal-isobaric ensemble (NPT), where the pressure and the temperature of the system are controlled, and other parameters such as the volume of the simulation box are allowed to relax.

2.1.2 Many-Body Potentials

For the last three decades there has been an ongoing effort to find more accurate potentials to describe many-body interactions [32, 15, 33]. While classic Lennard-Jones/Coulomb type pair potentials are still used for calculated properties of macromolecules, more refined potentials are needed in order to describe complex systems and phenomena. The Stillinger-Weber potential [34] was an initial success in finding a potential to describe silicon systems, which takes into account two and three body interactions. Since the potential was well parametrised, it was used for modelling a wide range of silicon structures and properties.

In order to better describe the elastic parameters of Si, Tersoff [35] introduced many-body inter-

actions to allow for the breaking of existing bonds and creation of new ones. A bond order and an electrostatic term with self consistent charge equilibration were added to the Tersoff potential by Yasukawa [36] to better model Si/SiO_2 systems. Many-body correction terms were added to the Yasukawa potential by Yu et al [37] to permit the modelling of Si interfaces with different silica polymorphs.

The charge-optimised many-body potential, COMB10, [38, 39] which is used in this report, was developed by Shan et al and replaced a point charge model with Coulomb integrals over the Slater $1s$ orbital and by treating electrostatic charges by using a real space Wolf summation method [40]. The functional form of COMB10 is

$$E_T = \sum_i \left(E_i^S + \frac{1}{2} \sum_{j \neq i} V_{ij}(r_{ij}, q_i, q_j) + E_i^{BB} \right) \tag{2.11}$$

where E_T is the total potential energy of the system, E_i^S is the self energy for atom i – specifically the energy required to form a charge, V_{ij} is the interatomic potentials for atoms i and j of charge q_i and q_j respectively, separated by a distance vector r_{ij}. E_i^{BB} is the bonding term for atom i. The term V_{ij} itself is the sum of three compontents: a short range repulsion term, U_{ij}^R, a short range attraction term U_{ij}^A, and a long range Coulombic interaction term, U_{ij}^I, which are defined as

$$\begin{aligned} U_{ij}^R &= f_{S_{ij}} A_{ij} \exp(-\lambda_{ij} r_{ij}) \\ U_{ij}^A &= -f_{S_{ij}} b_{ij} B_{ij} \exp(-\alpha_{ij} r_{ij}). \\ U_{ij}^I &= J_{ij}(r_{ij}) q_i q_j \end{aligned} \tag{2.12}$$

A_{ij}, B_{ij}, λ_{ij}, α_{ij} are functions of coefficients that are fitted (see [37] for further reference), $f_{S_{ij}}$ are cut-off functions dependent on the radius and a cut-off parameter, and b_{ij} is a bond order term dependent of the bond angle θ, and J_{ij} is the Coulombic integral over a $1s$ orbital of exponent ξ_i

$$J_{ij}(r_{ij}) = \int d^3 r_i \int d^3 r_j \frac{\rho_i(r_i, q_i) \rho_i(r_j, q_j)}{r_{ij}} \tag{2.13}$$

$$\rho_i(r_i, q_i) = q_i \frac{\xi_i^3}{\pi} \exp(-2\xi_i |r_{ij} - r_i|), \tag{2.14}$$

where ρ_i is the electron density of atom i. The self energy term is

$$E_i^S(q_i) = \chi_i q_i + J_i q_i^2 + K_i q_i^3 + L_i q_i^4 \tag{2.15}$$

with χ_i, J_i, K_i, and L_i fit to atomic ionization energies and electron affinities.

This variant of the COMB10 potential as implemented in the LAMMPS code [22] was used for the MD calculations in this work.

2.2 First principles methods

The nonrelativistic Hamiltonian for a system of interacting electrons and nuclei is

$$H = \sum_i T_i^e + \sum_I T_J^n + \frac{1}{2} \sum_i \sum_{j \neq i} V_{ij}^{\mathrm{ee}} + \frac{1}{2} \sum_I \sum_{J \neq I} V_{IJ}^{\mathrm{nn}} + \sum_i \sum_I V_{iI}^{\mathrm{ne}}, \tag{2.16}$$

where lowercase indices indices refer to electrons and the uppercase ones refer to nuclei. T is the kinetic contribution to the Hamiltonian and V^{ee}, V^{ne}, and V^{nn} are the electron - electron interaction, the nucleus - electron interaction and the nucleus - nucleus one, respectively. Obtaining an exact solution to this equation for systems comprised of more than a few atoms is not feasible, thus approximate solutions are needed.

The Born-Oppenheimer[1] approximation [41, p. 53] is the first step in reducing the complexity of the Schrödinger equation for a system of interacting electrons and nuclei. The approximation assumes that the wavefunction can be

[1] also known as the adiabatic approximation

$$\psi_{\text{system}} = \psi_{\text{electrons}}\psi_{\text{nuclei}}. \tag{2.17}$$

This approximation allows the problem of finding the ground state for the electron gas to be simplified by not taking into account the motion of the nuclei. The wavefunctions of these electrons are approximated by using linear combinations of either Gaussian functions or plane waves.

2.2.1 Hartree Fock Theory

The Hartree Fock method [42, p. 19] is a mean field technique, which approximates the effect the Coulombic electron-electron interaction by a mean field potential for the electrons.

An approximate electronic wavefunction for N interacting electrons can be chosen as a Slater determinant [43]

$$\psi_0 \approx \Phi_{SD} = \frac{1}{\sqrt{N!}} \begin{vmatrix} \chi_1(\mathbf{r}_1, s) & \chi_2(\mathbf{r}_1, s) & \dots & \chi_N(\mathbf{r}_1, s) \\ \chi_1(\mathbf{r}_2, s) & \chi_2(\mathbf{r}_2, s) & \dots & \chi_N(\mathbf{r}_2, s) \\ \vdots & \vdots & \ddots & \vdots \\ \chi_1(\mathbf{r}_N, s) & \chi_2(\mathbf{r}_N, s) & \dots & \chi_N(\mathbf{r}_N, s) \end{vmatrix}, \tag{2.18}$$

where $1/\sqrt{N!}$ is a normalisation factor and $\chi_i(\mathbf{r}_i, s)$ is a spin orbital for the electron i of coordinates $\mathbf{r}_i$ and spin s.

The one electron Fock operator f is

$$f_i = T_i + \sum_I V_{iI}^{\text{ne}} + \sum_j^N (J_j - K_j) \tag{2.19}$$

where J_j is the Coulomb operator

$$J_j(\mathbf{r}_1) = \left\langle \chi_j(\mathbf{r}_1) \left| \frac{1}{r_{12}} \right| \chi_j(\mathbf{r}_2) \right\rangle \tag{2.20}$$

It determines the electrostatic potential at $\mathbf{r}_i$ from the electron orbital χ_j. K_j is the exchange operator which is defined through its action on an orbital χ_i

$$K_j(\mathbf{r}_1)\chi_i(\mathbf{r}_1) = \left\langle \chi_j(\mathbf{r}_2) \left| \frac{1}{r_{ij}} \right| \chi_i(\mathbf{r}_2) \right\rangle \chi_j(\mathbf{r}_1) \tag{2.21}$$

The self consistent field method (SCF) requires finding the set of orbitals which minimise the total energy through solving the equations for a Slater determinant Ansatz, which leads to the following set of eigenvalue equations for the spin orbitals

$$f_i\chi_i = \varepsilon_i\chi_i. \tag{2.22}$$

According to the Koopman's theorem, ε_i are the ionisation energies for the electron on orbital χ_i.

2.2.2 Density Functional Theory

The electron density for a closed shell system

$$n(\mathbf{r}) = 2\sum_{i}^{occ} \psi_i^*(\mathbf{r})\psi_i(\mathbf{r}) \tag{2.23}$$

gives the electron probability density at position $\mathbf{r}$. The field of density functional theory relies on two mathematical theorems derived by Hohenberg and Kohn [16]:

Theorem 1 The external potential $V_{\text{ext}}(\mathbf{r})$ is determined within an additive constant by the electron density, $n(\mathbf{r})$.

Theorem 2 The ground state density is the density that minimises the total energy $E[n]$.

These two theorems, however, do not give any hints on how to calculate the electronic energy from the electron density $n(\mathbf{r})$. Kohn and Sham [17] showed that finding the electron density can be reduced to solving the set of equations

$$\left[-\frac{1}{2}\nabla^2 + \sum_I V^{\mathrm{ne}}(\mathbf{r}) + V_H(\mathbf{r}) + V_{XC}(\mathbf{r})\right]\psi_i(\mathbf{r}) = \varepsilon_i\psi_i(\mathbf{r}). \tag{2.24}$$

The first term in the Hamiltonian is the electron kinetic energy, the second one is the nucleus-electron Coulomb interaction and the third one is the Hartree potential defined as

$$V_H(\mathbf{r}) = \int \frac{n(\mathbf{r}')}{|\mathbf{r}-\mathbf{r}'|}d\mathbf{r}', \tag{2.25}$$

which describes the Coulomb repulsion of electrons. The last term V_{XC} is the functional derivative of the exchange correlation energy:

$$V_{XC} = \frac{\delta E_{XC}(\mathbf{r})}{\delta n(\mathbf{r})}. \tag{2.26}$$

The ground state density can be found with an iterative algorithm:

1. Select a trial density $n(\mathbf{r})$.
2. Solve the Kohn-Sham equations using a trial electron density to find the single particle wavefunctions $\psi_i(\mathbf{r})$.
3. Pre-calculate the electron density using these orbitals and Equation 2.23.
4. Compare the previous energy of the system with the newly obtained one. If they are identical return the ground state orbitals. If not use the density obtained from the Kohn Sham orbitals as the trial density in step 1 and repeat the sequence of steps.

It should be noted that no expression was given for E_{XC} in Equation 2.26, as the exact exchange correlation energy functional is not known, hence different routes towards approximating this term in DFT can be taken. In the local density approximation (LDA), the contribution of the exchange correlation energy E_{XC} from each infinitesimal volume $d\mathbf{r}$ is taken to be the value it would have if the whole of space were filled with a homogeneous electron gas with the same density as is found in $d\mathbf{r}$:

$$E_{XC}^{\mathrm{LDA}}[n(\mathbf{r})] = \int n(\mathbf{r})\varepsilon_{XC}[n(\mathbf{r})]d\mathbf{r} \tag{2.27}$$

where ε_{XC} which is considered to be the sum of the exchange and correlation energies ($\varepsilon_{XC} \equiv \varepsilon_X + \varepsilon_C$, where $\varepsilon_X = -(3/4)(3n(\mathbf{r})/\pi)^{1/3}$). Analytic expressions for ε_C are not known. This expression is local, as the value of E_{XC} here only depends on the value of the density in a given point. The local density approximation does provide reasonably good estimates for lattice parameters and energies, but tends to over-estimate bonding energies and doesn't perform particularly well on molecular systems [42].

A correction for the LDA treatment of the exchange correlation term is the generalised gradient approximation (GGA), which takes into account the gradient of the electron density

$$E_{XC}^{\mathrm{GGA}}[n(\mathbf{r})] = \int \varepsilon_{XC}^{\mathrm{GGA}}(n(\mathbf{r}), \nabla n(\mathbf{r}))d\mathbf{r}, \tag{2.28}$$

GGA type functionals do not always offer a clear improvement over LDA type functionals. For instance in the case of lattice constants determined by weak interactions pure LDA functionals trump GGA [44]. There is a wide variety of GGA functionals, some of the most popular ones being Perdew-Wang (PW91) and the Perdew-Burke-Ernzehof (PBE) [45] which we used in this report for optimising the geometry of our Si/SiO_2 and Si/HfO_2 structures. The approximation of the exchange correlation in DFT is known to result in underestimated band gaps for insulators but manages to obtain correct structural parameters [46] . While being less accurate in oxide band gap estimations than the hybrid density functionals discussed in the next section, the PBE functional is significantly less computationally expensive — and amorphous systems require hun-

dreds of geometry optimisation steps to reach a minimum structure, making PBE-level geometry optimisation an attractive computationally feasible option.

2.2.3 Hybrid Density Functionals

Hybrid functionals use both a portion of the Hartree Fock exchange mixed with the *ab initio* exchange correlation parameters. Starting from the adiabatic connection formula (or coupling constant integration formula) [47]:

$$E_{XC} = \int_0^1 E_{XC,\lambda} d\lambda \tag{2.29}$$

where $\lambda \in [0, 1]$ is a coupling constant that connects an interacting and a non-interacting system by replacing the Coulomb interaction by $\lambda/|\mathbf{r} - \mathbf{r}'|$. $E_{XC,\lambda}$ for a system whose external potential $v_\lambda(\mathbf{r})$ is adjusted to hold the electron density $\rho(\mathbf{r})$ fixed at its physical $\lambda = 1$ value is

$$E_{XC,\lambda} = \left\langle \Psi_\lambda \left| \hat{V}^{ee} \right| \Psi_\lambda \right\rangle + \frac{1}{2} \int d^3r \int d^3r' \frac{\rho(\mathbf{r})\rho(\mathbf{r}')}{|\mathbf{r} - \mathbf{r}'|} \tag{2.30}$$

with V^{ee} the electron-electron repulsion operator. At $\lambda = 0$ this equation represents the exact exchange of a Kohn-Sham non-interacting system. E_{XC} is thus an interpolation between the exchange only and the full correlated energies at a given density.

The most commonly used hybrid functional is the Becke 3 parameter Lee-Yang-Parr functional (B3LYP)

$$E_{XC}^{\mathrm{B3LYP}} = E_{XC}^{\mathrm{LDA}} + a_0(E_X^{\mathrm{HF}} - E_X^{LDA}) + a_X(E_X^{\mathrm{GGA}} - E_X^{\mathrm{LDA}}) + a_C(E_C^{\mathrm{GGA}} - E_C^{\mathrm{LDA}}), \tag{2.31}$$

with $a_0 = 0.20$, $a_X = 0.72$, and $a_C = 0.81$, these parameters were obtained by fitting experimentally measured ionisation energies. A full Hartree Fock treatment (i.e. $a_0 = 1.$) of the exchange

energy is avoided as HF and KS theories define exchange differently — as in Kohn-Sham theory the exchange is defined on a given density while the Hartree Fock density is evaluated on the orbitals. In this report we used the B3LYP — $a_0 = 0.2$, marked as B3LYP(20%) — functional to calculate the electronic properties of Si/HfO_2 structures, while for the Si/SiO_2 structures we used an Hartree Fock exchange mix $a_0 = 0.05$ — marked as B3LYP(5%). While initially designed for small molecules hybrid functionals also have been succesfully used in the study of a wide range of solids [48]. As it will be shown in Chapter 5, the B3LYP functional can provide a good estimate for the HfO_2 band gap, but over-estimates the bulk Si band gap by more than 60%. Choosing a 5% Hartree Fock mix returns a reasonable estimation for the bulk Si band gap, while under-estimating the band gaps of SiO_2 and HfO_2.

2.3 Electron Paramagnetic Resonance

In electron paramagnetic resonance (EPR)[2] measurements a sample is held in a magnetic field. The field induces a split in the spin up and spin down electron energy levels, while the absorption of microwave radiation is used to measure transition energies. By rotating the sample in the field observations can be made on the symmetry of the EPR active defect.

The hyperfine isotropic hamiltonian for the interaction between a nuclear and electron spin has the form[49]:

$$\hat{\mathcal{H}}_{\text{iso}} = \frac{2\mu_0}{3} g_e \beta_e g_n \beta_n \left|\psi(0)\right|^2 \hat{S}^T \hat{I} \tag{2.32}$$

where μ_0 is the vacuum permittivity, g_e and g_n are the electron and nuclear g factors, β_e is the Bohr magneton, β_n is the nuclear magneton, $|\psi(0)|^2$ is the electron spin density at the nucleus[3], and $\hat{S}$ and $\hat{I}$ are the electron and nuclear spin operators. The factor multiplying the $\hat{S}\hat{I}$ terms is known as the isotropic hyperfine coupling A_0, where

[2] Or electron spin resonance, hence the abbreviations ESR/EPR are used interchangeably

[3] Also known as the Fermi contact term

$$A_0 = \frac{2\mu_0}{3} g\beta_e\beta_n \left|\psi(0)\right|^2 . \tag{2.33}$$

For p, d or f orbitals the Fermi contact is essentially zero as these functions have nodes at the nucleus [50].

The anisotropic hyperfine Hamiltonian is defined as:

$$\hat{\mathcal{H}}_{\text{aniso}} = -\frac{\mu_0}{4\pi} g\beta_e g_n \beta_n \times \hat{S}^T \cdot \begin{bmatrix} \left\langle \frac{r^2-3x^2}{r^5} \right\rangle & \left\langle -\frac{3xy}{r^5} \right\rangle & \left\langle -\frac{3xz}{r^5} \right\rangle \\ & \left\langle \frac{r^2-3y^2}{r^5} \right\rangle & \left\langle -\frac{3yz}{r^5} \right\rangle \\ & & \left\langle \frac{r^2-3z^2}{r^5} \right\rangle \end{bmatrix} \cdot \hat{I} \tag{2.34}$$

In the equation above braces indicate an averaging over the spatial variables of the electron spin density. This term is the magnetic and dipolar coupling of electron and nuclear magnetic moments.

Chapter 3

Experimental and theoretical data on Si/SiO_2 interfaces

3.1 Introduction

An understanding of the Si/SiO_2 interface has been crucial for the development of transistor technology during the past few decades — its importance to the semiconductor industry has made it one of the most studied interfaces in condensed matter physics. In spite of the large number of published experimental and theoretical works on this system, a clear model of the bonding patterns and defect structures still has not been agreed upon [51]. The following sections will summarise X-ray diffraction studies that show that the SiO_2 layer is undoubtedly amorphous, and that bonds at the interface do not follow an ordered, predictable pattern.

This chapter will focus on summarising the conclusions of articles that deal with defects and sub-oxide distribution at the Si/SiO_2 interface. First some of the main experimental results on Si/SiO_2 interfaces will be covered. Core electron spectroscopy and electron paramagnetic resonance are the main tools used to probe the bonding arrangements and the properties of the defects observed in amorphous silica deposited on Si wafers. Theoretical work relevant to the calculations performed

in this work will be presented next; such work principally used molecular dynamics simulations and density functional theory calculations. Molecular dynamics is used to generate structural parameters similar to those obtained in atomic layer deposition and annealing procedures. Density functional theory is used to analyse the electronic properties of various atomic arrangements.

3.1.1 Experimental work

A large body of work exists around the nature of Si/SiO_2 interfaces as well as defects in amorphous SiO_2 and has been reviewed in [5, 13, 52]. EPR experiments detected the following paramagnetically active defects

- P_b-type defects — dangling bonds centred on tri-fold coordinated Si backbonded to Si atoms at the top-most Si monolayer. At (001)Si/SiO_2 interfaces two such defects have been identified, the P_{b0} and P_{b1}.
- E'-type defects in bulk SiO_2. The exact topological nature of these defects in amorphous Si/SiO_2 is still unclear [21] but they are generally formed by dangling bonds centred on tri-fold coordinated silica backbonded to three oxygen atoms.

Interface oxidation states and early models

The amorphous nature of the SiO_2 layer at the Si/SiO_2 interface has been proven through X-ray spectroscopy [5]. The topology of this interface is a problem that has been tackled both through experiment and *ab initio* and molecular dynamics calculations for several decades, yet a confirmed model of the bonding patterns at the interface does not exist yet [53, 51] — problem made more complex by the fact that different deposition techniques could result in different bonding patterns.

Extensive photoelectric electron spectroscopy studies on the oxidation states of (001) Si/SiO_2 and (111) Si/SiO_2 interfaces have been carried out by Hollinger and Himpsel [54]. In determining the ratio of Si^{3+}, Si^{2+} and Si^{1+} oxidation states they used core level photoemission with synchrotron

radiation to map the Si $2p$ and Si $2p_{3/2}$ core level energies. Whether amorphous SiO_2 was deposited on Si surfaces grown along the (001)Si or (111)Si directions, the relative ratio of $3+$, $2+$ and $1+$ oxidation states was the same — a ratio of $0.4 : 0.3 : 0.3$ for (001)Si, with only a slight increase in the Si^{3+} oxidation state for interfaces with the (111) Si surface. They also showed this ratio to remain relatively constant for SiO_2 layers of 5 Å, 7 Å and 11 Å, concluding that the general structure of the interface does not change as the thickness of the Si/SiO_2 layer is increased. Their follow up study in 1988 [55] gives the density of such intermediate oxidation states as $(1.5 \pm 0.5) \times 10^{15}\mathrm{cm}^{-2}$.

Electron energy loss spectroscopy measurements by Muller *et al* [56] show the thickness of the suboxide layer to be no larger than one or two monolayers thick by probing the oxygen K band edge. They also note that tunneling imposes an absolute minimum thickness for the oxide layer of 7Å and note that the gap states they observe could impact the performance of the MOSFET. The minimum oxide layer thickness was calculated by considering the decay length of Si states into the oxide, $t_{\min} = 6\lambda$ where $\lambda = \hbar/(E - E_C)$, E being the interface state energy and E_C the conduction band edge of bulk SiO_2. Another complementary paper by the same group [57] further cements their argument on the minimal SiO_2 oxide thickness. They point out that the reduced dielectric constant ($K = 3.9$) results in boron penetration, which itself leads to gate leakage currents and poor oxide reliability. They also note that some of the negative effects of overly thin oxide layer could be staved off by nitrogen incorporation. A theoretical study by the same authors is presented in subsection 3.1.2.

A vibrational study by Devine *et al* [58] compared the longitudinal and transversal optical (LO and TO) modes of the infra-red (IR) spectrum of SiO_2 deposited on Si wafers and concluded that the observed shifts in the absorption peaks can be mainly attributed to a change in stoichiometry at the interface region. They also estimated the thickness of this layer with modified stoichiometry to be around 16 Å — larger than the estimate of Muller *et al* mentioned in the previous paragraph — and the average stoichiometry in this region to be $SiO_{1.45}$.

The variation in the stoichiometry of the SiO_2 layer near the Si interface was also confirmed with IR spectroscopy carried out by Queeney and co-workers [59]. Basing their argument on the observed asymmetry of the redshift in LO and TO modes with decrease of the oxide thickness,

they concluded that the transition region from the top Si monolayer to the bulk phase of SiO_2 can be 6 Å deep into the oxide, estimate that falls between the previously mentioned studies of Muller *et al* [56] and Devine *et al* [58].

A 1993 study of Si/SiO_2 interfaces by Daum and co-workers [60] shows the importance of the interfacial layer in electron transitions. By analysing the vibrational spectra of amorphous SiO_2 deposited on Si wafers, they observed the existence of stretched Si-Si bonds at the interface layer. These stretched bonds cause a resonance at photon energies in the vicinity of 3.3 eV. Daum *et al* also point out that annealing moves the gap states of P_b-type defects towards the silicon conduction and valence band edges.

EPR studies on paramagnetic defects

Electron Paramagnetic Resonance (EPR) is an experimental technique used to probe paramagnetic defects. It consists of using a slowly varying magnetic field to induce a variation in the splitting of the up and down spin states of an energy level. An electromagnetic field in the microwave frequency range is used to cause the electron to resonate between the up and down levels. The g-tensors of defects can be measured by rotating the sample with respect to the applied magnetic field. Given that paramagnetically active states tend to be well localised, the symmetry of the g-tensor can offer insight into the symmetry of the paramagnetic defect that is being analysed.

Using Electron Paramagnetic Resonance on (001) Si/SiO_2 structures, paramagnetic defects have been found both at the interface as well as in the bulk oxide. Two main interface defects have been observed with EPR techniques, P_{b0} and P_{b1}, both $\bullet$ Si$\equiv$Si[1] dangling bonds [13]. The most common and well analysed defect is P_{b0}, which is known to be a dangling bond pointing in the $\langle 111 \rangle$ direction of the (001)Si surface. A strikingly similar defect to P_{b0} is the P_b defect in (111)Si/SiO_2 interfaces, but with the dangling electron perpendicular to the interface. The exact nature of the P_{b1} defect proved to be more problematic to determine experimentally, yet both defects are known to create states in the band gap of Si [61], their energies depending on the

[1] Notation represents a dangling bond on a Si atom trifold coordinated to other Si atoms

position of the Fermi level.

The generally reported densities for these defects are 5×10^{12} cm^{-2} for P_{b0} and 1×10^{12} cm^{-2} for P_{b1} [5] [62]. Lenehan and Conley [13] showed that there is a $1:1$ correspondence between the charge trap density D_{it} and the density of P_{b0} and P_{b1} defects. The average distance between P_{b0} defects at (001)Si/SiO_2 interfaces is around 2 nm [63].

EPR techniques have been used in the analysis of E' defects in oxides since the 1950s [64]. More than 15 varieties of E' defects have been identified in experimental measurements during the past 50 years [52]. One of the first generation mechanisms for E' defects was using neutron radiation to displace O atoms in the structure into interstitial positions, thus leaving a doubly positively charged defect. Experimentally, four main types of E' paramagnetic defects were found to be intrinsic to bulk amorphous SiO_2, E'_α, E'_β, E'_γ and E'_δ. Hyperfine isotropic A_0 parameters of E' defects range from 0.2 mT to 49 mT [65]. The exact structural paramenters of these defects are still debated [52], however candidate structures have been proposed. A model for the E'_γ structure is a puckered positively charged oxygen vacancy resulting in an O≡Si• $^{+}$Si≡O structure. E_β has similar spectroscopic features to E'_γ but hydrogen is thought to be found in the O vacancy region. E'_δ presents a ~ 10 mT hyperfine split, with the wavefunction of the unpaired electron being more delocalised. E'_α variants are stable only below 200 K and tends to relax to an E'_γ structure upon interaction with ambient light. Griscom *et al* [66] suggested that the 13 mT hyperfine splitting of E'_α defects could be caused by two-fold coordinated O=Si•• structure in a triplet spin state. Buscarino *et al* [65] attribute a 49 mT to E'_α defects and dispute the link between two-fold coordinated Si (O-Si-O bridges) and E'_α defects, as their relative concentrations in samples differ by approximately one order of magnitude. They also proposed a positively charged back projected (i.e. pointing away from the vacancy) sp^3 hybridised Si dangling bond as the main candidate for E'_α defects.

The P_{b1} defect has been analysed by Stesmans *et al* [62]. Through EPR spectroscopy they determined that the P_{b1} defect dangling electron orbital is pointing in the $\langle 211 \rangle$ direction, making a 35.26° angle with the $\langle 100 \rangle$ interface normal. They also point out that the dangling electron might also be a part of a surface Si dimer structure. Their results show that even on O enriched Si/SiO_2, oxygen and hydrogen are not a part of the immediate vicinity of the P_{b1} defect. The P_{b1}

defect is also more easily passivated than P_{b0}.

Further EPR studies on the P_{b1} defect were carried out by Campbell and Lenahan in 2002 [67]. They showed that it produces states predominantly in the lower half of the Si band gap. Their studies were done using corona charging, a process where charge is pumped into the system rather than simply applying an external potential difference, on a system with a 3.3 nm thick layer of amorphous SiO_2. They observed a narrower peak in the Si gap for P_{b1} defect than P_{b0} ones. Their hyperfine results are also in agreement with the previously mentioned studies of Stesmans *et al*. The positioning of the P_{b0} defect they provide in the band gap is in contradiction with older studies that place the defect's states either above the mid gap region [68] or studies that contend the P_{b1} defect is electrically inactive [69]. Campbell and Lenahan estimate the 0.3 to 0.4 eV energy difference between the peaks located in the Si gap locations of the positively and negatively charged P_{b1} defect.

CV measurements

The charge pumping technique [70] is used in capacitance voltage (CV) measurements to determine the trap density at semiconductor/oxide interfaces by measuring the substrate current of a transistor with grounded source and drain while uniform voltage pulses are applied to the gate. The charge trap density, D_{it}, can be measured through varying the base voltage of the pulses using the formula

$$D_{it} = \frac{I_{cp}}{qfA\Delta E} \tag{3.1}$$

where I_{cp} is the charge-pumping current, q is the electron charge, A the surface area, f is the pulse frequency and ΔE is the difference between the inversion Fermi level at different charged states of the interface [71]. While a charge trap density D_{it} can be estimated with the help of CV measurements, the technique cannot provide details about the chemical nature of these traps.

Early CV measurements on MOS structures with a 40–50 Å oxide thickness by Maserjian and

Zamani [72] showed that the majority of charge traps in their stacks were defects at the interface layer (< 20 Å). An analysis on the charge trap density of the (001)Si/SiO_2 interfaces was carried out by Witczak *et al* [73] using 5 different methods of charge-voltage (CV) measurements, measuring the different values for charge traps obtained under high and low frequency measurements, by estimating the conductance of the sample, measuring the slope of the drain current versus the gate voltage at subthreshold voltages, pumping charge to recombine with the majority carriers and in the last method they measured the difference in electron-hole recombination under different temperatures. They observed that the density of gap states tends to increase sharply around the band edges, predominantly near the conduction band.

Effect of hydrogen passivation

The pervasiveness of hydrogen in Si/SiO_2 structures has been known for a long time [74], the concentration of hydrogen in Si/SiO_2 stacks being around 0.1 nm^{-3} [75]. The exact range of effects hydrogen has on device performance is still a matter of debate [76] [77]. Both P_{b1} and P_{b0} interface defects can be passivated with hydrogen and the activation energy of the Si-H bond is known to be $E_a = 1.57 \pm 0.04$ eV for P_{b1} defects and $E_a = 1.51 \pm 0.04$ eV for P_{b0} defects [62].

Exposure of oxidised (100) Si surfaces to hydrogen and ulterior analysis through EPR measurements was carried out by Stathis and Cartier [18]. They showed that the P_{b0} defect is more easily produced yet harder to passivate by hydrogen. They also concluded that P_{b0} defects are chemically dissimilar to the P_b defects observed in (111) Si/SiO_2 interfaces, in spite of the similarity of the EPR g tensors. In the same work they also noted that the P_{b1} reaction to hydrogen passivation more closely resembles the P_b defects from (111) interfaces. This however was a puzzling result as P_{b0} and P_b defects were shown to be structurally similar — both are •Si≡Si structures with the dangling bond pointing in the $\langle 111 \rangle$ direction. Stathis and Cartier also support the idea that many interface defects are not P_b defects after all. This statement however is strongly contradicted by Lenahan *et al* [13], who cite problems such as the unreasonably high concentration of hydrogen used by Stathis and co-workers in their experiments and the tendency of hydrogen to dimerise at room temperature. Lenahan *et al* also point out the difficulty in generating P_b centres using the

element that passivates them and finally noting that the 10^{21} hydrogen atoms/cm^2 flux used by Cartier and Stathis is severely above the limits used for technologically relevant experiments.

Stesmans *et al* [69, 78] presented results on CV and EPR measurements on Si/SiO_2 interfaces, particularly relating to the EPR active P_{b0} and P_{b1} defects. H passivated defects were EPR activated through annealing at temperatures that ranged between 620°C and 1110°C. During the EPR measurements the magnetic field was applied perpendicular to the interface. They concluded that the P_{b1} defect has no major effect on the degradation of the interface following corona charging. They calculated the concentration of electrically active interface states after hydrogen passivation to be less than $3 \times 10^{10}/\mathrm{cm}^{-2}$. P_{b1} centre density increases linearly with respect to the annealing temperature. Unexpectedly, the density of P_{b0} defects remained constant regardless of the temperature at which the annealing process was carried out. The authors point out this could be due to the generation of different interface defects through the hydrogen passivation process. While P_{b1} and P_{b0} were identified as silicon dangling bonds, the atomic conformation of these defects could not be experimentally determined.

Following the results of Stesmans and Afanas'ev, a 2007 paper by Jin and co-workers [79] in which they studied the defect generation at the Si/SiO_2 interface via corona charging, confirms the role of protons in interface degradation, both through depassivating P_b-type defects and creating others. Jin *et al* used CV measurements to characterise the defect density D_{it} — a technique which unlike EPR is not restricted to paramagnetically active defects, however – as previously stated – it does not provide information about the atomic structure of the defects observed. A short anneal at 400°C restores the previous properties of the interface.

Negative Bias Temperature Instability

While known since 1966, negative bias temperature instability (NBTI) became a reliability issue for transistors only in recent years as their miniaturisation continued [80]. NBTI is an increase in the threshold voltage for switching and overall degradation in device performance in p-channel transistors generally attributed to interface and oxide charge traps created by a negative gate bias at an elevated temperature. NBTI is also observed as well in n-type MOSFETs under positive

bias, albeit to a lesser degree [80].

The process is thought to involve breaking of Si-H bonds at the interface, leaving dangling bonds and interface traps, the hydrogen being exchanged with defects within the amorphous SiO_2 layer. This could facilitate trapping of holes within the oxide. P_{b0} and P_{b1} defects seem to be a crucial part of this phenomenon [80]. The P_{b1} defect is electrically inactive at low temperatures. However, at room temperature such defects act as electrically active interface charge traps [67]. On the other hand the density of P_{b1} defects is much lower than that of P_{b0} ones, and thus they may play a smaller role in the charge trapping at the interface. The NBTI effect however is not strongly dependent on the hole density in the substrate semiconductor. The estimated density of Si-H broken bonds that contribute to NBTI is around $10^{12} - 10^{13}\mathrm{cm}^{-2}$, fully coordinated interface Si requiring 10^{15} bonds/cm^{-2}.

One explanation for the difference in NBTI for p-type and n-type MOSFETs includes hydrogen bonds with phosphorous and boron inside the bulk of the substrate, namely the difference between B-H and P-H bonding energies. These bonds are thought to break, leaving a H^+ ion that migrates to the interface and forms a bond with a hydrogen from a passivated Si dangling bond. This H_2 molecule diffuses into the oxide where it can passivate dangling bonds, effectively healing the NBTI. A second and more likely explanation for the difference in NBTI in p-type and n-type transistors could be the concentration of gap states generated by defects near the donor and acceptor states of the doping impurities of the substrate semiconductor. At flatband the p-type semiconductor has positive interface trap charge, unlike the n-semiconductor's positive charge. In both cases the charge of the oxide is positive, thus having an overall increased excess of charge contributing to NBTI in p-type MOSFETs. The link between the interface's P_{b0} and P_{b1} defects and the oxide's E' defects are also corroborated by Campbell *et al* [81].

Grasser *et al* [82] showed that the recovery from NBTI is caused by the charging of E' defects in the oxide layer. They demonstrated with the use of time dependent defect spectroscopy that the recoverable part of the near bias temperature instability is due to a thermally activated hole capturing mechanism by oxide defects. The charge trapping time scale constants of these E' defects varies with a several orders of magnitude, as the defect's geometry changes upon charging it. Such defects seem to be pre-existing and not created after the bias is applied.

The role of the E'-P_{b0} and E'-P_{b1} defect interaction in NBTI was investigated by Ryan *et al* [83] using EPR techniques. They showed that E' defects tend to form in the oxide layer when the interface is subjected to negative bias. This result was consistent with the recovery process in NBTI being linked to the annihilation of oxide trap holes as presented in the Grasser two stage model discussed in the previous paragraph.

3.1.2 Theoretical work

The earliest models for the Si/SiO_2 interface presented an abrupt transition from the bulk crystalline Si to SiO_2. Such models had to be reconsidered after the results of XPS experiments presented in the previous section. An intermediary model proposed by Ohdomari *et al* [84] took an interface SiO_x layer into account in the light of photoelectric experiments [54]. They used a continuous random network to generate the atomic positions of the oxide layer. Their proposed model is shown in figure 3.1. The model implies a roughness of the (001)Si surface, having pyramid-like (111) protrusions that bind to oxygens. They used a potential interaction to relax the positions of their initial ball-and-stick model and present their average parameters for the structure. The Si-Si bonds match the bulk value, while the average 109.45° O-Si-O angle they give is slightly smaller than the 111.32° value for α-quartz.

The Ohdomari model did not account for P_{b0} and P_{b1} defects or charge traps. More complex models have been proposed and advances in computer simulations in the 1990s and 2000s allowed for more theoretically complex descriptions of interfaces.

Molecular dynamics calculations

First principles molecular dynamics was used by Hybertsen *et al* [85] to simulate the oxidation of silicon at the interface. Their model included 6 monolayers of silicon and 8 monolayers of the tridymite form of SiO_2, with the periodic boundaries along the interface set to approximately 10 Å. A temperature gradient was applied to melt the tridymite layer, the silicon substrate being connected to a thermostat. In their structure they observed a threefold coordinated oxygen, which

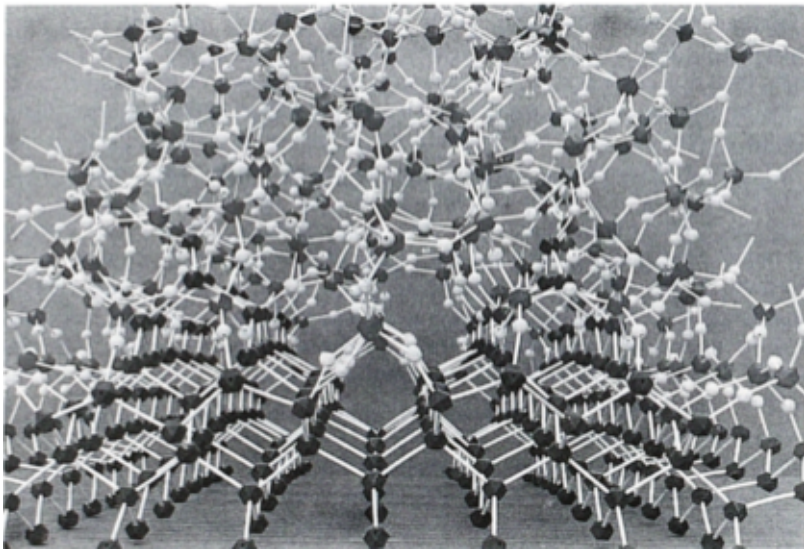

Figure 3.1: Model for the (001)Si/SiO_2 interface by Ohdomari *et al* [84]. This interface does not account for P_{b0} and P_{b1} defects.

caused a substantial rearrangement of the interface bonding pattern. This rearrangement resulted in an increased density of Si atoms near the interface layer, as oxygens adsorbed into Si-Si bonds at the interface get incorporated into the oxide (see figure 3.2). The processes they observed could explain the reduced stress observed at interfaces between crystalline Si and amorphous SiO_2 as opposed to the strain observed in interfaces with crystalline allotropes of SiO_2.

A 2007 paper by Yu *et al* [37] reported a molecular dynamics treatment of interfaces using a custom charge optimised many body potential (COMB07). They created a 15600 atom system, with $10\times10\times10$ conventional unit cells for the (001)Si slab and $3\times10\times10$ SiO_2 slab in its β-crystobalite form. They chose the β-crystobalite polymorph of SiO_2 instead of its more commonly used α-quartz structure in order to avoid dipolar effects arising from asymmetric interface structures.

Shan *et al* [39] did calculations with an improved COMB potential. COMB10 specially adapted for dealing with interfaces between amorphous SiO_2 and Si. Even more, defect vacancy formation energies determined with the COMB10 potential resemble those obtained with the help of DFT

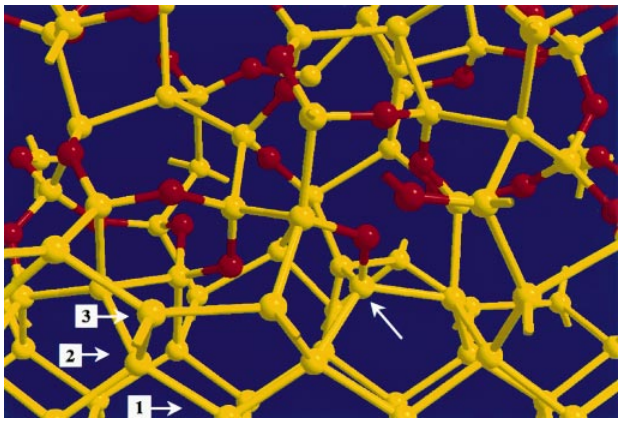

Figure 3.2: Snapshot of the structure obtained by Hybertsen *et al* [85]. Up to three monolayers of silicon are affected by bonding with the amorphous SiO_2. Arrows 1, 2 and 3 mark a substrate Si, a strained interface Si and a top monolayer Si$1+$ respectively.

calculations. They verified multiple possible contact geometries at the interface between α-quartz and Si. An energy minimisation was run for each of these possible geometries. The lowest energy minimised interface was then used in an MD constant pressure calculation, where the box size was allowed to change. It was first heated up to a temperature of 500 K for 12 ps, and then left to reach equilibrium for 8 ps at 300 K. The final charge distribution for this system is plotted in Figure 3.3. One may notice that both the Si substrate and bulk amorphous SiO_2 interface retain their usual charges, while charge redistribution does take place at the interface layer.

Interfaces between crystalline SiO_2 and Si

Buczko *et al* argued for an ordered oxidation (see figure 3.4) of the (001)Si semiconductor surface and the interface with the SiO_2 [86]. They inserted an oxygen atom in the bonds of the surface (2×1) dimer reconstructions in order to create a stable surface configuration. β-quartz, α-crystobalite and β-tridymite could be bonded to the checkered oxidation pattern, however only tridymite could form a bonding arangement with the row patterned oxidation state. Their ordered interface model accounts for the equal ratio of Si oxidation states at the vicinity of the interface.

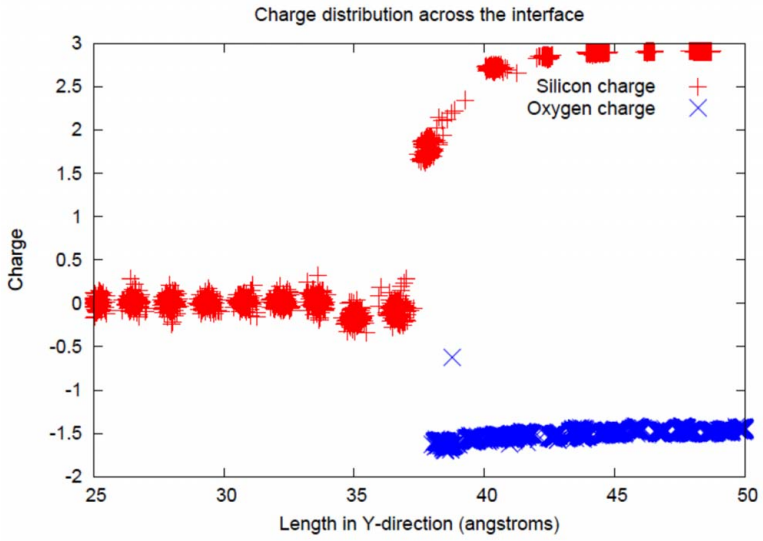

Figure 3.3: Charge profile for Si and O atoms in Si/SiO_2 systems according to Shan *et al* [39].

The authors also show that the introduction of oxygen in a suboxide Si-Si bond always lowers the energy per atom of the overall system – a mechanism that tends to make the Si/SiO_2 interface more abrupt and less prone to defects. The row pattern formation of O bridges inserted in Si surface dimer model of Buczko and co-workers is also supported by experimental IR data by Gurevich *et al* [87] on water molecules adsorbed on (001) 2×1 reconstructed Si surfaces.

The charge density of the interface proposed by Buckzo *et al* was analysed by Kutsuki *et al*. [88]. In their work, Kutsuki and co-workers used an α-quartz interface with a (001) Si slab. They subsequently removed one oxygen to obtain an interfacial defect and applied an external bias electric field to the structure. They observed that electrons localise around the interface in both, even for the defect free structure whether an external bias is applied or not. Kutsuki and co-workers also noticed that the existence of interface defects disrupts the charge density within the bulk of the Si and SiO_2 layers as well. Thus they conclude that interface defects decrease the effective oxide thickness (EOT) of the material and leakage currents by trapping charges.

The stability of oxygen bridges was further analysed in 2007 by Hemeryck *et al*, [89] both with

Figure 3.4: Row-patterned (a) and checkerboard-patterned (b) oxidation of a (001) Si surface as reported by Buczko *et al* [86]

density functional theory methods, as well as with scanning tunneling microscopy experiments. By calculating the energies of oxygen atoms in various positions near the SiO_2 layer, they showed that it is more energetically favourable by more than 0.15 eV for the oxygen atom to incorporate itself into the (2×1) Si dimer rather that one of the Si backbonds. They also mention that integration of O atoms into bulk Si requires a substantial rearrangement of the bulk atoms, thus making it more energetically favourable for the O atoms not to incorporate themselves in the deeper layers of the Si. The STM measurements they performed confirmed that O atoms favour clean 2×1 dimers or surface defects on adsorbtion.

First principles description of E' defects in bulk SiO_2

Boero et al [90] performed first principles LSDA calculations on the E_1' in α-quartz and the analogous E_γ defect in amorphous silica. They observed that an oxygen charged vacancy in α-quartz is stable in both a neutral and a charged state — a positively charged state favouring a

puckered configuration for the Si dangling bond. They observed a similar bistability in the charge states of the equivalent E'_γ defects in amorphous SiO_2. Their calculation of the hyperfine tensors on different atomic sites in the vicinity of the α-quartz E'_1 defect matches experimental values. They did not manage to obtain the same agreement with experiment for the equivalent E'_γ defect in amorphous SiO_2.

In a subsequent *ab initio* MD calculation Boero *et al* study [91] show E' centres can also appear in the absence of an oxygen vacancy in α-quartz. Through displacement an oxygen atom can reach a local energy minimum which causes a triplet-state sp^3 hybridised dangling bond to appear on the site of one of the Si atoms.

A recent theoretical study by Giacomazzi *et al* [21] on the E' defect reconsiders the paramagnetic behaviour of E'_γ defects, as well as considering several other type of E' dangling bonds found in amorphous silica. Through matching the computed g-tensors with values determined in previous experimental studies Giacomazzi and co-workers also assigned the E'_α defect to a forward oriented O≡Si• Si≡O defects. Their study rejects the assignment of the E'_γ defect to a dimerised Si-Si bond in the bulk of the SiO_2, but maintains it is an sp^3 hybridised Si≡O dangling bond.

First principles description of P_{b0} and P_{b1} centres

The P_{b0} defect had long been experimentally shown to be a threefold coordinated sp^3 bonded silicon pointing in the $\langle 111 \rangle$ crystalline direction [5]. A mechanism for the formation of these defects during the initial stages of (001)Si surface oxidation was analysed by Yamasaki *et al* [63] by starting from the previously shown inital oxidation model proposed by Buczko.

The atomic structure of the P_{b1} defect has been analysed by Stirling *et al* [92] using GGA DFT. In trying to determine role of oxygen — not directly bonded to the undercoordinated Si but part of the vicinity of the defect — in the data observed by Stesmans and his co-workers [69], they considered 3 main models for the P_{b1} candidate: a Si-Si interface dimer, an oxygen bridge between two silicon atoms and a Si-Si dimer between the interface and a •Si≡O with 2 oxygens bonded to the interface (see fig 3.5). They calculated the hyperfine tensors of the three systems and settled

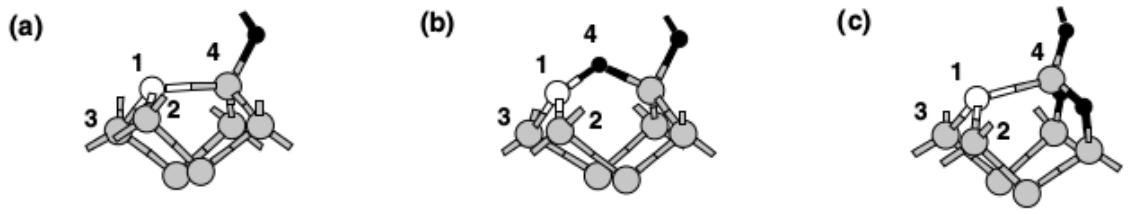

Figure 3.5: Relaxed models considered by Stirling *et al* [92] for the P_{b1} defect. The models are identified as (a) dimer (b) bridge and (c) asymetrically oxidised dimer. Based on their Fermi contact calculations, Stirling *et al* proposed the asymetrically oxidised dimer (model (c)) as the correct structure for P_{b1} defects. Oxygen atoms are shown in black, fully coordinated Si are shown in grey and 3-fold coordinated Si in white.

on the asymmetrically oxidised dimer as the model that best matches the experimental Fermi contact data. The models were considered by imposing 4 main constraints based on structural properties known from EPR experiments

(i) The defect has to be bonded to the Si substrate

(ii) The angle between the dangling bond and the interface must be near the value $32.3^\circ \pm 3^\circ$

(iii) Oxygen is not directly bonded to the P_{b1} Si

(iv) A near sp^3 configuration is expected

While the Si-Si dimer matched most experimental hyperfine parameters, the hyperfine axis angle of the asymmetrically oxidised dimer model matches the experimental 33° value. This model for the P_{b1} defect has since been referenced in following experimental works without being challenged.

Complex Si/SiO_2 cell models

The continuous miniaturisation transistors and consequently the shrinkage of the SiO_2 layer in Si/SiO_2 interfaces resulted in a significant increase of the computational power of computers. Thus it became computationally feasible to do *ab initio* calculations on Si/SiO_2 systems that can better describe the transistors used in the devices that run the calculations themselves.

Projected density of states calculations on the Si/SiO_2 interface by Neaton *et al* [93] showed that gap states are concentrated at the suboxide region of the interface and point out that interface specific states can be found as deep as 4-5 Å into the oxide. They emphasize the importance of second order neighbour arrangements on observing a more skewed projected densities of states profile.

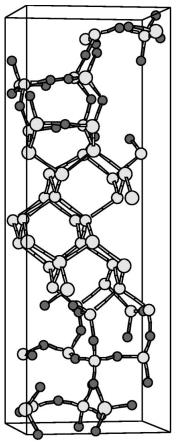

Figure 3.6: Model for the (001)Si/SiO_2 interface as suggested by Carrier *et al* [94] The cell contains 52 Si and 44 O atoms. Its dimensions are $7.67 \times 7.67 \times 24.62$ Å

The electronic structure of Si/SiO_2 using a 1.6 Å suboxide layer was investigated by Carrier *et al* [94] using the LDA functional and the frozen-core projected augmented wave (PAW) approach on models based on previous work by Pasquarello, Hybertsen and Car [85] — the cell can be observed in figure 3.6.

The structure was relaxed and the distribution of bond lengths was calculated, observing that Si-Si bonds tend to stretch near the interface region. The electronic contribution of dangling bonds was determined by removing the non-adsorbed oxygen from the structures and passifying the dangling bonds with hydrogen. They observed that the bandstructure of the stacked slabs (presented in figure 3.7) is rather similar to the bandstructure of the slabs with the

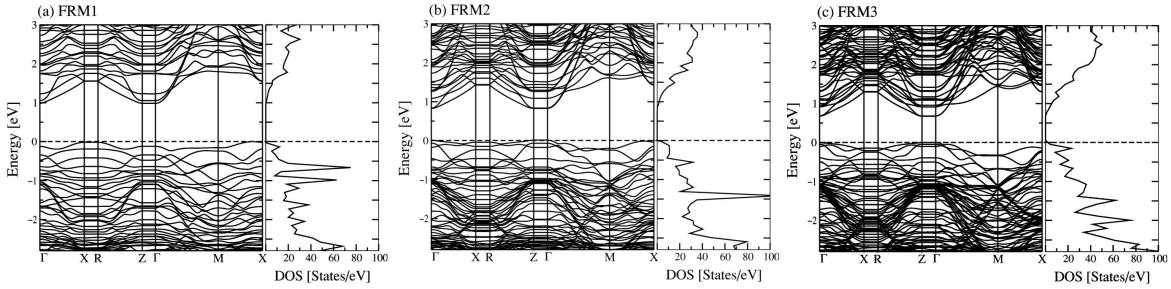

Figure 3.7: Bandstructures of Si/SiO_2 superlattices using LDA as presented by Carrier *et al* [94]. The thickness of the Si substrate is increased (52 Si atoms FRM1, 68 Si atoms FRM2 and 84 Si atoms FRM3)

shaved oxide layer — which led the authors to conclude that bulk oxide states have a minimal impact on the overall bandgap of the system. The authors also observed that the suboxide silicons have the effect of increasing the band gap and producing dispersionless valence bands. The values for the bandgaps of the fully relaxed models (FRM) are 0.99 eV, 0.81 eV and 0.68 eV for the first, second and third model respectively.

A simulation of a > 100 atom Si/SiO_2 stack was carried out by Giustino *et al* [95]. They used an MD quench to create an interface, and oxygens removed *a posteriori* from the interfaces obtained to replicate experimental results available in literature [78] [73]. Ion-scattering yields were calculated, which resulted in the selection of two main models that gave results similar to experimental data. Giustino and co-workers also note a high density of in-plane Si-Si interface dimers in the structures — such dimers have also been observed in the present work in the calculations on Si/SiO_2 structures presented in Chapter 6. For their further calculations, the periodicity of the structures was changed from 2D slab periodicity, to a superlattice with 3 dimensional periodic boundary conditions imposed. An extra layer of interfacial silica was added, and the system was relaxed a second time using molecular dynamics and the GGA Perdew-Wang functional. Structural properties of these final two models include a gradient in mass density that goes from 2.3 g/cm^{-3} at the interface to 2.1 g/cm^{-3} in the bulk silica, experimental X-ray reflectivity experiments show a density ranging from 2.4 g/cm^{-3} to 2.3 g/cm^{-3}. They calculated band offsets in the conduction band and valence band of the Si and SiO_2 layers for the two models and obtained the values 2.5

eV for ΔE_V and 1.8 eV for ΔE_C. The difference between the two values can be explained through the use of the GGA functional which is known to undersestimate band-gaps. The silicon induced states decay length was calculated to be 1.2 Å. By calculating the dielectric function of their structures they also noticed the partially oxidised Si atoms contributed to an enhanced dielectric constant around the interface layer.

NBTI in Si/SiO_2 stacks was modelled in a recent computational study carried on by Ling *et al* [96]. In their study they showed that E' centres can exchange H atoms with passified interface P_b-type defects. They started with a 3 nm thick Si substrate and a 216 atom amorphous SiO_2 layer, which was obtained through an MD simulation using the ReaxFF force field [97]. The resulting structure was optimised using the non-local HSE functional, which resulted in good agreement with experimental data for the band offsets and the band gaps of silicon and silica. By calculating the formation energy of Si-H bonds they observed that such bonds would require high temperatures to be dissociated. They also showed that if dissociated, the hydrogen from a Si-H bond within the bulk silica will bond to a two-fold coordinated O atom, thus forming a hydronium-like structure. Ling and co-workers also showed that the energy levels of neutral E' centres are strongly dependent on their position with respect to the interface.

The properties of hydrogen at the Si/SiO_2 interface were also analysed by Tsetseris and Pantelides [98]. They calculated diffusion barriers and reaction energies at the LDA and GGA level in order to determine the reaction path that leads to the passivation on P_b centres in (001)Si/SiO_2 interfaces. Tsetseris and Pantelides proposed a simultaneous breaking of an interfacial Si-Si bond and a dissociation of a hydrogen molecule as a mechanism for generating two interface Si-H bonds. They analysed both the passivation barriers of the P_{b1} models shown in figure 3.5. The calculated energies for H bond dissociation ranged from 0.1 eV to 0.9 eV. The high values of energy barriers obtained for H atoms near the interface layer would explain the thermal stability of hydrogen annealed devices.

	A_0	structure
P_b	11 mT	•Si≡Si in (111)Si/SiO_2
P_{b0}	9.6 mT	•Si≡Si in (001)Si/SiO_2
P_{b1}	12.7 mT	•Si≡Si in (001)Si/SiO_2
E'	43.9 mT	•Si≡O in SiO_2
E'_δ	12. mT	•Si≡O in SiO_2

Table 3.1: Experimental anisotropic hyperfine parameters (reproduced from Lenehan and Conley [13, p. 2051]) for various defects that appear in Si/SiO_2 interfaces or bulk amorphous SiO_2. The P_{b1} experimental A_0 value is taken from Stesmans *et al* [62].

3.1.3 Summary

A large body of work on bulk SiO_2 and Si/SiO_2 interfaces exists, but a consensus between theoretical and experimental works as to the exact structure of these defects has not been reached. The predominant defect in bulk SiO_2 are dangling bonds on Si back-bonded to three oxygen atoms. Two defects have been clearly identified by experimental works at (001)Si/SiO_2 interfaces: P_{b0} and P_{b1}, both Si dangling bonds direction back bonded to interface Si. The P_{b0} defect has its dangling bond along the $\langle 111 \rangle$ direction while the P_{b1} defect's dangling bond is along the $\langle 211 \rangle$ direction. Oxygen is known to be a part of the P_{b1} defect structure, but experiments do not give a clear picture how the full P_{b1} structural parameters. A theoretical model for the P_{b1} defect has been proposed, an asymmetrically oxidised Si dimer with two oxygen atoms adsorbed into neighbouring Si back-bonds. Table 3.1 shows the experimental anisotropic hyperfine parameters obtained in literature for defects in Si/SiO_2 interfaces and bulk SiO_2.

Chapter 4

Si/HfO_2 background

As mentioned in the previous chapter, scaling the thickness of the SiO_2 gate in Si/SiO_2 transistors results in electron tunneling through the oxide layer increasing too much for technological purpouses at thicknesses of 2nm [99]. Towards the early 2000s high capacitance (high-k) materials were considered for replacing it. A wide range of experimental and theoretical studies has been published on the properties of HfO_2 and HfO_2-based interfaces with Si in the last decade and a half. Such studies mainly focused on the effect of oxygen vacancies on the properties of bulk hafnia and Si/HfO_2 or SiO_2/HfO_2 interfaces [14] [100].

In MOSFET devices, the drain current depends on the capacitance of the gate which can be approximated as a parallel plate capacitor and thus described by the formula [6] [101]

$$C = \frac{\varepsilon_0 k S}{\Delta x}, \tag{4.1}$$

where ε_0 is the vacuum permittivity, S is the surface area, k is the dielectric constant (or relative permittivity) of the material, and Δx is the dielectric layer thickness. It can be seen in the previous equation that there would be three mechanisms of increasing the capacitance of a given transistor — decrease the oxide layer thickness, increase the surface area of the oxide-semiconductor interface

or use an oxide with a higher k constant. Increasing the surface of transistors would mean reversing the trend set by Moore's law, and the thickness of the SiO_2 layer is reaching its limit, thus the only available alternative is the use of materials with a high dielectric constant k. The effective oxide thickness (EOT) is used to describe the advantage of using a high-k material relative to an SiO_2 dielectric and is defined as [99]

$$\Delta x_{\mathrm{ox}} = \frac{3.9}{k} \Delta x_{\mathrm{hi}-k}, \tag{4.2}$$

where 3.9 is the dielectric constant of SiO_2, $\Delta x_{\mathrm{hi}-k}$ is the oxide thickness and k is the dielectric constant of the high-k material.

Huff *et al* [102] identified four main problems when looking for oxides suitable for high-k transitors:

1. Carrier mobility in Si can be reduced when using a high-k material
2. Scaling to a lower effective oxide thickness
3. Instabilities caused by the high number of defects in the gate oxides
4. Observed shifts in gate voltage thresholds

The carrier mobility in Si is lost due to the polarised nature of high-k materials — phonons scatter charge carriers in the conducting channel, i.e. remote Coulomb scattering. Defects at Si/HfO_2 interface pin the Fermi level and act as charge traps, which result in shifts in the gate voltage thresholds needed to operate the transistor. These problems were however circumvented by Intel in 2007 with the launch of their HfO_2-based 45 nm transistor family of Penryn processors [103]. Multiple high-k alternatives such as aluminium oxide (Al_2O_3), titanium dioxide (TiO_2), tantalum peroxide (Ta_2O_5), zirconium dioxide (ZrO_2) or zirconium dioxide (ZrO_2) were tried in the process [9]. Atomic layer deposition techniques were used to reduce the number of interface charge traps formed at the interface. The carrier mobility of the substrate problem was alleviated through the use of a metal gate, which help alleviate the reduction in channel mobility.

4.1 Experimental Work

Stesmans and Afanatas'ev carried out an EPR studies of Si/HfO_2 interface dangling bond defects [104] [105]. They observed both P_{b1} and P_{b0} defects at the interface. The g-tensor values they measured match the ones previously reported in Si/SiO_2 interfaces. Stesmans and Afanatas'ev observe a higher density of P_{b0} defects in Si/HfO_2 structures relative to Si/SiO_2 ones, which they point out could be due to the reduced exposure to hydrogen during deposition and nitrogen incorporation near the oxide-semiconductor interface. The responsiveness to hydrogen passivation of P_{b0} in Si/HfO_2 interfaces is similar to that observed in Si/SiO_2 structures — which Stesmans and Afanatas'ev mention points towards the formation of an intermediate SiO_2 layer. In the case of P_{b1} defects they note that the relative density of such defects does not vary significantly with the oxide used — Si/SiO_2, $(001)Si/AlO_3$ and Si/HfO_2 interfaces having similar densities of obtained P_{b1} defects. Stesmans and Afanatas'ev attribute this to P_{b1} defects being possibly located slightly below the interface plane. They also note that post deposition annealing significantly improves the quality of Si/HfO_2 structures. A later study by Fedorenko *et al* [106] confirmed the relative P_{b0} and P_{b1} densities in Si/HfO_2 structures.

Choi et al [107] studied the formation of transitional SiO_2 in $(001)Si/HfO_2$ interfaces between the hafnia and the semiconductor substrate. They suggest a temporary bonding between Hf and Si would act as a catalyst in the forming of the interfacial layer. By using X-ray photoelectron spectroscopy (XPS) to map the Si $2p$ and Hf $4f$ core level states in their structures, they detected signals of Hf-Si bonds as well as signals of Si-O bonding. Choi and co-workers estimate the thickness of the intermediate SiO_2 layer to be around 2 monolayers thick. The existence of the Hf-Si signal in the XPS measurements could indicate that the intermediate oxide layer formation is actually a form of hafnium oxygen silicate (HfO_xSi_x). Choi and co-workers also observed that oxygen adsorbed into the (001)Si interface does not instigate the formation of an interfacial SiO_2 layer, and as HfO_2 is thermodynamically stable with respect to Si, another mechanism must drive the spontaneous formation of the transition silica.

A study that combines experimental (XPS) and theoretical (DFT) techniques to investigate the band alignment of Si/HfO_2 interfaces was published by Puthenkovilakam *et al* [108]. They used

the LDA approximation to calculate a valence band offset of 3.04 eV and a conduction band offset of 1.54 eV between tetragonal HfO_2 and Si. They used the DFT density of states to fit the XPS data and extrapolated the new valence band offset to be 3.10 eV and the conduction band offset of 1.48 eV.

Modreanu *et al* carried out X-Ray, spectral ellipsometry, UV spectroscopy, IR and Raman studies HfO_2 thin films deposited on (001)Si [109]. They report a 5.51 eV band gap for amorphous HfO_2 and a 5.85 eV gap for HfO_2 that transitioned towards a crystalline (monoclinic) phase upon annealing. Through the use of X-ray diffraction Modreanu and co-workers showed that centres of crystalline nucleation are found in their deposited HfO_2 films, and observed a dependence for the crystallisation temperature on the film thickness — 20 nm films needing a $500°$C temperature to start crystallising while only a $450°$C annealing temperature is needed for 40 nm films. Upon annealing at $500°$C Modreanu *et al* observed a mix of monoclinic and cubic HfO_2 phases, even though in crystalline structures the cubic phase is a high temperature ($2700°$C) phase. The Raman spectrum they measured for monoclinic HfO_2 samples matches our own *ab initio* simulations (see chapter 5 section 5.3). Modreanu and co-workers also measured the Raman spectra of deposited Si/HfO_2 thin films and observed traces of the monoclinic HfO_2 phonon modes. By analysing the relative position of Si-Si vibration peaks in their Raman spectra they observe that tensile strain at the Si/HfO_2 interface could be induced through the HfO_2 crystallisation during the annealing process.

Kang, Lenahan and Conley performed EPR measurements on hafnia films deposited on (111)Si surfaces [110]. Their spectrum indicated the presence of O_2^--type defects. Their estimated density of such defects is 3×10^{12} cm^{-2}, out of which 10% would seem to be Hf^{3+}.

Wright and Barklie carried out EPR studies of defects in (powder) monoclinic hafnia [111]. γ radiation was used on the samples to induce a higher density of paramagnetic defects. They obtained three types of EPR spectra which they labeled as H1, H2 and H3. The H1 defect was stable while H2 and H3 decayed slowly at room temperature. Fig 4.1 shows the EPR spectrum they measured before and after exposing their samples to γ radiation. Wright and Barklie propose an Hf^{3+} d^1 state ion to be the main source of the H1 signal obtained. For the H2 signal they propose an oxygen vacancy with a trapped electron (i.e. an F^+ centre) — as the g tensor

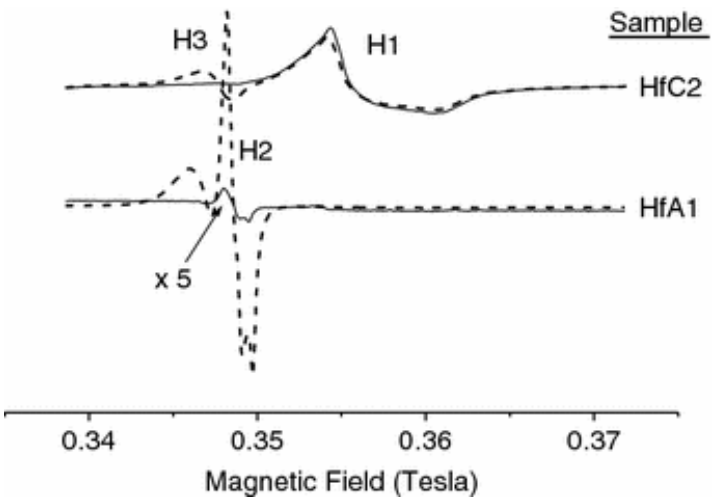

Figure 4.1: EPR spectrum for m-HfO_2 powders measured by Wright and Barklie [111]. The dotted line shows the spectrum after a γ-irradiation with 2040Gy. The non-irradiated HfA1 spectrum was scaled by a factor of 5. Three types of defects were identified — labeled as H1, H2 and H3.

components obtained for H2 defects more closely resemble those of a free electron than the components of an H1-type defect. They assigned the H3-type defect to an oxygen hole centre, due to the orthorhombic symmetry of the g-tensor. Wright and Barklie note that grinding the m-HfO_2 samples does not influence the density of observed H1 centres but increases the density of H3 centres, which would suggest that H3 is a surface-type defect. As the H1 density is unaffected by γ radiation, it is unlikely that such defects would act as charge traps, while H2 and H3 could be trapping centres.

Electrical and chemical beam evaporation was used to create HfO_2 thin films on (001) Si by Cherakoui *et al* [112] with an interfacial SiO_2 thickness of only 6 Å. They observed an increase in the effective oxide tunneling thickness of the HfO_2 layer after exposing the samples to argon. They also confirm that at Si/HfO_2 interfaces an intermediate SiO_2 layer forms spontaneously. Cherakoui and co-workers obtained a k-value of 21.2 for the hafnia layer and 6.3 for the interfacial silica layer.

Bersch *et al* used XPS and spectroscopic ellipsometry to measure the valence band and the

conduction band offsets in $Si/SiO_2/HfO_2$ stacks [113]. They observed band bending in the Si substrate in annealed stacks while no band bending was observed for the unannealed ones. They measured the Si/HfO_2 valence band offset to be 3.06 eV. Charging effects from the creation of holes due to the photoemission of electrons require a correction to be made to this figure — bringing the estimation of the Si/HfO_2 valence band offset down to the range 2.5 — 3 eV. Such a value is in agreement with ultraviolet photoelectron spectroscopy measurements, and Bersch and co-workers estimate this 2.5 — 3 eV valence band offset to be more accurate. The measured conduction band offset depended on the HfO_2 film thickness, 20 Å films having a conduction band offset of 1.77 eV and 30 Å films having a conduction band offset of 1.54 eV.

Another XPS study on $Si/SiO_2/HfO_2$ stacks was carried out by Wang *et al* [114]. They showed that a lower charge neutrality level of the HfO_2 layer results in electron transfer from the SiO_2 region towards hafnia, due to potential drops induced at the interface to align the Fermi levels in the three materials. Wang and co-workers note that $Si/SiO_2/HfO_2$ contacts obey similar principles to band alignment in semiconductor/semiconductor contacts.

Li *et al* studied the Si scavenging at the Si/HfO_2 interface which leads to the formation of an interfacial SiO_2 layer [115]. They deposited 2 to 5.5 nm SiO_2 films on (001)Si and 4H-SiC substrates and followed this by depositing $2 - 4.5$ nm thick HfO_2 films. XPS, TEM and AFM techniques were used to probe the thickness of the SiO_2 interfacial layer. They observed that Si atoms from the SiO_2 interfacial layer are scavenged into the HfO_2 layer upon annealing. Li and co-workers did not observe any Si scavenging from the Si substrate to occur. Their proposed mechanism for the observed effect is oxygen vacancy migration from the silica interlayer to the hafnia layer.

Quite recently Jamison *et al* have grown SiO_2-free (001)Si/HfO_2 interfaces through Hf physical vapour deposition and subsequent annealing [116]. They obtained 25 Å thick HfO_2 layers and after annealing the transistor leakage current dropped to 0.6 A/cm^2 (for comparison $Si/SiO_2/HfO_2$-stack transistors have a leakage current of 0.8 A/cm^2). Figure 4.2 shows the transmission electron spectroscopy (TEM) cross section image for the Si/HfO_2 stacks they fabricated. Figure 4.2 (c) shows the SiO_2-free (001)Si/HfO_2 stack profile. They used electron energy loss spectroscopy (EELS) to verify the absence of a silica interfacial layer by measuring the point of the O and Hf

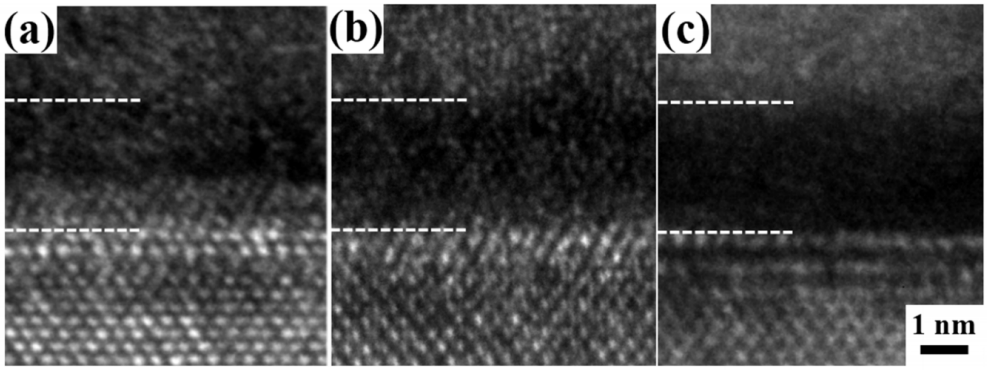

Figure 4.2: TEM images for (001)Si/HfO_2 stacks obtained by Jamison *et al* [116]. The dotted line marks the transition from crystalline to amorphous microstructures. The dark region shows the HfO_2 layer. Figure (a) 120s oxidation time (b) 10s oxidation time (c) 120s oxidation and annealing at 750° for 5 min. Figures (a) and (b) show the lighter intermediate SiO_2 layer, while figure (c) shows SiO_2 free Si/HfO_2 stack.

onset — where this onset was defined as the position where the maximum for the Hf and O EELS intensities reaches half of its value at the bulk HfO_2 position. For the stacks shown in figures 4.2 (a) the onset for the O signal is 12 ± 5 Å below the Hf onset point — which leads to the conclusion that an interfacial SiO_2 layer was formed in that region. For the structure shown in figure 4.2 (c) the onset difference between the O and Hf signal fell to 6 ± 5 Å. Jamison and co-workers observe that the annealed SiO_2-free Si/HfO_2-stacks would likely tend to crystallise in a high-k cubic or tetragonal phase due to the oxygen deficiency induced in the oxide layer. Through the EELS measurements the authors also concluded that during the annealing process Si atoms are integrated into the semiconducting substrate rather than being absorbed in the hafnia layer.

4.2 Theoretical Studies

DFT and molecular dynamics methods are generally used for the calculation of bulk HfO_2 and its interfaces. Such studies only began appearing in the past 15 years as HfO_2 became a more likely candidate for the choice of gate oxide material in the next generation of transistors.

4.2.1 Bulk Hafnia

Crystalline Hafnia

Foster *et al* used spin-polarised GGA calculations to analyse the properties oxygen vacancies and interstitials in crystalline hafnia [117]. For the analysis of defects they used a $2 \times 2 \times 2$ expansion of the 12 atom monoclinic unit cell. Oxygen was removed from or added to the resulting 96 atom system to form vacancies or interstitial defects. The effect on the total DOS is shown in figure 4.3. Foster and co-workers calculated the formation energies for such defects. They showed that incorporation of atomic oxygen is more energetically favourable than inserting O_2 molecular defects and also indicate that the stability of charged hafnia defects could result in interactions with image charges from Si substrates. They also showed that oxygen vacancies produce localised states in the Si valence band near the valence band maximum, while molecular oxygen defect states tend to lie deeper in the Si conduction band.

The charge transition levels of O vacancies and interstitial states relative to the bulk Si and HfO_2 band gaps were also studied by Xiong *et al* [118] using a screened exchange method and the weighed density approximation (WDA). The band gap obtained for m-HfO_2 with screened exchange is 5.75 eV and the one obtained with WDA is 5.9 eV. The transition levels for interstitial and oxygen vacancy defects obtained by Xiong and co-workers are not in agreement with the LDA results of Foster *et al*, placing the positively charged defect energy above the Si conduction band minimum. Xiong and co-workers support the idea that the O vacancy is the most important HfO_2 defect affecting device performance.

The spectroscopic properties of the oxygen vacancy defect were analysed by Muñoz Ramo *et al* [119] with the B3LYP functional. For this, an oxygen was removed from the 96-atom large $2 \times 2 \times 2$ expansion of the m-HfO_2 unit cell. An embedded cluster approach was used to calculate the properties of the vacancy. The B3LYP DOS for the various charged states of the oxygen vacancy calculated by Muñoz Ramo and co-workers is shown in figure 4.4 — the various charged states of the oxygen vacancy (V^{2-}, V^{2-}, V^{1-}, V^{0}, V^{1+} and V^{2+}) produce localised states in the m-HfO_2 band gap. Similar results were obtained by Broqvist and Pasquarello with the PBE0

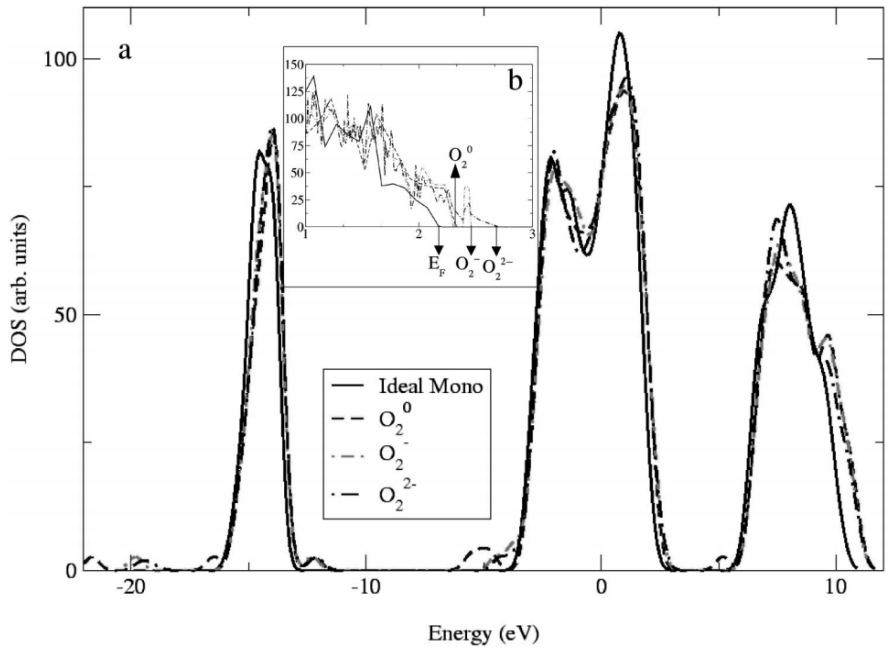

Figure 4.3: Influence of oxygen defects in monoclinic hafnia as calculated by Foster *et al* [117]. Inset figure shows the enlargement around the Fermi level (E_F). O_2^0 marks an introduced neutral oxygen molecule, O_2^- and O_2^{2-} mark its $(-)$ and $(2-)$ charged states. A 0.5 eV shift in the Fermi level is observed through adding a charged defect.

functional [120] — with mid gap states for the negatively charged vacancies and a near CBM gap state for the V^{2+} vacancy.

Wu *et al* used LDA approximations with Troullier Martins and Hartwigzen–Goedecker–Hutter correlation to calculate the elastic properties and Raman spectrum of m-HfO_2 [121]. The Raman intensities they obtained for the frequencies match the frequencies existing experimental data within 2.14%. The comparison between the results of Wu and co-workers and ours are shown in Chapter 5.3.

Amorphous Hafnia

Calculations on amorphous hafnia cells were also carried out in the past few years. Techniques range from classical to *ab intio* molecular dynamics, while the electronic properties of such structures are analysed with first principles DFT methods.

Kaneta and Yamasaki ran molecular dynamics simulations and first principles calculations on amorphous HfO_2 and analysed the formation energies of oxygen defects HfO_2 [122]. They used a 96 atom amorphous HfO_2 cell obtained through a classical molecular dynamics melt-and-quench technique. The cell was then optimised at the GGA level and its structural properties were computed. They obtained a density of 8.62 g/cm^{-3} for their structure and found the coordination for Hf atoms (2.35 Å cutoff radius) to be 5.7, lower than the coordination number of 7 obtained in monoclinic HfO_2. They also calculated the formation energy of an oxygen vacancy in this structure, and found it to range from 4.7 to 6.1 eV depending on the site location, with the most common value being 6 eV. Kaneta and Yamasaki also found that the formation energy of an oxygen vacancy in m-HfO_2 is independent of the density. As in the case of the m-HfO_2 study, Kaneta and Yamasaki showed that an oxygen vacancy creates a localised state in the middle of the amorphous HfO_2 band gap. For the incorporation energies for oxygen interstitials they found values lower than 0.2 eV, which are significantly lower than the incorporation energies of over 1.5 eV for oxygen in monoclinic and cubic hafnia [122].

Ab initio melt-and-quench MD was used by Scopel *et al* to generate the atomic structure of an

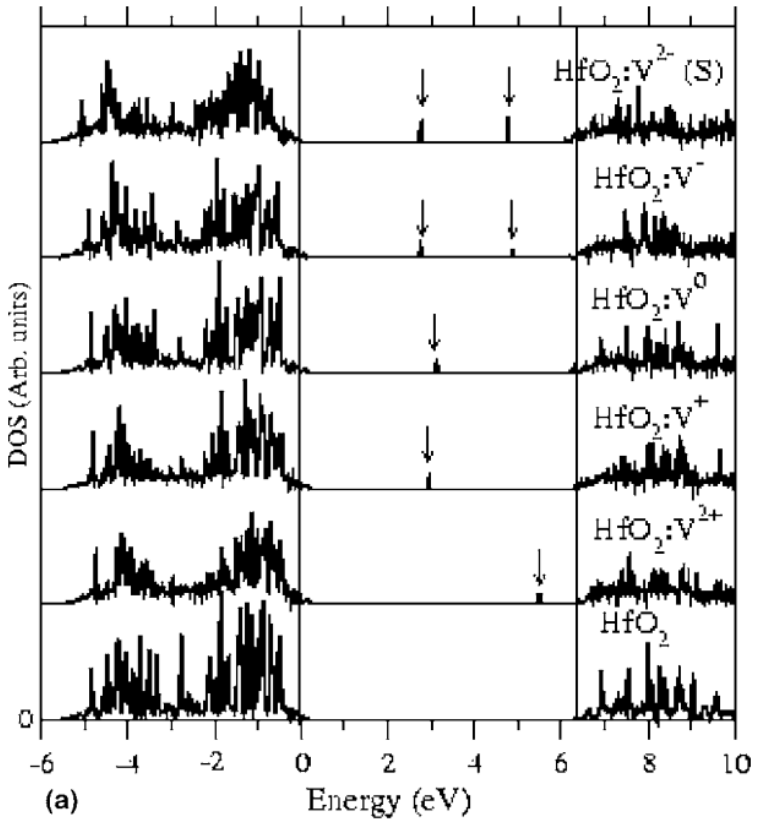

Figure 4.4: B3LYP density of states for the various charged states of of the m-HfO_2 oxygen vacancy as calculated by Muñoz Ramo *et al* [119]. While m-HfO_2 shows a clear 6.1 eV band gap, the oxygen vacancy produces a mid-gap state.

amorphous 96-atoms cell [123]. They calculated the pair distribution function and the coordination number for Hf atoms (2.5 Å cutoff for the coordination shell). The average coordination number for Hf they obtained was 7, while 6-fold and 8-fold coordinated atoms were found. Hf-Hf peaks in the pair distribution function were found in the range 3.3 — 4.0 Å. They note that, compared to monoclinic hafnia, the energy levels of oxygen vacancies are closer to the top of the valence band for amorphous systems. Scopel and co-workers also showed that the formation energy of oxygen vacancies is lower in amorphous systems than in m-HfO_2.

Another first principles study on the structural and electronic properties of amorphous HfO_2 were done by Chen and Kuo [124]. They generated their 96-atom cell using *ab initio* MD which was then optimised with the PBE functional. The pair distribution function and coordination distribution they obtained is shown in figure 4.5. For Hf-Hf pairs they observe a range between 3.0 — 4.3 Å and the average Hf coordination number they obtained is 6.1. A hybrid PBE0 level single point calculation was run for determining the electronic properties. The PBE0 band gap they obtained was 5.94 eV. They also showed that the (-2) charged state for the oxygen vacancy is stable and its chemical potential lies in the band gap.

Broglia *et al* determined the coordination and pair density distribution for amorphous HfO_2 through classical MD methods [125]. They chose structures containing a total of 1500 atoms ranging in density from 8.60 g/cm^{-3} to 11.50 g/cm^{-3} . Broglia and co-workers showed how through increasing the HfO_2 density localised Hf-Hf peaks in the range 3.3 — 4.3 Å of the pair distribution function fuse into one wider peak in the 3.0 — 4.2 Å region. They also showed that the diffusion of O atoms is affected by the density of the HfO_2 layer, the denser structure having a lower diffusion constant.

4.2.2 Si/HfO_2 Interfaces

First principles calculations with the Perdew-Wang functional (PW91) on the (001)Si/HfO_2 interface were done by Gavartin, Fonseca, Bersuker and Shluger [126]. Rather than creating the coordinates of the HfO_2 layer through molecular dynamics models, they chose to model the atomic layer deposition of monoclinic hafnia on a (2×1) reconstructed Si surface. They showed that

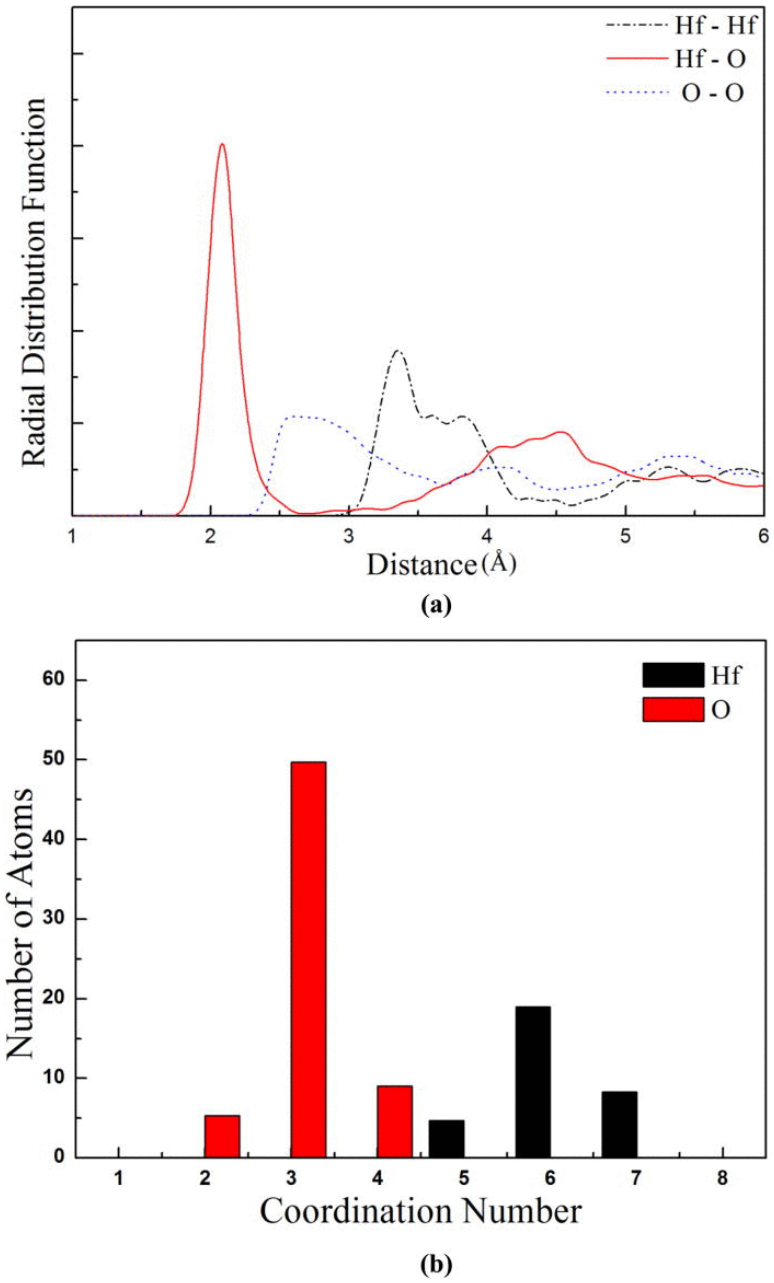

Figure 4.5: Pair distribution function and coordination barchart for amorphous HfO_2 as obtained through *ab initio* MD by Chen and Kuo [124].

oxygen incorporation into Si-Si bonds is exothermic while incorporation into the bulk hafnia is endothermic — which indicates interstitial oxygens from m-HfO_2 are likely to migrate towards the Si substrate and form an intermediate SiO_2 interface layer. Gavartin and co-workers also note that oxygen vacancies in the Si-O-Hf interface site have the lowest formation energy, which could result in the formation of interface Si-Hf bonds that create a state above the Si valence band maximum, if doubly charged.

Bonding patterns at the Si/HfO_2 interface were analysed with the PW91 functional by Peacock *et al* [127]. They used doubly interfaced cells with 25 — 47 atoms to match crystalline cubic HfO_2 cells. Non-polar (oxygen terminated) and polar (Hf terminated) faces of hafnia were considered. For a (2×1) reconstructed cell, interfaces with bivalent and trivalent oxygen atoms at the interface are stable, while metal (Hf) terminated interfaces were found to be metallic. Interface Hf-Si bonds create a state 0.3 eV below the bulk Si conduction band and pin the Fermi level.

Ab initio molecular dynamics techniques were used to model the interface layer between amorphous HfO_2 and the (2×1) reconstructed (001)Si interface by Hakala *et al* [128]. They observed that interface Si tended to adsorb the oxygen from the hafnia layer for a non-stoichiometric hafnia, leading to the formation of Hf-Si bonds and intermixing HfO_2, SiO_2 and hafnium silicate phases at the interface. Hakala and co-workers did not observe a strong tendency for interface reconstruction when using stoichiometric HfO_2, however the abundance of 4 and 5-fold coordinated Hf atoms resulted in a significant number states localised in the Si gap region. Adding saturating oxygen clears the gap states, bur not states near the Si VBM and CBM. By calculating the formation energy of an oxygen vacancy at different sites they conclude that such vacancies would likely migrate towards the interface layer. They estimated the tunnelling current to be around 10^7 A/cm^2, several orders of magnitude larger than the tunneling currents observed experimentally — which could be an artefact of a high defect rate and an underestimated band gap caused by use of the PBE functional.

Gavartin and Shluger ran *ab initio* calculations on a $Si/SiO_2/HfO_2$ stack [129]. Silica was manually added on top of a (001)Si surface, annealed by MD, followed by addition of a layer of monoclinic hafnia. Upon optimisation at the GGA level, oxygen diffused from the hafnia layer, but the vacancy sites were identified and oxygen atoms were added manually — which also resulted in the hafnia

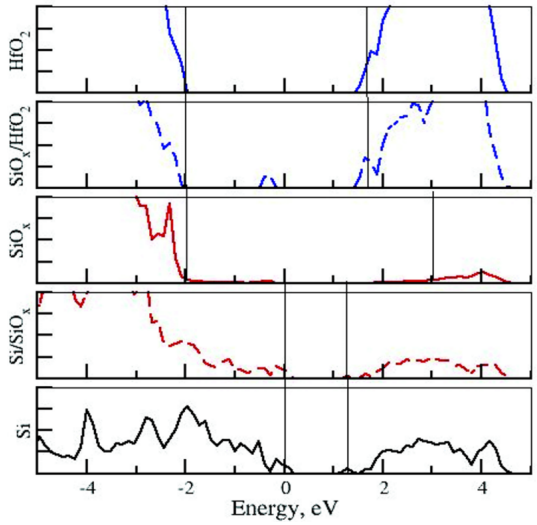

Figure 4.6: GGA-level layer projected density of states breakdown calculation on $Si/SiO_2/HfO_2$ by Gavartin and Shluger [129].

layer turning amorphous. The resulting structure had three bulk layers (Hf, SiO_2 and HfO_2) and two transition layers (SiO_x and SiO_x/HfO_2). The contribution to the density of states of each of the respective layers is shown in figure 4.6. The gap state seen in the SiO_x/HfO_2 region corresponds to a Hf-Si bond and its localisation beneath the bulk Si VBM is in agreement with the previously discussed study of Gavartin, Fonseca, Bersuker and Shluger [126]. A distribution of 6-fold, 7-fold and 8-fold coordinated Hf atoms is present in the HfO_2 layer, with a slight predominance of the 6-fold coordination.

Hydrogen states and band offsets in $Si/SiO_2/HfO_2$ stacks were analysed by Godet *et at* [130]. By calculating the formation energies of H, H^+ and H^- at different sites in the amorphous region, Godet and co-workers showed that H^+ is more likely to attach to oxygen atoms while H^- has an affinity for Si bonds, and its lowest energy is as a bridging hydrogen between two Hf atoms. Calculating the chemical potential of $(-)$ and $(+)$ charged states of the hydrogen atom they found that H^+ is the most stable state — and it tends to localise predominantly in the interface two interface regions (Si/SiO_2 and SiO_2/HfO_2). In the Si/SiO_2 region the proton induces the formation of threefold coordinated O atoms which act as charge traps.

Tang and Ramprasad used the PW91 functional to analyse the migration of O defects Si/m-HfO_2 stacks from the hafnia layer towards the interface, [131]. They showed that in the absence of oxygen at the interface Si-Hf bonds of ~ 2.6 Å will be created. Tang and Ramprasad calculated the driving force for segregation experienced by an oxygen vacancy to be approximately 1 eV. This driving force is maintained if other oxygen vacancies are induced in the structure. They also confirm that O interstitials are likely to accumulate near the interface region where they could form an interfacial SiO_x layer.

Ryu and Chang studied defects at the (001)Si interface with crystalline and amorphous hafnia and their effect on Fermi level pinning [132]. They used *ab initio* MD to generate the amorphous hafnia layer which was then manually added onto a (001) Si surface with additional oxygen atoms added to the interface. For the m-HfO_2 structure they used the slab geometry stretched to match the Si lattice. GGA-level DFT was used to calculate the electric properties of the structures. Ryu and Chang showed that removing the oxygen atom from a Si-O-Hf structure results in a charge transfer from the Hf d orbital to the Si dangling bond orbital. The GGA gap for the Si/amorphous-HfO_2 structure they obtained was 1.02 eV for six bulk Si layers and 0.74 eV for twelve bulk Si layers (for reference the GGA gap of bulk Si is 0.61 eV). They showed that Si dimers in structures with amorphous HfO_2 form a defect level -0.04 eV below the Si CBM — which makes dimers act as electron traps in n^+ electrodes.

4.2.3 Summary

In summary no clear consensus exists about the nature of defects at Si/HfO_2 interfaces. Experimentally P_b-type defects have been observed at Si/HfO_2 interfaces via EPR — but at an interface that contained an intermediate SiO_2 layer. EPR spectroscopy studies on bulk amorphous HfO_2 fail to provide an accurate description of the defects encountered, but it is likely such defects involve a Hf^{3+} ion.

The various band-gaps obtained from first principles studies on monoclinic hafnia are shown in table 4.1. *Ab initio* studies on interface structures between Si and amorphous HfO_2 with no interfacial layer have not been published yet to the best of our knowledge. Studies on the interface

	Functional	E_g band-gap
Zhao [133]	LDA	3.9 eV
Zhao [133]	GW_0	5.9 eV
Komsa [134]	PBE	4.34 eV
Komsa [134]	HSE06	5.98 eV
Komsa [134]	PBE0	6.75 eV
Exp [135]	N/A	5.9 ± 0.5 eV

Table 4.1: Band gap values reported in literature for m-HfO_2. The experimental HfO_2 band gap measured by Cheynet and co-workers is shown for reference.

	Cut-off radius	Density	Hf coord no	Method
Broglia *et al* [125]	N/A	11.50 g/cm^{-3}	7.63	MD
Broglia *et al* [125]	N/A	8.60 g/cm^{-3}	6.13	MD
Chen and Kuo [124]	2.5 Å	8.63 g/cm^{-3}	6.10	*ab initio* MD
Scopel *et al* [123]	2.5 Å	N/A	7	*ab initio* MD
Kaneta and Yamasaki [122]	2.35 Å	8.62 g/cm^{-3}	5.7	MD

Table 4.2: Density and average Hf coordination number at various cut-off radii as reported in theoretical studies on amorphous HfO_2. In m-HfO_2, Hf atoms are seven-fold coordinated within a radius of 2.35 Å.

between (001)Si and m-HfO_2 have focused on oxygen-vacancy defects. Such studies also show that Hf-Si bonding at the interface results in the generation of metallic states. Molecular dynamics calculations on bulk amorphous hafnia result in different estimations for the Hf-O coordination number, estimations that depend on the density chosen for the amorphous layer — but generally this coordination number varies from 6 to 8. The result from some of these studies is summarised in table 4.2. The coordination for an Hf atom in bulk monoclinic HfO_2 is 7 for a radius of 2.35Å.

Recently a usable transistor interface between Si and amorphous HfO_2 with no intermediate oxide layer has been engineered. In this thesis we performed calculations to determine the defects in such interfaces and presented the results in chapter 7.

Chapter 5

Bulk Si, SiO_2 and HfO_2 calculations

Predictions of DFT methods used in this work for bulk properties of Si, amorphous and crystalline SiO_2 and amorphous and crystalline HfO_2 are described in this chapter. These properties include lattice parameters, band gaps and vibrational frequencies. The calculations reported here are a benchmark for judging the accuracy of the methods applied to complex Si/SiO_2 and Si/HfO_2 interfaces.

The properties of the bulk components of Si, Si/SiO_2 and Si/HfO_2 materials were analysed. The structures were optimised with hybrid functionals for smaller systems and the more computationally inexpensive PBE functional was used to optimise larger and amorphous systems. Molecular dynamics techniques were used to generate the coordinates for amorphous systems. The principles of Hartree Fock and DFT theory were introduced in Chapter 2 section 2.2. In equation 2.31 the a_0 parameter is set either to 0.05 to obtain the B3LYP(5%) functional or at 0.20 to obtain B3LYP(20%). While yielding accurate band gaps for certain materials hybrid functionals lack a general accuracy when it comes to predicting the band gap of materials [136] [137]. Increasing the percentage of Hartree Fock exchange mix in hybrid functionals results in an increase in the calculated band gap of the analysed material. As it will be shown in the following sections, different percentages of Hartree Fock mix in the B3LYP functional results can either match the experimental band gap of the bulk semiconductor or the experimental band gap of the bulk HfO_2.

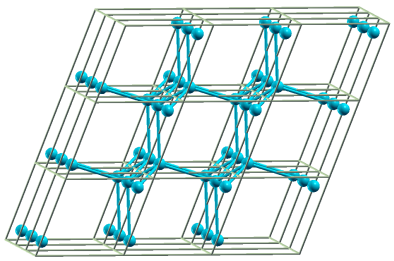

Figure 5.1: 3×3 expansion of the Si bulk cell. The primitive cell lattice parameter for the B3LYP(5%) optimised cell is 5.50 Å (density 2.232 g/cm^{-3}) and for the B3LYP(20%) optimised one 5.44 Å (density 2.266 g/cm^{-3}). The experimental lattice constant is 5.43 Å [140].

5.1 Bulk Si

The fundamental Si cell (figure 5.1) was optimised using a a hybrid functional as implemented in the CRYSTAL code [24]. A full electron basis set [138] was used to describe the Si electron behaviour. A 5% and a 20% Hartree-Fock exchange mix — marked as B3LYP(5%) and B3LYP(20%) — were considered for the optimisation. The aim of this calculation is to check the relative validity of using these functionals in determining bond lengths and bands gaps of Si. For this the cell dimensions were allowed to relax and a $24 \times 24 \times 24$ Monkhorst-Pack grid [139] was used.

A geometry optimisation was run using both the B3LYP(5%) and the B3LYP(20%) functionals. The use of the B3LYP(5%) functional results in a 2.39 Å equilibrium Si-Si bond length. For the structure optimised with the B3LYP(5%) functional a Si-Si bond length of 2.37 Å was obtained. Both lengths slightly overestimate the experimental value of 2.352 Å [140]. The density of states was calculated for the fundamental cell calculated with the B3LYP(5%) and B3LYP(20%) functionals respectively, the result is shown in figure 5.2.

The energy gap value for the structure optimised with B3LYP(5%) is 1.08 eV. Using the B3LYP(20%) functional a gap value of 1.76 eV was obtained. The experimental value of bulk Si is 1.11 eV [141].

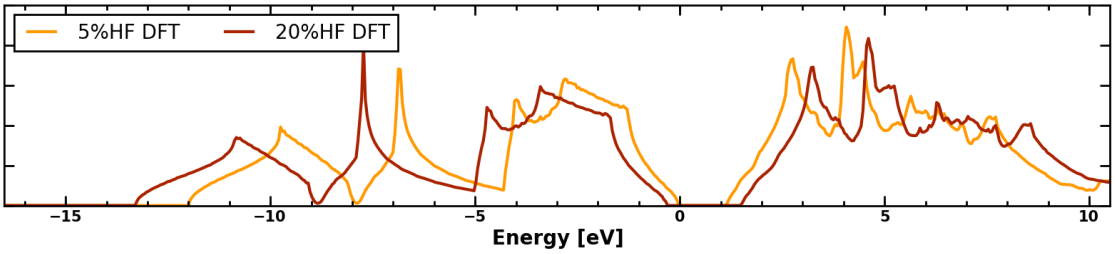

Figure 5.2: Density of states for the Si fundamental cell. The B3LYP(20%) calculation results in an over-estimation of the Si bandgap by 61% (see table 5.1). The band gap obtained with the B3LYP(5%) functional under-estimates the Si band gap by 2.7%. The zero level was set at the valence band maximum obtained with the B3LYP(5%) functional.

A summary of the band gap and lattice parameter results obtained is presented in table 5.1.

	B3LYP(5%)	B3LYP(20%)	Exp
Si-Si bond length	2.382 Å	2.370 Å	2.352 Å [140]
Error	1.29%	0.78%	N/A
Band gap	1.08 eV	1.76 eV	1.11 eV [141]
Error	2.7%	61%	N/A

Table 5.1: Si-Si bond length, band gap and error values obtained for bulk Si.

The density of states for the structure obtained with the B3LYP(5%) functional will be used as a reference in the analysis of Si/SiO_2 interfaces (chapter 6), as it offers a better approximation for the bulk Si band gap. The density of states for the structure obtained at the B3LYP(20%) level will be used as reference in the analysis of Si/HfO_2 interface structures (chapter 7) as SCF calculations for HfO_2-based structures proved difficult to converge — yet the B3LYP calculations on HfO_2 yield better estimations of the band gap.

5.2 Bulk Silica

Hybrid DFT calculations on α-quartz and amorphous phases of SiO_2 structure were done. The α-quartz geometry was optimised with both the B3LYP(5%) functional and the B3LYP(20%) one. The larger amorphous structure (see figure 5.4) was optimised with the more computationally inexpensive PBE functional, and a single point B3LYP(5%) calculation was run on the PBE-optimised structure. An all electron basis set [142] was used to describe the electron orbitals of oxygen in the SiO_2 structures.

5.2.1 Quartz

The geometry for a conventional 18 atom α-quartz cell was optimised with hybrid B3LYP(5%) and B3LYP(20%) functionals using the CRYSTAL code [24]. The two optimised cells were very similar structurally and in reasonable agreement with experimental data. The Si-O bond lengths of the cell optimised with the B3LYP(5%) functional relaxed at 1.626 Å. For the B3LYP(20%) optimised cell the Si-O bond length relaxed at 1.617 Å. These values are in agreement with the experimental 1.61 Å Si-O bond lenghts in silica [143]. For both structures the Si-O-Si angle optimises at 157°, which is 9% larger than the experimentally obtained value of 144° Si-O-Si angle for α-quartz [143]. The calculated densities for the two obtained structures were 2.304 g/cm^{-3} for the 5% and 20% Hartree Fock mix optimised structure and 2.338 g/cm^{-3} for the B3LYP optimised one. This underestimates the experimental density of 2.66 g/cm^{-3} [144] by roughly 13%.

The density of states of α-quartz was computed both the structure obtained with the B3LYP(5%) functional the one obtained with the B3LYP(20%) functional. The result in shown in figure 5.3. A 6.29 eV band gap was obtained for the structure optimised at the B3LYP(5%) level and a 8.05 eV gap for the structure optimised at the B3LYP(20%) level. Both under-estimate the experimental value of 9.65 eV [145].

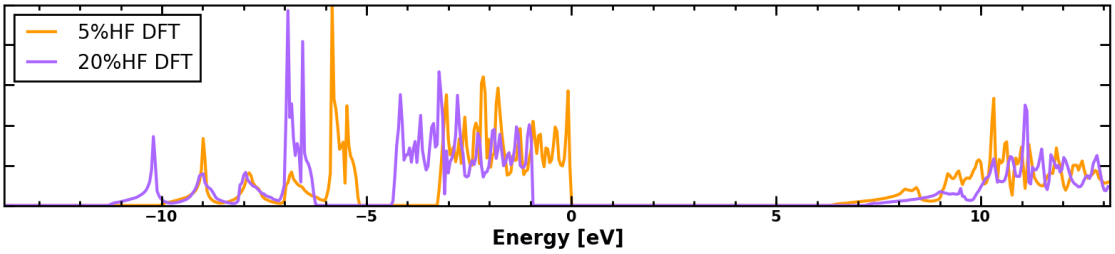

Figure 5.3: Density of states for the α-quartz. Using the B3LYP(20%) functional results in a gap widening of 1.76 eV. The 0 eV level in this figure represents the B3LYP(5%) SiO_2 valence band maximum.

5.2.2 Amorphous SiO_2

A molecular dynamics simulation with the LAMMPS code [22] was run to obtain the coordinates of amorphous SiO_2. An 84 atom cell was created, and the cell dimensions were modified to match the experimental amorphous SiO_2 density of 2.196 g/cm^{-3}. A 100 ps annealing process was run using the Nosé-Hoover thermostat in the NPT ensemble. The resulting structure was then optimised with the PBE functional and the CASTEP code [23]. The cell dimensions were allowed to relax, while the cell angles were kept fixed at $90°$. Upon optimisation the density of the amorphous SiO_2 cell increased to 2.246 g/cm^{-3}. The resulting structure is shown if figure 5.4.

The pair density function was computed for the optimised amorphous SiO_2 cell and it is shown in figure 5.5. The pair distribution function shows a main peak centred around 1.6 Å, which corresponds to the average length of an Si-O bond. A second peak appears at the 2.6 Å and it marks the distance of nearest O-O neighbours in SiO_2 tetrahedra. No other significant peaks are present, indicating a highly amorphous phase — as confirmed by experiment [146].

A single point spin polarised calculation using the B3LYP(5%) functional was run with the CRYSTAL code [24]. The basis introduced by Towler *et al* [142] was used, as in the case of the previously discussed bulk quartz calculations. The total density of states was computed for amorphous SiO_2 was computed. The resulting DOS is shown in figure 5.6. A gap of 6.05 eV is observed, which is smaller than 9.3 eV gap observed in thermally grown SiO_2 films [147].

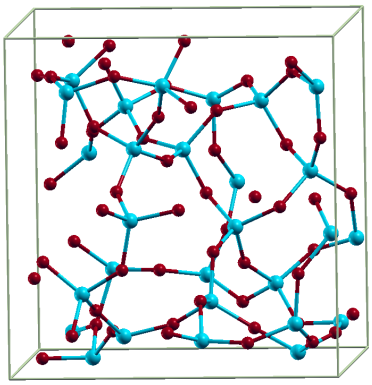

Figure 5.4: Amorphous SiO_2 supercell containing 84 atoms (28 Si atoms and 56 O atoms). The three Cartesian cell dimensions after optimisation are 10.47 Å 10.89 Å 10.88 Å.

Based on these results we conclude that a molecular dynamics COMB run followed by a PBE-level relaxation results in a good structural description. The B3LYP(5%) band gap under-estimates the band gap of amorphous SiO_2.

5.3 Bulk Hafnia

Both crystalline and amorphous monoclinic structures were considered for calculations. In hafnia-based systems the B3LYP(20%) functional was used for electronic structure calculations. Crystalline hafnia is monoclinic at low temperatures, and it transforms into a cubic structure at temperatures higher than 1720° and cubic at temperatures higher than 2600° [148].

5.3.1 Monoclinic Hafnia

In trying to determine the basis set to be used for Si/HfO_2 calculations single point B3LYP(20%) calculation was run on a monoclinic HfO_2 cell comparing the basis sets proposed by Muñoz Ramo

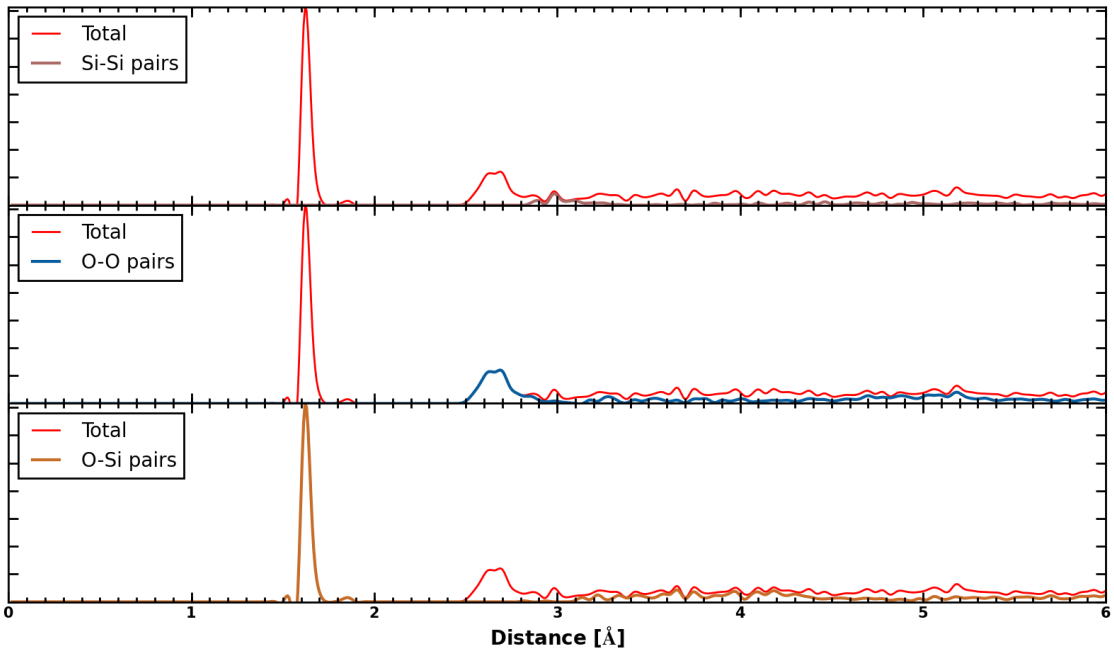

Figure 5.5: Pair density distribution function for PBE optimised amorphous SiO_2. A breakdown of the contributions of Si-O, Si-Si and O-O pair contributions is shown. The main peak appears at 1.6 Å and it represents the average length of an Si-O bond. The second identifiable peak appears around 2.6 Å and represents the 1st O-O coordination shell.

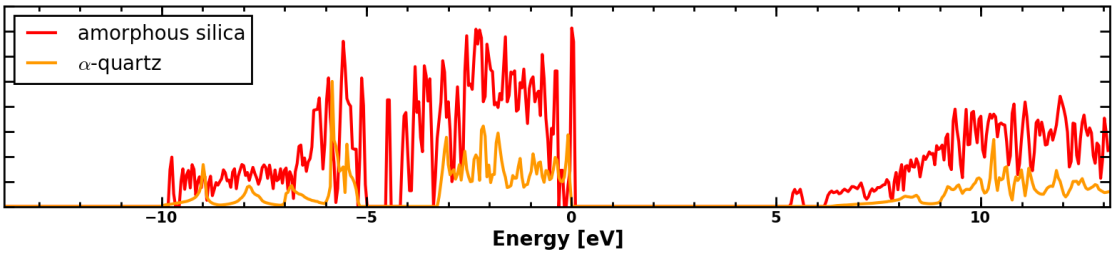

Figure 5.6: Density of states for the amorphous SiO_2 calculated with the B3LYP(5%) functional. The density of states for α-quartz is presented for reference. The 0 eV level represents the B3LYP(5%) level bulk α-quartz valence band maximum.

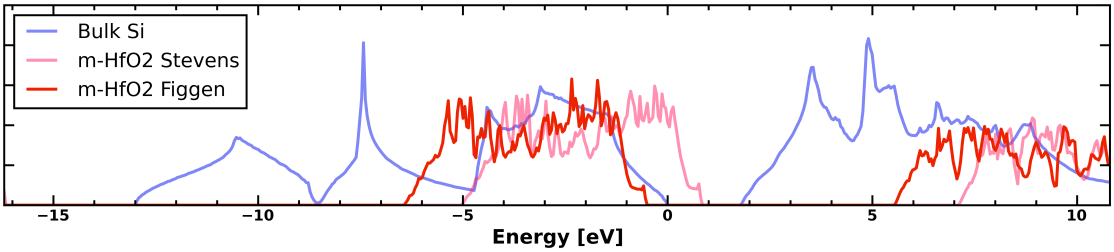

Figure 5.7: B3LYP(20%) density of states for the monoclinic hafnia. The B3LYP(20%) Si density of states is shown for reference. The basis set proposed by Muñoz Ramo *et al* [119] produces a valence band edge maximum for *m*-HfO_2 that is more than 1 eV above that of the bulk Si conduction band. The B3LYP(20%) bulk Si valence band maximum is set to 0 eV.

et al [119] and Figgen *et al* [149]. The experimental lattice parameters given in table 5.2 were used. The density of states obtained with the two basis sets was compared. The result is shown in figure 5.7. An offset between the two basis sets exists, due to the arbitrary global shift at 0 K, the calculation with the Muñoz Ramo basis set yieling a higher valence band maximum for m-HfO_2. The actual shapes of the two DOS curves for the Figgen and Muñoz Ramo basis set calculations are virtually identical. It is clearly known that the HfO_2 valence band maximum lies below that of Si [113, 114, 108, 150]. The gap obtained for the Muñoz Ramo basis set is 6.24 eV while the one obtained with the Figgen basis set is 6.03 eV (this value increases to 6.13 eV after the geometry is optimised). Given the experimental band gap from table 5.3 we chose the Figgen basis set to perform all the calculations presented in the next sections as the 6.13 eV gap it yields fits better within the experimental limits. Ultimately, we would expect the Muñoz Ramo basis set to perform just as well as the Figgen one in calculations.

The CRYSTAL code was used to optimise the *m*-HfO_2 structure with the basis set introduced by Figgen *et al* with a Hay-Wadt small core pseudopotential [151] was used to optimise the structure using the CRYSTAL code [24]. A $6 \times 6 \times 6$ Monkhorst-Pack grid was used. An indirect band gap of 6.13 eV was obtained. Table 5.3 shows how this result compares to other values published in previous studies. The result is in agreement with both the experimentally obtained value of 5.9 ± 0.5 eV reported by Cheynet *et al* [135] and results obtained with the HSE functional (5.98 eV [134]) and the GW approximation (5.9 eV [133]). The predicted lattice parameters are given in

	Functional	a [Å]	b [Å]	c [Å]	β
Present work	B3LYP(20%)	5.170	5.196	5.339	99.47°
Error		1.03%	0.40%	0.90%	0.25%
Zhao [133]	LDA	5.171	5.276	5.292	99.35°
Error		1.05%	1.95%	0.01%	0.13%
Komsa [134]	PBE	5.09	5.12	5.34	99.61°
Error		0.52%	1.06%	0.92%	0.39%
Ceresoli [152]	LDA	5.106	5.165	5.281	N/A
Error		0.21%	0.19%	0.18%	N/A
Lyons [153]	HSE	5.12	5.16	5.28	N/A
Error		0.05%	0.28%	0.20%	N/A
Wu [121]	GGA	5.20	5.31	5.45	99.22°
Error		1.62%	2.6%	3.00%	0.00%
Exp [154]	N/A	5.117	5.175	5.291	99.22°

Table 5.2: Obtained lattice parameters for *m*-HfO_2 optimised at the B3LYP level with the basis set proposed by Figgen *et al* [149]. Our B3LYP results are in agreement with previously published theoretical and experimental values.

table 5.2 and match previously published experimental and theoretical values which are shown in table 5.2.

The CRYSTAL14 code was used to calculate the Raman spectrum of the optimised m-HfO_2 cell. The result is shown in figure 5.8. The calculation of Raman intensities in the CRYSTAL code has been implemented by Maschio *et al* [155]. The Raman-Stokes scattering intensity for the i-th vibrational mode of frequency ω_i is defined by the polarisability tensor α_{xy} and the normal mode coordinate for mode Q_i

$$I^i_{xy} \approx C \left(\frac{\alpha_{xy}}{Q_i} \right)^2 \tag{5.1}$$

	Functional	E_g band-gap
Present work	B3LYP(20%)	6.13 eV
Zhao [133]	LDA	3.9 eV
Zhao [133]	GW_0	5.9 eV
Komsa [134]	PBE	4.34 eV
Komsa [134]	HSE06	5.98 eV
Komsa [134]	PBE0	6.75 eV
Exp [135]	N/A	5.9 ± 0.5 eV

Table 5.3: Comparison of band gap for *m*-HfO_2 with literature values. Our B3LYP(20%) calculation matches the HSE and GW published results, as well as the experimental gap obtained by Cheynet and co-workers.

where the C prefactor depends on the laser frequency ω_L and the temperature T

$$C \sim (\omega_L - \omega_i)^4 \frac{\left[1 - \exp(-\frac{\hbar\omega_i}{K_B T})\right]^- 1}{30\omega_i} \tag{5.2}$$

where K_B is the Boltzmann constant and $\hbar$ is the reduced Planck constant. The intensity of the transverse optical (TO) modes is obtained after the polarisability derivative is computed. A correction is needed for computing the intensity of the longitudinal optical (LO) modes detailed in reference [156].

The calculated spectrum matches the experimental measurement of Modreanu *et al* [109]. A Raman calculation presented by Wu *et al* using the LDA functional with the Hartwigsen–Goedecker–Hutter (HGH) scheme for the exchange-correlation energy is shown for reference. Our B3LYP(20%) calculation offers a better prediction to the experimental results than the LDA-HGH calculation of Wu *et al* for the peak splitting the 520 cm^{-1} to 600 cm^{-1} region and the 300 cm^{-1} to 350 cm^{-1} region.

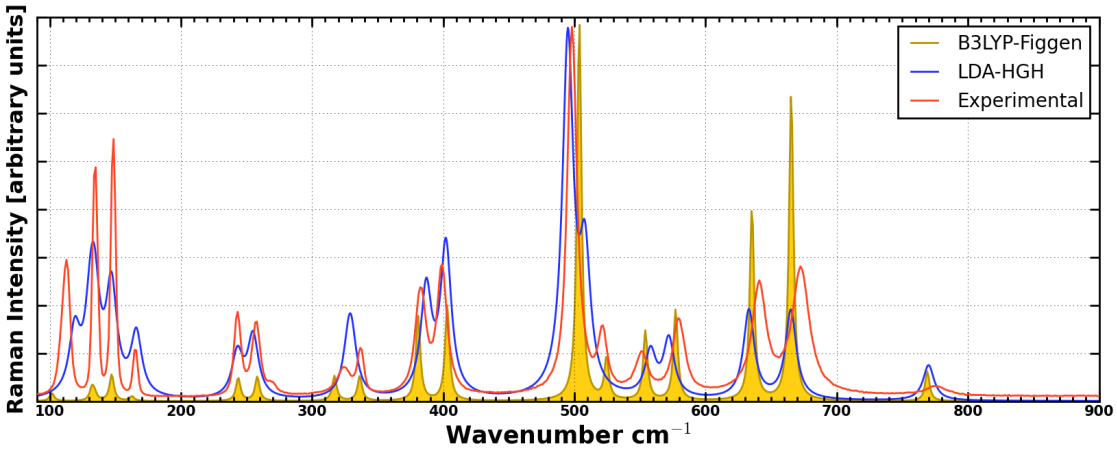

Figure 5.8: Raman spectrum calculated with the Figgen basis set. The experimental spectrum as measured by Modreanu *et al* [109] and the LDA calculation was done by Wu *et al* [121].

5.3.2 Amorphous Hafnia

Amorphous HfO_2 is used in Si-based devices due to lattice mismatch between monoclinic hafnia and bulk Si. A $2 \times 2 \times 2$ expansion of the monoclinic conventional cell resulted in a slab cell containing 96 atoms. The resulting orthorhombic cell's x, y and z dimensions were 10.3 Å 10.3 Å and 10.4 Å respectively. The density of the cell is 10.04 g/cm^{-3}. The COMB potential [38] was used on the HfO_2 supercell in a melting simulation. A temperature of 7000 K was used for 100 picoseconds. A high-temperature snapshot was chosen since the material showed a strong tendency to crystallise when cooled.

The amorphous structure extracted from the T $=$ 7000K snapshot was then optimised using the PBE functional as implemented in the CASTEP [23] code. The cell dimensions were allowed to relax while the cell angles were kept fixed at $90°$. Upon optimisation this density shifted to 10.84 g/cm^{-3}. The resulting structure can be observed in figure 5.9.

The pair distribution function for the optimised amorphous HfO_2 structure is shown in figure 5.10. The location and width of the Hf-O, Hf-Hf and O-O peaks is in agreement with the previously published *ab intio* molecular dynamics results of Scopel *et al* [123] and Chen and Kuo [124] and

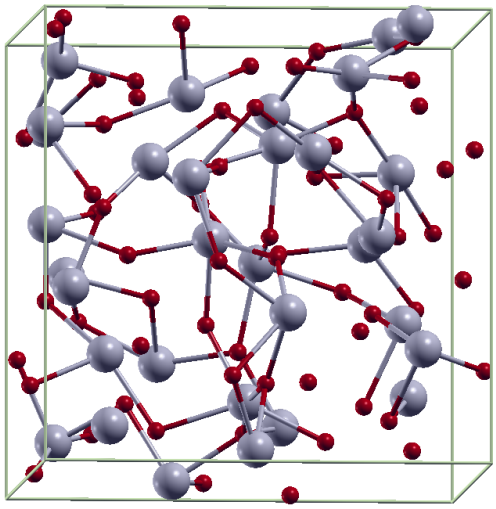

Figure 5.9: Unit cell for amorphous HfO_2 containing 96 atoms used for the determination of the structural and electronic parameters of bulk amorphous hafnia. The density of the structure after the PBE geometry optimisation is 10.84 g/cm^{-3}, higher than the one considered for MD simulations by Wang *et al* [157] but in the range of MD simulations ran by Broglia *et al* [125].

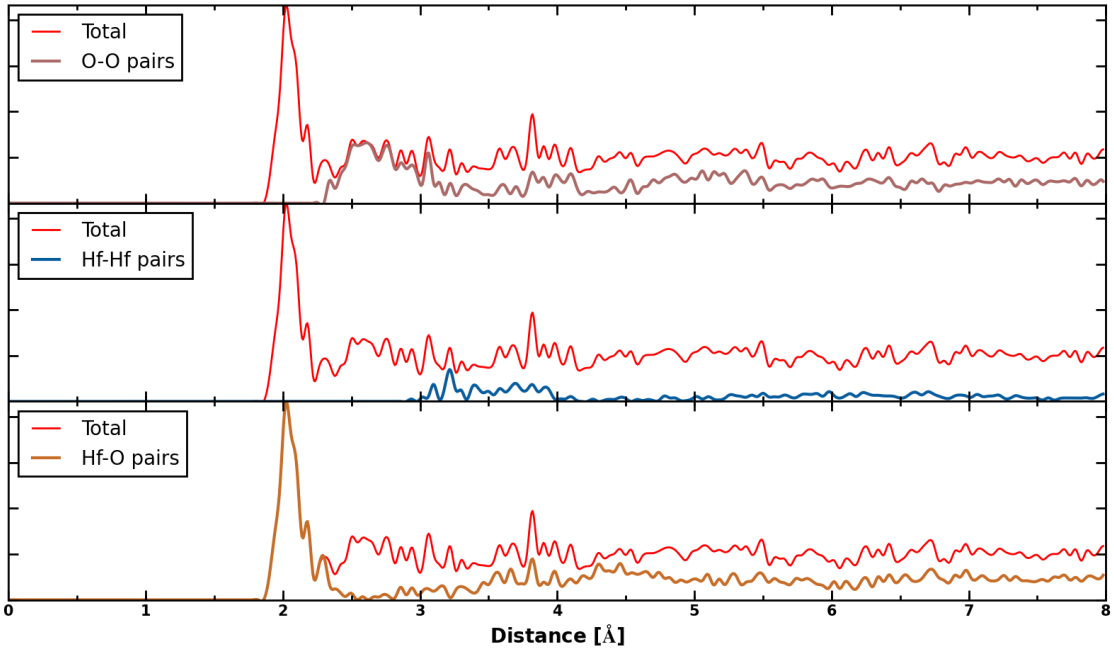

Figure 5.10: Pair density distribution function for PBE optimised amorphous HfO_2. The first peak in the range $2 - 2.4$ Å marks Hf-O pairs. One Hf-Hf pair creates a small peak < 3 Å.

in agreement classical molecular dynamics calculations performed by Wang *et al* [157] and Kaneta and Yamasaki [122].

Perevalov *et al* [158] experimentally determined the Hf-O peak to lie slightly below the 2 Å and the Hf-Hf peak to be near 3 Å. The density is higher than the 7.97 g/cm^{-3} observed by Wang et al to produce compact, reasonably amorphous structures and the 8.6 g/cm^{-3} density reported by Kaneta and Yamasaki.

A single point B3LYP(20%) calculation was run on the PBE structure. The obstained density of states is shown in figure 5.11. A 5.47 eV band gap is observed. This is in agrement with the experimental 5.6 eV gap value measured by Afanas'ev *et al* [104] and the 5.7 eV gap value measured by Takeuchi *et al* [159]. This obtained value is smaller than the PBE0 level 5.94 eV gap obtained by Chen and Kuo [124].

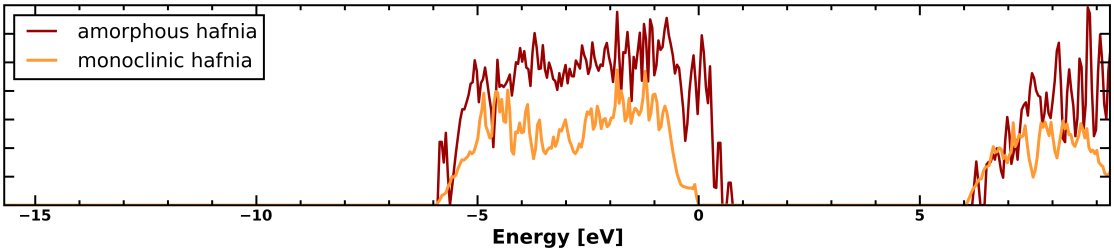

Figure 5.11: Density of states for the amorphous HfO_2 calculated with the B3LYP(20%) functional. The m-HfO_2 density of states is shown for reference. The 0 eV level is set to the B3LYP(20%) m-HfO_2 valence band maximum.

In summary, B3LYP(5%) provides a good estimate of the Si band gap, while under-estimating the SiO_2 band gap. The B3LYP(20%) functional offers a good estimation of both the crystalline and amorphous HfO_2 band gaps. Using the COMB10 potential to melt SiO_2 and HfO_2 structures and subsequently optimise them at the PBE level results in structures results in structures with radial pair distribution functions that match those in the available literature. This leads us to conclude that a sufficiently good procedure of generating Si/SiO_2 and Si/HfO_2 interface structure and density of states is (1) a COMB10 melting to generate the position of atoms in the amorphous oxide layer (2) a PBE-level optimisation of the structure and (3) a single point B3LYP(5%) for Si/SiO_2 interface structures and a B3LYP(20%) calculation for the Si/HfO_2 structures. Different functionals were used for Si/SiO_2 interface structures and Si/HfO_2 interface structures as single point self consistent field calculations with the B3LYP(5%) functional on Si/HfO_2 structures proved exceedingly difficult to converge.

Chapter 6

Si/SiO_2 Interface Calculations

Nine model Si/SiO_2 structures were used to test the properties of silicon-silica interfaces. Interfaces between amorphous SiO_2 with unoxidised and pre-oxidised Si interfaces were considered. Molecular dynamics and density functional theory methods were used optimise the geometry of the interface structures. Hybrid DFT methods were used to compute the atom projected density of states for the structures. Characteristic defects were identified, and their contribution to the states in the Si band gap was analysed. Passifying hydrogen atoms were added to undercoordinated atoms and a local geometry optimisation of the defect levels was run. The effect of the clearing of gap states was observed for several types of defects.

6.1 Structure generation

Structures were created by manually adding amorphous SiO_2 on either a pristine Si slab or a previously oxidised Si structure. The oxidised Si slab was used to account for the initial row pattern oxidation of (001)Si surfaces [63, 86]. The unoxidised Si slab was constructed by translating the 8 atom 5.42 Å conventional cubic Si cell. A $2 \times 2 \times 2$ translation was performed and two extra monolayers of Si were added. The resulting Si slab is 8 monolayers thick and contains 64 atoms.

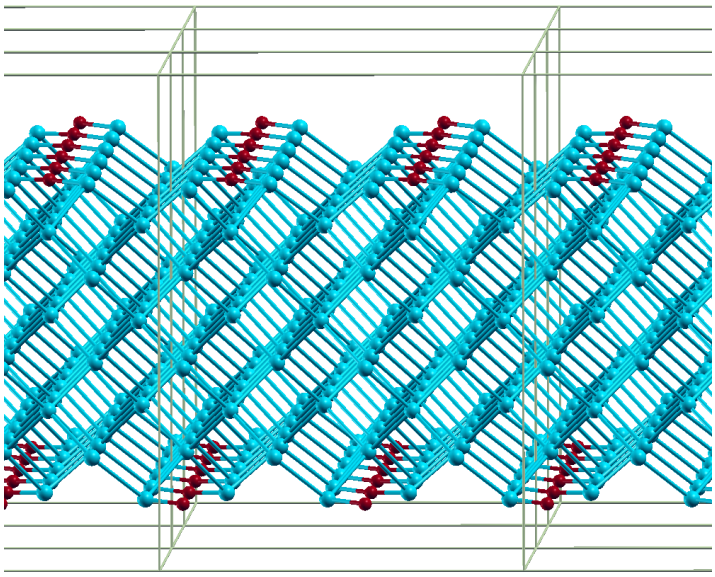

Figure 6.1: Oxidised Si slab used for the generation of O-rich Si/SiO_2 interfaces. The supercell for this slab contains 72 atoms, with 4 Si-O-Si bridges per side. Si atoms are represented in blue and O atoms in red. The structure was optimised at the PBE level. Upon optimisation the horizontal x and y supercell dimensions relaxed at 11.02 Å

The unoxidised (001)Si slab cell x and y dimensions were 10.83 Å. For the oxidised slab, 2 extra monolayers of Si were added. O atoms were inserted in between every pair of neighbouring surface Si atoms. The resulting structure had 72 atoms. Before adding the amorphous oxide layer on top, the slab was optimised using a $4 \times 4 \times 2$ k-mesh with the PBE functional as implemented in the CASTEP code [23]. The structure was considered optimised once the variation in energy per step per ion fell below 2×10^{-4} eV. The manually inserted oxygens prevented the formation of surface Si dimers. After the PBE relaxation the x and y dimensions of the supercell relaxed to 11.02 Å. The resulting structure can be observed in figure 6.1.

The process of generating an Si/SiO_2 interface structure has several steps: (1) Use an MD run on an 84 atoms SiO_2 cell to obtain amorphous coordinates. (2) place the amorphous SiO_2 on

a pristine or oxidised crystalline Si slab, and run a very brief MD pre-relaxation [1]. (3) PBE-level relaxation of the structure. (4) hybrid B3LYP(5%) single-point calculation on the resulting structure. At the end of this process the result is the hybrid-level electronic structure of interfaces between Si and SiO_2. In each of these steps an increasingly higher and more demanding level of theory is used — and each step is done at a level of theory that is currently computationally unfeasible at the step before it repeatedly for structures of relevant sizes. Thus MD techniques are used mainly to generate the atomic coordinates of the amorphous oxide layer, the PBE functional is used to optimise the geometry of the interface structure and the more computationally costly B3LYP(5%) functional is used to obtain the electronic structure of the system.

The coordinates for the atoms in the SiO_2 layer were created via a simulated melting process with molecular dynamics techniques. First an α-quartz conventional cell was translated once in the x and y directions. Two monolayers of SiO_2 (α-quartz) were placed on top. The resulting cubic 10 Å supercell contained 84 atoms, 28 Si atoms and 56 O atoms. Periodic boundary conditions were applied on all cartesian directions. The molecular dynamics melting simulation was done using the COMB10 many-body potential [39] as implemented in the LAMMPS code [22]. A Nosé-Hoover [29] [30] thermostat in the isothermal-isobaric ensemble (NPT) was applied, with an externally imposed temperature varying from 5000 K to 500 K for 10 picoseconds. Six snapshots where chosen from the atomic coordinates produced during their melt, favouring geometries that exhibited a relatively low percentage ($< 40\%$) of undercoordinated atoms, by counting the number of O atoms with fewer than 2 neighbouring atoms and the number of Si with fewer than 4 neighbouring atoms.

All six of these SiO_2 snapshots were manually placed on the unoxidised unreconstructed Si slab previously generated. Three of the snapshots were also manually placed on oxidised Si slabs. The initial horizontal boundaries of the new supercells were chosen to match those of the Si slab. The x and y coordinates of the oxide atoms were scaled to adjust for this constraint. The vertical dimension (perpendicular to the interface) of the cells was adjusted individually, in order to avoid creating unphysically short bonds. Thus the initial vertical cell dimensions ranged from 18.83 Å to 21.55 Å. A total of nine model structures resulted from this process. A very short relaxation

[1] Without this MD pre-relaxation the PBE-level SCF cycle would not always converge, as manually adding the oxide on the Si slab occasionally results in very short (< 1 Å) bonds

using the COMB potential was run in order to relax short bonds formed by manually adding the amorphous silica.

The atomic positions of the structures were subsequently relaxed with the PBE functional [45] as implemented in the plane wave CASTEP code [23]. An open shell calculation was run for each structure. The box size of the first cell was kept fixed for reference, while in the case of the other eight cells the cell dimensions were allowed to relax while the angles between the cell axes were kept fixed at 90°. The geometry relaxation stopping criterion was an energy step $dE/\mathrm{atom} < 5 \times 10^{-4}\ \mathrm{eV}$. The energy stopping criterion was chosen in favour of a minimum force stopping criterion as strains in bonding at the Si/SiO_2 interface impede force minimisations. The nine interface structures finally obtained are shown in figures 6.2 and 6.3. Figure 6.2 shows the six structures obtained using a clean unoxidised Si surface. The remaining three interface structures shown in figure 6.3 present the structures obtained by starting from the oxidised Si slab from figure 6.1.

The PBE-level relaxation was chosen in favour of a pure MD relaxation with the COMB potential because of the observed difference in the number of undercoordinated atoms. By running a PBE relaxation in favour of a COMB one the number of undercoordinated Si and O atoms drops by over 45%. This relative poor performance of the COMB potential in generating defect free oxide layers could be due to the small size of the interface structures considered, as the original paper of Shan *et al* [38] was done on structures several times larger than the ones presented in this work. For this reason in this work the use of the COMB potential was limited strictly to the generation of atomic coordinates for the SiO_2 layer and a very brief pre-relaxation step to eliminate short bonds after the amorphous layer was manually added on the crystalline Si slabs.

For determining the electronic properties of our structures we used the CRYSTAL code [24] to run single point, all electron spin polarised hybrid DFT calculations at the B3LYP(5%) level using gaussian local basis sets (same basis sets used in chapter 5). The calculation was stopped when the energy difference in between cycles dropped below 10^{-6} Hartree. All the results presented on the electronic structure of the models use energy values obtained from these hybrid DFT calculations. The B3LYP(5%) level was chosen for its accuracy in determining the band gap of bulk Si.

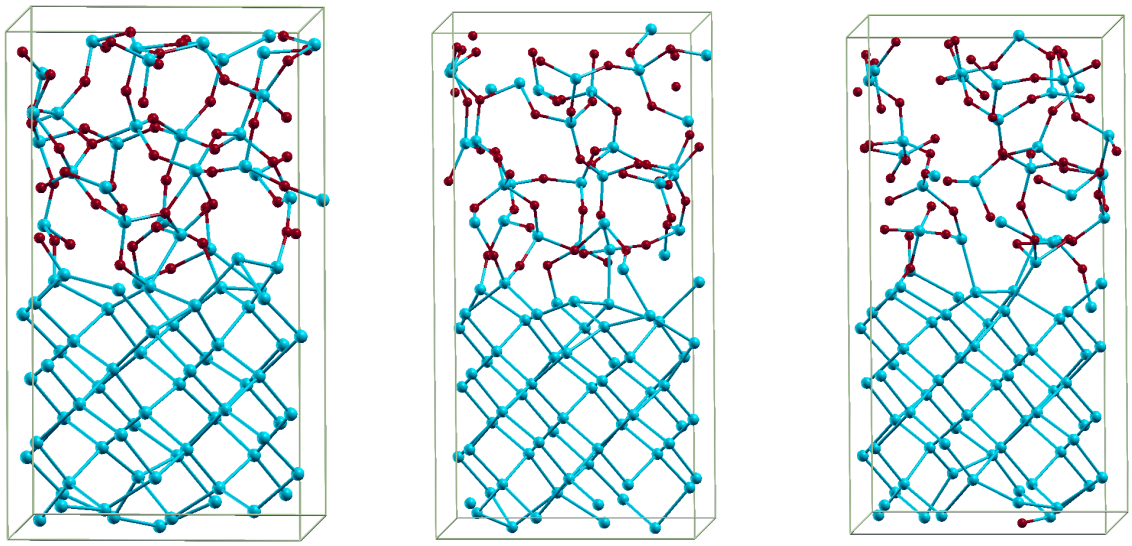

(a) Cell 1 (b) Cell 2 (c) Cell 3

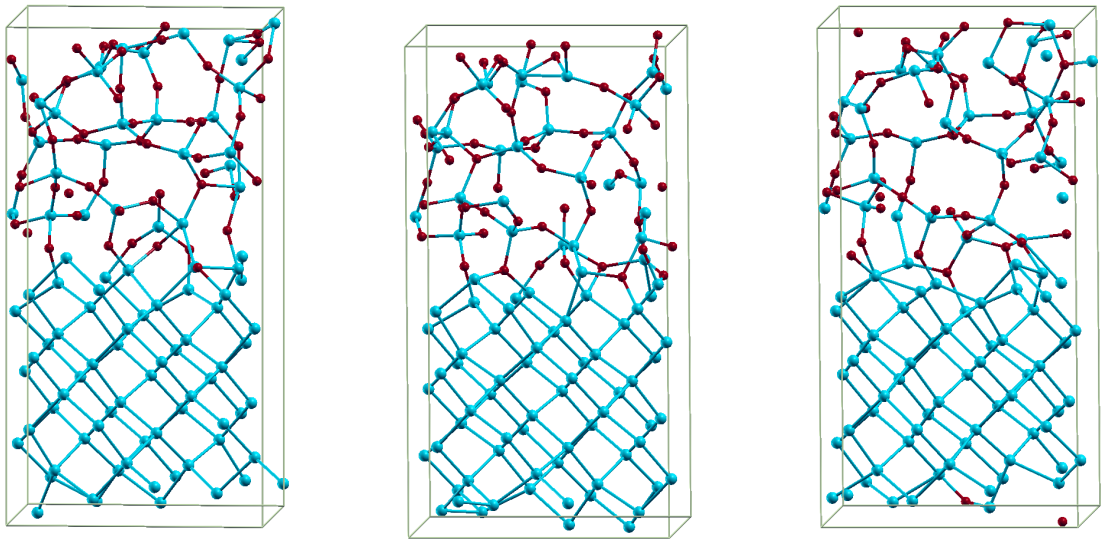

(d) Cell 4 (e) Cell 5 (f) Cell 6

Figure 6.2: PBE-optimised structures for (001)Si/SiO_2 interface structures using an unoxidised Si slab. For the 1st cell the box size was kept fixed (10.83 Å for the x and y dimensions, and 18.86 Å for the vertical z dimension), while for the others the cell dimensions were allowed to relax. During the PBE optimisation, Si-Si dimers form at the Si/SiO_2 interface in all but one cell (i.e. cell 4).

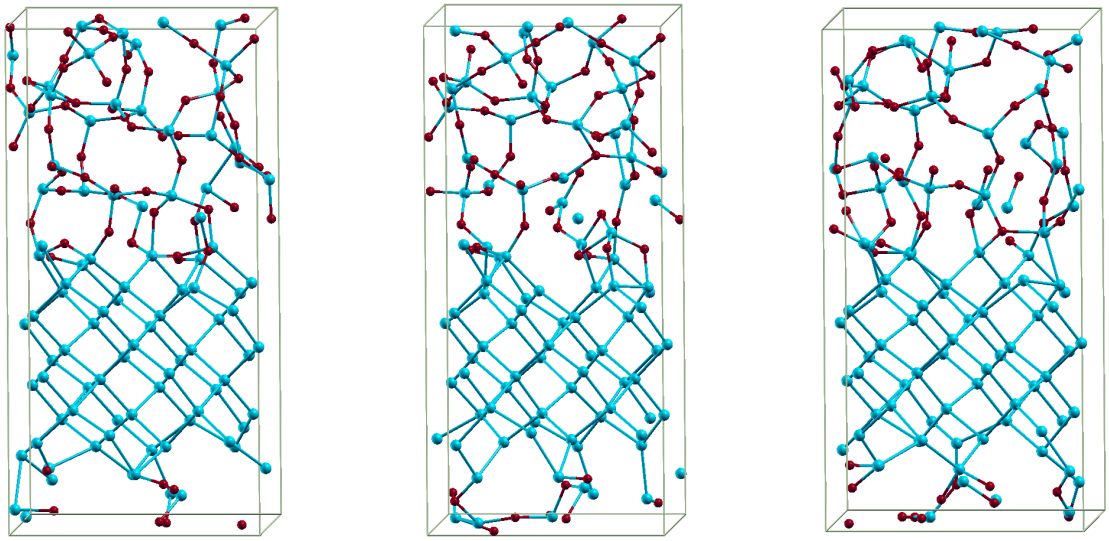

(a) Oxidised Cell 2 (b) Oxidised Cell 3 (c) Oxidised Cell 5

Figure 6.3: PBE-optimised structures for Si/SiO_2 interface structures using an oxidised Si surface. The initial positions of the SiO_2 oxide layer were the same as the initial positions of the SiO_2 atoms from cells 2, 3 and 5 pictured in figures 6.2b, 6.2c and 6.2e respectively. One dimerised Si surface pair appeared in each of the oxidised cells.

The effect of hydrogen passivation on the electronic properties of the unoxidised Si interface structures (figure 6.2) was also analysed. For this structural defects were identified. For each Si atom the distance to the nearest 4 neighbours was computed. If one or more neighbours were found at a distance > 3 Å for Si-Si bonds or > 2 Å for Si-O bonds, one or more hydrogen atoms were added to the defect. This automatic detection of defects resulted in using up to 13 hydrogen atoms per interface structure — which results in a hydrogen density roughly two order of magnitudes higher than that reported in the experimental works discussed in Chapter 3. The upside of choosing to passivate each individual defect results in being able to observe the effect of H passivation on the DOS of the structures for each such defect in part. Such effects on specific types of defects are discussed in section 6.4.

A local PBE-level optimisation was run on the hydrogen passified structures. The supercell dimensions and angles were kept fixed. Atomic positions were kept frozen throughout the run for all atoms not directly bonded to the passivated defects. This local geometry optimisation was stopped once the energy steps between the cycles reached $dE/\mathrm{atom} < 5 \times 10^{-4}$ eV. A single point B3LYP(5%) calculation was run on the resulting structure.

For reference, a crystalline Si/α-quartz interface structure was created. 10 atomic layers were used for the Si substrate and 7 atomic layers of SiO_2 for the oxide. O atoms were manually inserted into the neighbouring surface to prevent Si dimer formation. The quartz layer was arranged in such a way that no undercoordinated atoms appear at any of the two interfaces. The cell dimensions and the atomic positions were relaxed with the PBE functional. The cell angles were kept fixed at 90°. The resulting structure is shown in figure 6.4.

6.2 Structural properties

A total of eighteen 1.16 nm^2 interfaces are found in the 9 structure we generated and optimised with first principles methods. As previously mentioned, initial atomic positions for the oxide layer added to the oxidised cells were also used in unoxidised Si interfaces. However, by examining the structures presented in figures 6.2b, 6.2c and 6.2e with their oxidised counterparts from figure

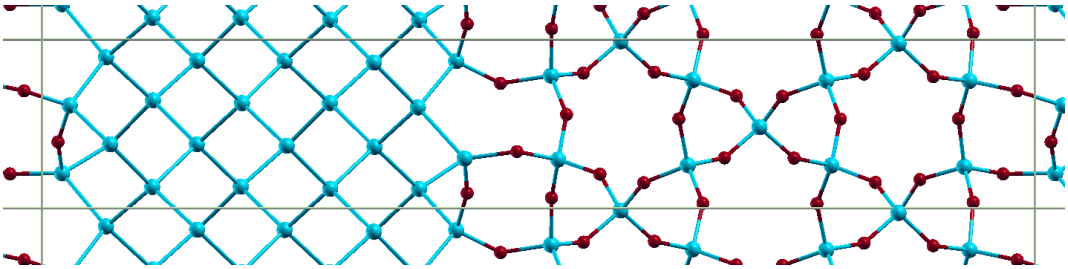

Figure 6.4: Supercell for α-quartz/Si structure. The supercell contains 57 atoms, out of which 27 are O atoms (red) and 30 Si (blue). Oxygen atoms were manually inserted between neighbouring surface Si atom pairs to prevent surface Si-Si dimer formation.

6.3a, 6.3b and 6.3c respectively, it can be seen that the configuration of the atomic positions in the oxide is significantly altered during the optimisation, the bonding pattern at the interface affecting the oxide atoms ~ 5 nm into the SiO_2 layer.

The relaxed x and y supercell dimensions for the unoxidised Si structures vary from 10.18 Å to 11.09 Å. The vertical z dimensions (perpendicular to the interface) vary from 20.87 Å to 21.18 Å. For the 3 structures obtained using the oxidised Si slab presented in figure 6.1 the x and y horizontal dimensions range from 10.48 Å to 11.07 Å. Using 2 extra monolayers of Si for the oxidised Si structures also results in higher vertical z cell dimensions of 21.99 Å for the first oxidised cell (figure 6.3a), 22.52 Å for the second (figure 6.3b) and 21.6 Å for the third oxidised Si cell (figure 6.3c). 2×1 dimer reconstructions of the (001)Si slab appear at the Si/SiO_2 layer in all structures but one structure (cell 4, shown in figure 6.2d).

We calculated the mass density profile for all the interface structures, and the results are shown in figure 6.5 for the unoxidised Si slabs and 6.6 for the oxidised Si structures. The density value $\rho(z)$ was calculated as the atomic mass of the atoms in the structure with a z coordinate in the interval $[z - dz : z + dz]$ divided by the volume $2S \cdot dz$, where S is the cross section of the structure and $dz = 1.15$ Å. A Gaussian smoothing filter was applied to the graph. The average density of the Si slab closely approximates the 2.33g/cm^3 experimental density for bulk silicon. The density of the amorphous oxide layer varies between that of crystalline α-quartz (2.66 g/cm^3) and that of amorphous SiO_2 (2.328 cm/g^3). The small SiO_2 layer thickness (< 12 Å), compounded by the

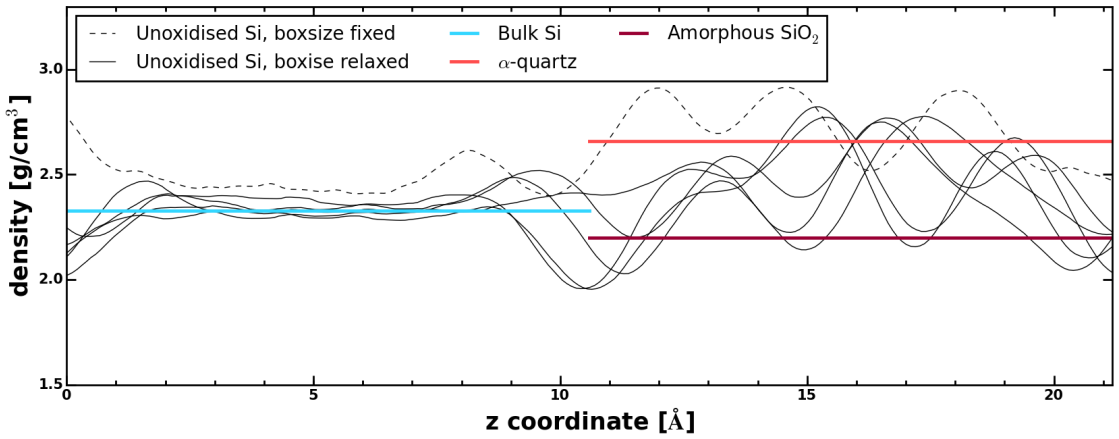

Figure 6.5: Density profile for Si/SiO_2 cells using a clean unoxidised Si slab. The experimental value for the density of Si, α-quartz and amorphous SiO_2 [144] are shown in blue, light and dark red respectively. The density profile of the structure optimised with a fixed box size (cell 1) is marked with a dashed line. For the cells that were allowed to relax (cell 2-6) the density profile is marked with a continuous line.

double interfacing with Si, prevents the appearance of a bulk amorphous phase. In figure 6.5 we can observe that keeping the box size fixed (dashed line) results in a higher density for both the Si and SiO_2 layers. The density of the interface layers tends to be higher for the oxidised structures, as can be seen in figure 6.6. The increased density of the near interface oxide layer has been observed experimentally through X-Ray reflectivity measurements [160] and the low density at the transition monolayer has been observed in other first-principles theoretical studies [46] [161].

The pair density function $g(\mathbf{r})$ was computed for the structures and is presented in figure 6.7. This distribution function gives the density of particles found at a distance r from each other. Crystalline materials produce several clear coordination shells. Amorphous materials present peaks only in the nearest neighbour region.

We observe a more narrow distribution of Si-Si bonds than that of the Si-O pairs. The Si-Si pair distribution function peak for the cell optimised with a fixed box size (dashed line, figure 6.7b) is offset from the rest of the distribution by roughly 0.03 Å. This effect is not strongly visible in the

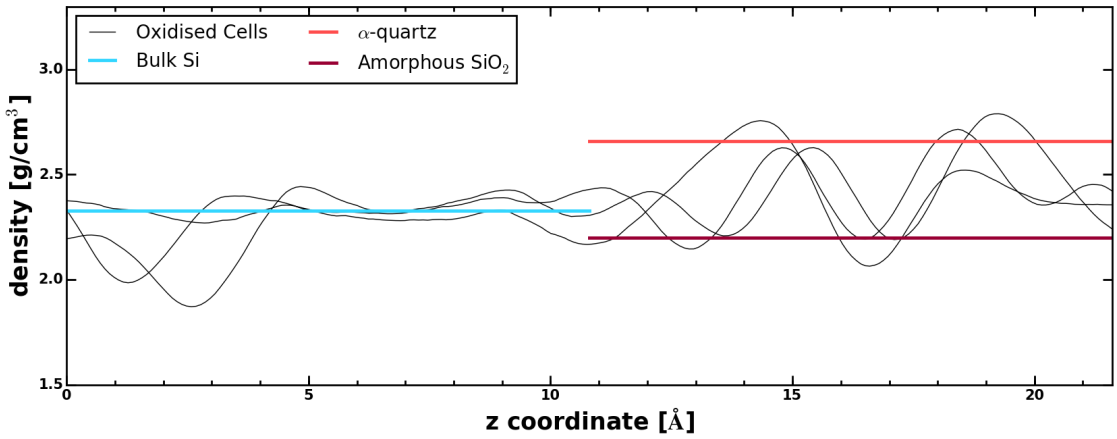

Figure 6.6: Density profile for interface structures created with an initially oxidised surface. The experimental value for the density of Si, α-quartz and amorphous SiO_2 [144] are shown in blue, red and dark red respectively. The 0 point marks the lower interface of the Si slab.

distribution of the more plastic Si-O bonds. The dimerised surface Si-Si atoms do not produce a clear peak as their lengths can vary from 2.35 Å to 2.7 Å. Si-O bonds from inserted O into the neighbouring Si on the oxidised surfaces vary significantly in length from 1.65 Å to 1.8 Å. Stretched Si-Si and Si-O bonds do result in an asymmetry of the corresponding peaks in the pair distribution function.

A brief summary on the experimental data on suboxidation states in Si/SiO_2 interfaces is presented in section 3.1.1. We determined the nearest 4 neighbours for each of the Si atoms in our structures. Si atoms were considered suboxides if only and only if 1, 2 or 3 of those nearest 4 neighbours were oxygen atoms found at a distance of less than 1.9 Å. A gaussian smoothing filter was applied. For the unoxidised Si interfaces we found the ratio of Si^{1+}, Si^{2+} and Si^{3+} oxidation states to be $0.47 : 0.26 : 0.27$. For the oxidised cells this ratio becomes $0.28 : 0.41 : 0.31$. The experimental Si^{1+}:Si^{2+}:Si^{3+} suboxide ratio was determined to be $0.3 : 0.3 : 0.4$ by Hollinger and Himpsel [54]. We present a comparison of the suboxide density profile for unoxidised and oxidised interfaces in figure 6.8. A higher density of Si^{2+} suboxides can be observed at the interface layer of the oxidised cells. The smaller ratio of Si^{3+} suboxides can be attributed to the small thickness of the oxide layer. Such suboxides are the basis of E' defects, which are intrinsic to bulk SiO_2. As seen

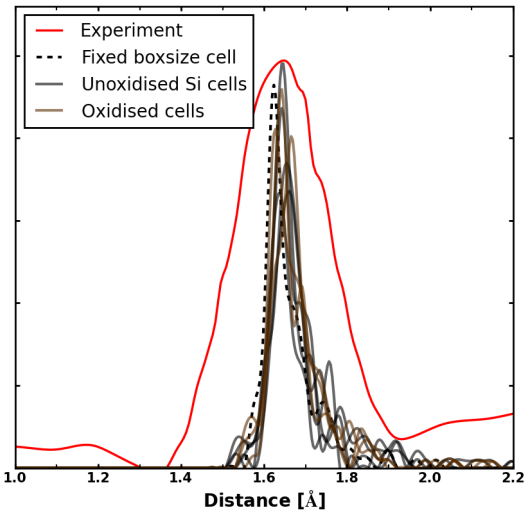

(a) Pair density distribution function for Si-O pairs. The experimental SiO_2 data is taken from Wright [146].

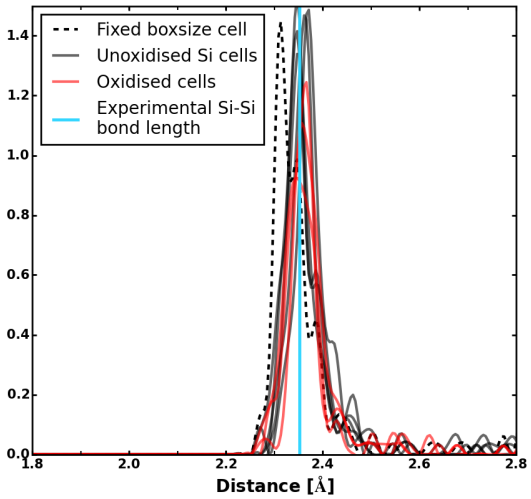

(b) Pair density distribution function for Si-Si pairs. The experimental value is taken from Sutton et al [140].

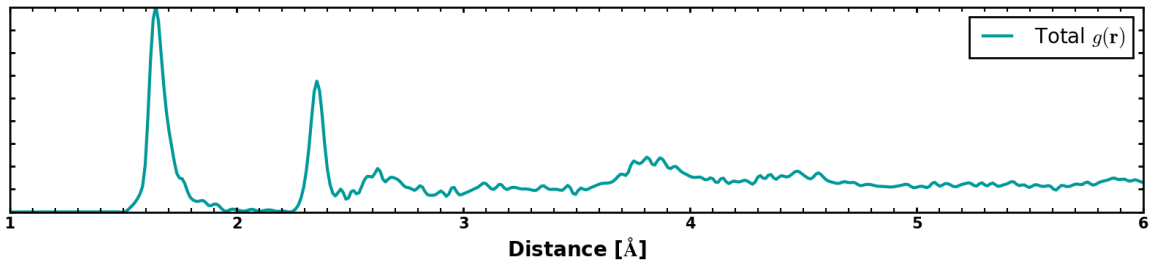

(c) Total pair distribution function for the 9 obtained cells

Figure 6.7: Radial pair density distribution function $g(r)$ for Si-O (a) and Si-Si pairs (b) and total pair distribution function (c) obtained for the 9 structures shown if figures 6.2 and 6.3.

in figure 6.8, Si^{1+} and Si^{2+} suboxides are concentrated in the near-interface layers, while Si^{3+} suboxides are found in between the two interface layers. The distribution of such Si^{3+} suboxides doesn't seem to be significantly affected by the existence of an initial oxidation layer on the Si slabs. We computed the density of suboxide defects per unit surface to be 0.1 Å^{-2}. This was done by considering all suboxides to be part of the near-interface layer and taking into account the fact that each structure has effectively two Si/SiO_2 interfaces. This density is in agreement with Holliger and Himpsel, who measure it at 0.15 ± 0.05 Å^{-2} [54].

An average hydrogen density of 6 atoms/nm^{-3} was used for the hydrogen passivation. The hydrogen density reported in experimental works is 0.1 atoms/nm^{-3}. The high density of obtained defects could be a caused by the COMB10 molecular dynamics potential used or by lattice frustrations in the amorphous oxide due to the small cell dimensions used. The ~ 1 Å thick oxide has a double interface with crystalline Si, which doesn't allow for several monolayers of fully bulk amorphous SiO_2 phase to emerge. Another reason for the high defect density obtained in our structures could be the experimental observation that low oxidation temperatures produce defect rich (001)Si/SiO_2 interfaces [162]. The high number of intrinsic defects that are observed in the structures provides comes with a silver lining — more data for identifying different types of intrinsic Si/SiO_2 defects.

6.3 Electronic properties

The atom projected density of states was obtained for each structure from the hybrid run. The B3LYP(5%) calculated band gap obtained for bulk silicon is 1.1 eV. This result is in agreement with the experimental gap of 1.11 eV for Si [141]. The B3LYP(5%) functional was explicitly chosen to match the experimental gap value. The drawback of this choice is that the computed band-gap for bulk α-quartz is 6.26 eV. This value is significantly smaller than the GW calculated 10 eV value [163], but higher than the 5.6 eV LDA gap [164].

The total density of states computed for the unoxidised Si cells (figure 6.2) is presented in figure 6.9. The B3LYP(5%) bulk Si valence band maximum was chosen as the 0 eV level for all the

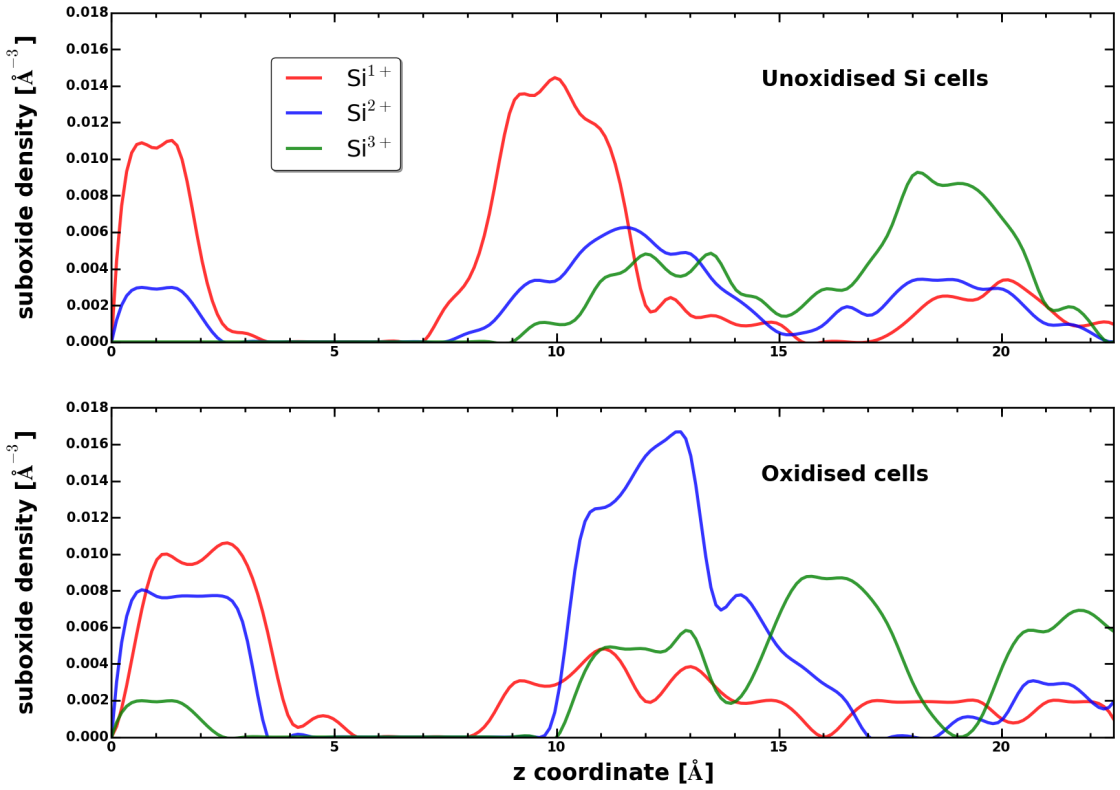

Figure 6.8: Suboxide distribution profile along the z axis for the unoxidised Si cells (see figure 6.2) and the oxidised Si cells (presented in figure 6.3). For the oxidised cells there is a pronounced increase in Si^{2+} suboxide density in favour of the Si^{1+} species. The lower ratio of Si^{3+} suboxides can be attributed to the small thickness of the oxide layer considered. Si^{3+} suboxides form the basis of E' defects which are intrinsic to bulk SiO_2

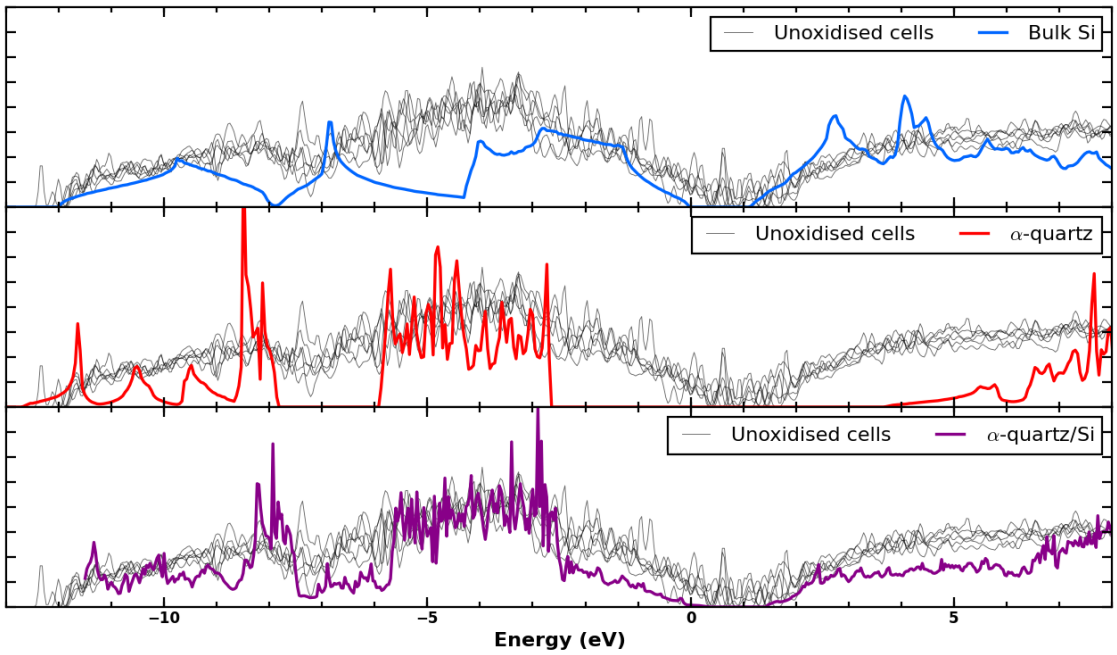

Figure 6.9: The total DOS for unoxidised Si cells (cells shown in figure 6.2). The total density of states calculated for bulk Si, bulk α-quartz and an ideal Si/α-quartz structure (figure 6.4) is shown for reference. The defect-free Si/α-quartz structure has no defects localised in the Si band gap. The density of states for bulk Si (blue), bulk SiO_2 (red) and the α-quartz interface (purple) are shown for reference.

density of states figures in this chapter. The bulk silicon, bulk $\alpha-$quartz and an Si/$\alpha-$quartz structure density of states are presented for reference. It can be observed that the density of states for the Si/SiO_2 structures is effectively formed by characteristic states of bulk Si and bulk α-quartz. A number of localised states appear in the Si band gap. All these states correspond to defect atoms at the interface or within the bulk of the SiO_2 layer. The reference defect-free α-quartz/Si structure (shown in figure 6.4) presents a clear gap, free of localised states. Such localised states are predominantly caused by undercoordinated Si atoms at the interface layers or in the oxide.

The importance of an initial oxidation of the Si surface to minimise the density of interface charge

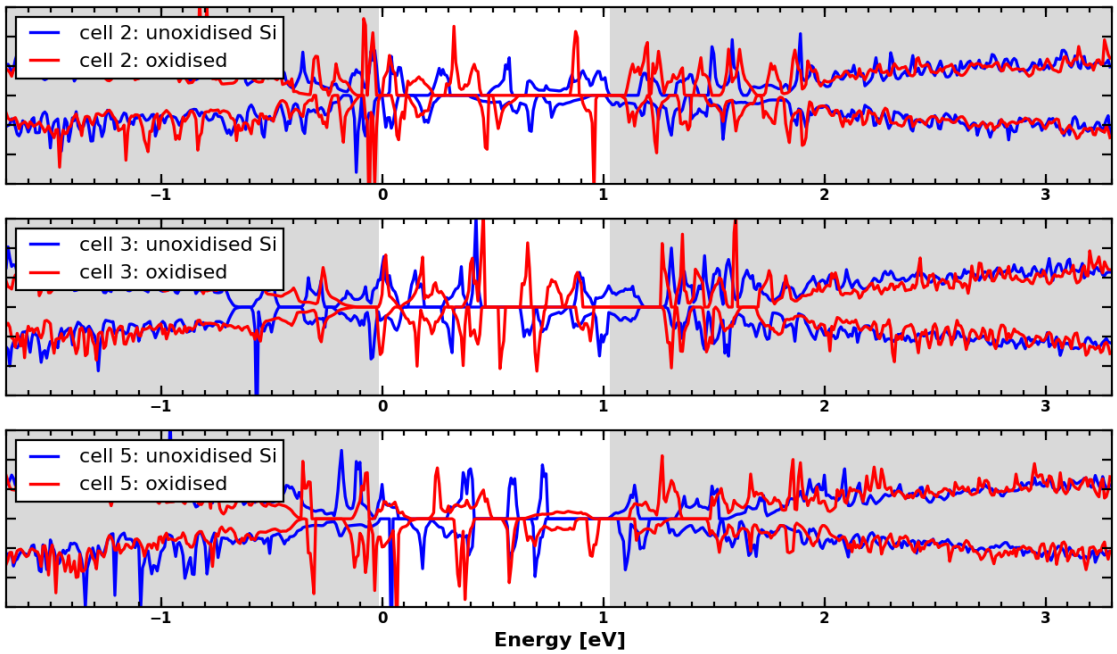

Figure 6.10: Comparison of obtained density of states for the oxidised cells (structures in figures 6.3a, 6.3b and 6.3c) and their unoxidised Si counterparts (structures figures 6.2b, 6.2c and 6.2e). The grey shaded areas represent the Si valence and conduction bands, while the clear white area marks the Si band gap.

traps is well known [165]. In figure 6.10 we present the near gap region DOS for the cells created using an oxidised Si slab (structures shown in figures 6.3a, 6.3b and 6.3c) and their unoxidised Si counterparts (figures 6.2b, 6.2c and 6.2e). Merely adding oxygen atoms in between neighbouring Si atoms at the Si slab surface does not diminish the number of states within the Si band gap.

Hydrogen passivation has a clear effect in eliminating defect states appearing in the Si band gap. The total density of states for these passified structures was computed with the B3LYP(5%) hybrid functional used for the unpassified cells. The results are presented in figure 6.11.

By integrating the densities of states for the unoxidised Si unpassivated cells and the passivated equivalents we can compute the reduction of gap states in the Si band gap. A reduction in the density of Si band gap states is observed for all the cells subjected to hydrogen passivation (i.e. the unoxidised cells presented in figure 6.2), though the reduction integral of the DOS between the Si VBM and CBM levels varies from 2.4% in cell 6 (figure 6.2f) to 52% in the case of cell 3 (figure 6.2c). The effectiveness of hydrogen passivation varies on the type of defect passivated.

Spin polarised solutions are observed in all the Si/SiO_2 structures created with an initially oxidised slab. Out of the structures created with an unoxidised unreconstructed and unoxidised Si slab, structures 1, 4 and 6 (figures 6.2a, 6.2d and 6.2f respectively) do not exhibit spin moments on individual defects. Cells 2, 3 and 5 (figures 6.2b, 6.2c and 6.2e) have spins localised either at the Si/SiO_2 interface layer or in the bulk SiO_2. Such defects are exclusively localised on dangling Si bonds.

6.4 Defect properties

All spin polarised defects are localised on dangling Si bonds. In the nine analysed structures we observed three recurring defects.

1. E' defects — bulk SiO_2 •Si≡O structures
2. Dimer Si dangling bonds — •Si≡Si structures containing a (2×1) Si dimer reconstruction

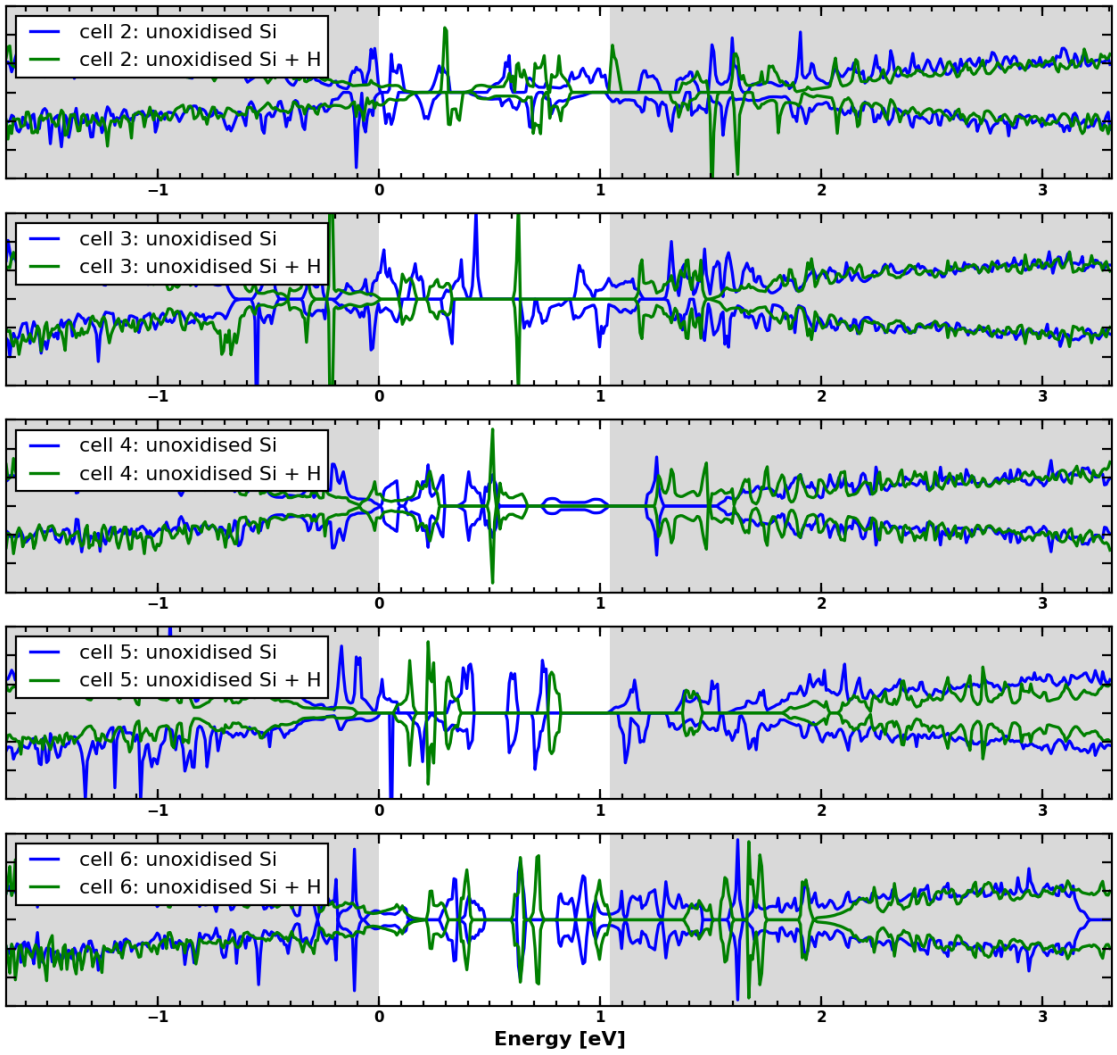

Figure 6.11: Passivation effect on density of states on the structures presented in figure 6.2. A clear improvement in reducing the states in the Si gap (clear area) is observed upon passivation, though certain states remain or become more strongly localised.

	A_0	structure
P_b	11 mT	•Si≡Si in (111)Si/SiO_2
P_{b0}	9.6 mT	•Si≡Si in (001)Si/SiO_2
P_{b1}	12.7 mT	•Si≡Si in (001)Si/SiO_2
E'	43.9 mT	•Si≡O in bulk SiO_2
E'_δ	12. mT	•Si≡O in bulk SiO_2

Table 6.1: Experimental anisotropic hyperfine parameters (reproduced from Lenehan and Conley [13, p. 2051]) for various defects that appear in Si/SiO_2 interfaces or bulk amorphous SiO_2. The P_{b1} experimental A_0 value is taken from Stesmans *et al* [62].

3. Broken dimer structures — O-•Si=Si interface structures, the dangling bond is centered on an Si bonded to both the bond and an oxygen atom from the SiO_2 layer.

The latter two defects, the dimer dangling bond and the broken dimer structure aren't described in the available literature to the best of our knowledge. Stirling *et al* [92] did consider a dimer defect as a possible candidate for the P_{b1} defect structure, but found that the anisotropic hyperfine tensor calculations and the hyperfine axis did not match those of the experimental results [62], and opted for an asymetrically oxidised dimer model instead to describe the structure of P_{b1} defects (see Chapter 3 for details). EPR results by Stathis and Cartier [18] [19] suggest that non-P_{b0} and non-P_{b1} defects are found at Si/SiO_2 interfaces. Other types of unique defects are also present in the nine Si/SiO_2 structures obtained. Exactly one P_{b0} defect was observed. No P_{b1} defect as described by Stirling *et al* in their asymetrically oxidised dimer model was observed. For reference table 6.1 shows the experimentally determined A_0 values for the defects identified with EPR spectroscopy.

The distribution of the hyperfine A_0 parameter value is presented in figure 6.12. Only 3 defects that are not identified as E' have an A_0 hyperfine parameter > 19 mT. Broken dimer and dimer dangling bonds account for the wide majority of defects with low A_0 values. These defects are analysed in the following sections.

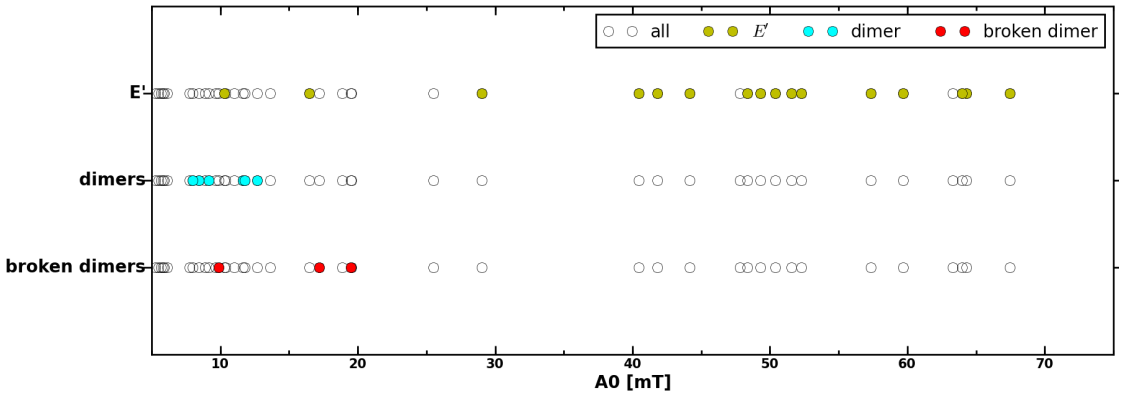

Figure 6.12: Distribution of A_0 values calculated. This diagram shows the relative anisotropic hyperfine values obtained for the three main types of defects. Each blank dot represents an individual defect and its A_0 hyperfine value. To mark the three main types, yellow dots were used for E' defects, blue dots to mark the hyperfine values of dimer defects and red to mark the A_0 values of broken dimer type defects. E' defects account for the overwhelming majority of high A_0 values obtained. The 3 non-E' defects with $A_0 > 1.9$ mT are an oxide O-Si-O bridge and two neighbouring overcoordinated interface Si atoms. Experiments show that E' A_0 values average around 44 mT, P_{b0} defects average at 9.6 mT and P_{b1} defects present A_0 values around 12 mT (cf table 6.1).

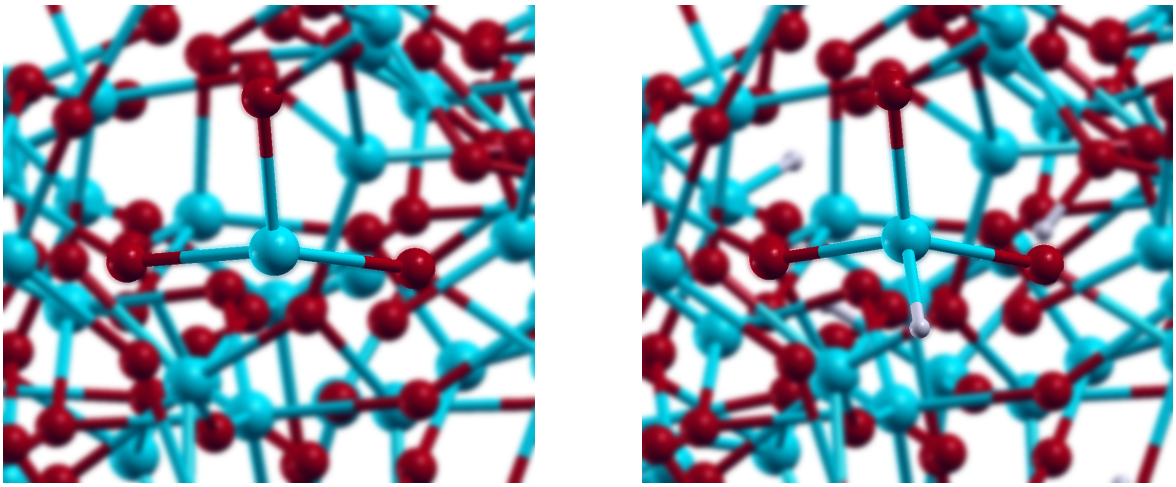

(a) E' defect (b) Hydrogen passified E' defect

Figure 6.13: Unpassified (a) and hydrogen passified (b) E' prime defects.

6.4.1 *E' defects*

E' defects are •Si≡O structures found in bulk silica (see chapter 3). Though initially thought to be caused by oxygen vacancies in the bulk, such defects were shown to be intrinsic to amorphous SiO_2 [166][167]. The structure of an E' defect found in our structures and its hydrogen passified conformation is shown in figure 6.13.

We observed a total of 45 E' defects in the 9 structures considered. While pure silica contains around 10^{17}spins/gram, the high concentration of defects we observe could be attributed to either frustrations induced in the oxide by the proximity of the interface and by the geometry produced by the COMB potential.

The atom projected density for all E' defects is presented in figure 6.14. The number of gap states in the Si band gap is strongly reduced by the presence of hydrogen. These localised states shift towards the inside the Si conduction/valence band region during passivation, effectively clearing the band gap.

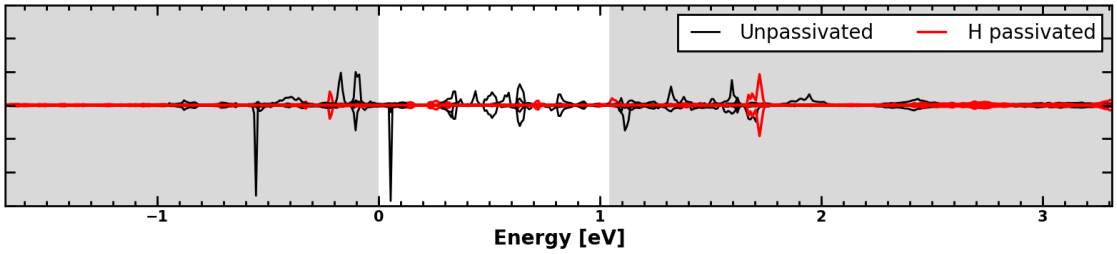

Figure 6.14: Atom projected density of states for all the 45 E' present in the unoxidised Si cells. Black lines represent E' defects from unoxidised unpassivated structures, and red lines represent hydrogen passivated E' defects. Gap localised states shift towards the Si conduction and valence bands (shaded areas).

The relation between the E' calculated isotropic hyperfine A_0 parameters and the structural properties of the E' structure are shown in figure 6.15. Si-O bonds in the E' defect stretched above 1.70 Å are more likely to be paramagnetically active. Isotropic contributions to the hyperfine tensor do not seem to be determined by the average O-Si-O angle. An average angle of $120°$ indicates a flat sp^2-type bonding, while a lower average of the O-Si-O angles marks a buckling of the Si≡O structure.

6.4.2 Dimer defects

During the PBE geometry optimisations 2×1 surface reconstructions of the topmost Si layer appeared for most cells. This type of reconstruction is known to appear on pristine (001) Si surfaces [168]. Like the P_{b0} and P_{b1} defects, dimer defects are non-planar • Si≡Si. The length of the dimer Si-Si bond varies between 2.35 Å to 2.7 Å. In some structures both atoms of the dimer are bonded to an atom from the oxide layer — showing that not all dimerised surface Si result in interface defects. No dimer was identified where both of its Si atoms have a dangling bond. The typical structure of an interface dimer defect and its hydrogen passified equivalent are shown in figure 6.16.

All but one structure (cell 4, shown in figure 6.2d) had dimer defects. Unoxidised Si structures

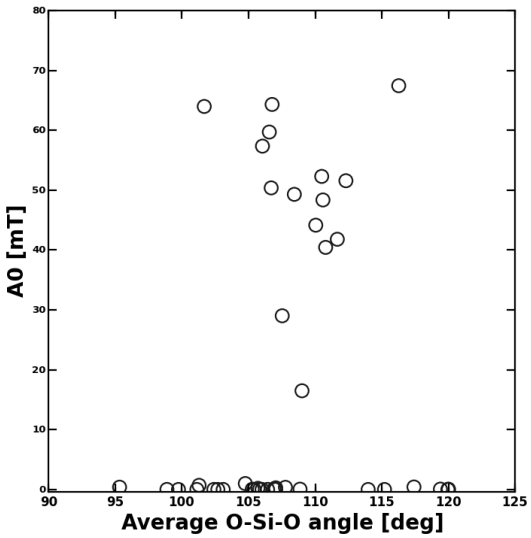

(a) E' defect A_0 value as a function of average Si-O-Si angle

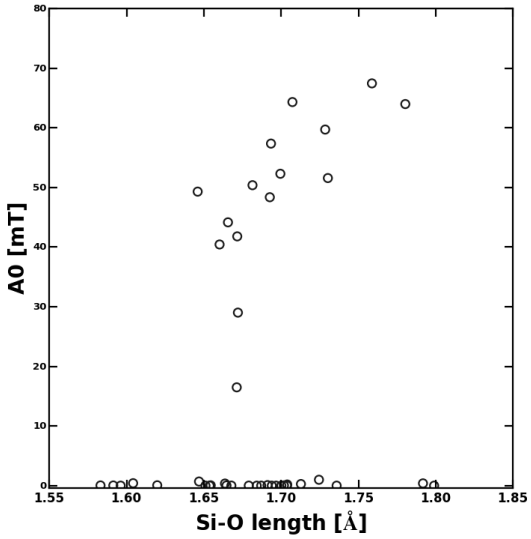

(b) E' defect A_0 value as a function of average Si-O bond length angle

Figure 6.15: Dependence of E' anisotropic A_0 values on structural parameters.These scatter plots aim to show whether a range or a linear dependency between the structural properties (average bond length or average angle) between the Si with the dangling bond and the backbonded atoms that together constitute the defect. In the case of E' defects we observe that an average an increased bond length with the backbonded atoms is indicative of a higher A_0 value. The average O-Si-O angle — a smaller angle indicating a higher degree of buckling of the defect — does not seem to produce higher anisotropic hyperfine values.

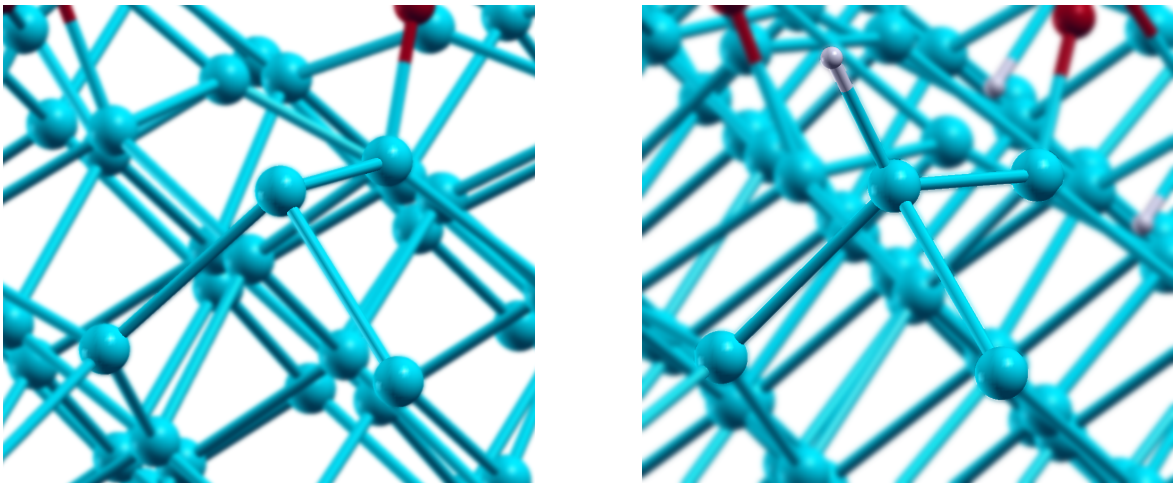

(a) dimer dangling bond

(b) Hydrogen passified dimer dangling bond

Figure 6.16: Dimer defect configuration. Such defects appear on all but one of our structures. (2×1) type reconstructions at the top Si monolayer occur frequently during the PBE-level relaxation. Unlike P_{b0} defects, the dangling bond of such defects does not point in the crystalline $\langle 111\rangle$ direction.

(figure 6.2) had on average 1.33 dimers per structures. Oxidised Si cells presented on average only one such dimer per cell.

A comparison for the passified and non-passified distribution of states in the bulk Si gap caused by dimer defects is shown in figure 6.17. Hydrogen passivation is significantly effective in reducing the number of gap states for SiO_2 interfaces.

The hyperfine axis of dimer defects does not coincide with the $\langle 111\rangle$ hyperfine axis of P_{b0} nor the $\langle 211\rangle$ axis of P_{b1} defects. While not primarily a focus in EPR studies, the formation of Si-Si dimers at the Si/SiO_2 interface has been considered by Stirling et al [92] as a possible candidate for P_{b1} defects, but rejected in favour of an asymetrically oxidised dimer model. Dimer defects were also reported in a theoretical study on GaAs interfaces [169].

Si-Si dimers did not appear in molecular dynamics relaxations using the COMB potential as

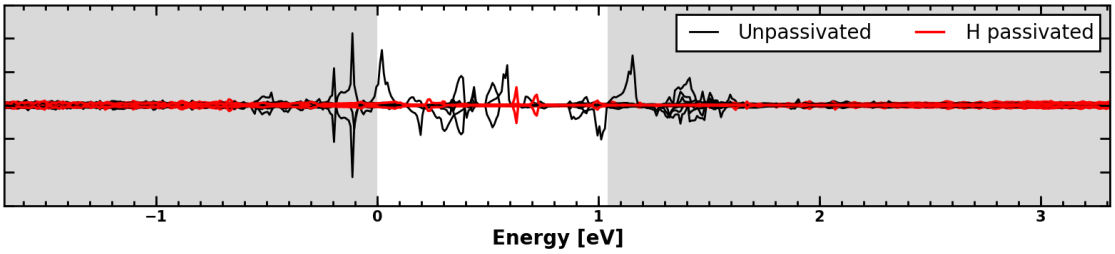

Figure 6.17: Distribution of states in the Si band gap for dimer defects. Atom projected DOS plots are shown for the identified dimers from the unoxidised Si cells (black line), and their passified equivalents are identified (red line). Shaded areas represent the Si valence band and conduction band, respectively.

implemented in the LAMMPS code, and thus cannot be caused by limitations of the potential used. The fact that the (2×1) reconstruction of unoxidised (001)Si surfaces is well known and confirmed experimentally, leads us to conclude that such structures will appear in real SiO_2 structures. A lower dimer density than the one obtained in this work is expected to appear in practice, as an initial oxidation is likely to result in O atoms inserted into the dimer bond rather than the Si backbonds [89].

Figure 6.18 shows the dependence of the A_0 anisotropic contribution to the hyperfine tensor on the structural parameters of the dimer structure. There is no clear dependence of the anisotropic term with respect to the average length between the Si dangling bond and the bonded Si atoms. Defects with a low ($< 98°$) or high ($120°$ an sp^2 hybridisation) (bonded Si)-(dangling Si)-(bonded Si) angles have low Fermi contact terms. Buckled defects with an average Si-Si-Si angle between the range $[98° : 115°]$ tend to show calculated A_0 values higher than 7 mT.

6.4.3 Broken dimer structures

A "broken dimer" defect is a dangling bond on a threefold coordinated surface Si atom that bonds to an O atom from the oxide layer rather than forming a dimer with another surface Si. Fourteen broken dimer (O-•Si=Si) defect structures were observed in the structures analysed. The

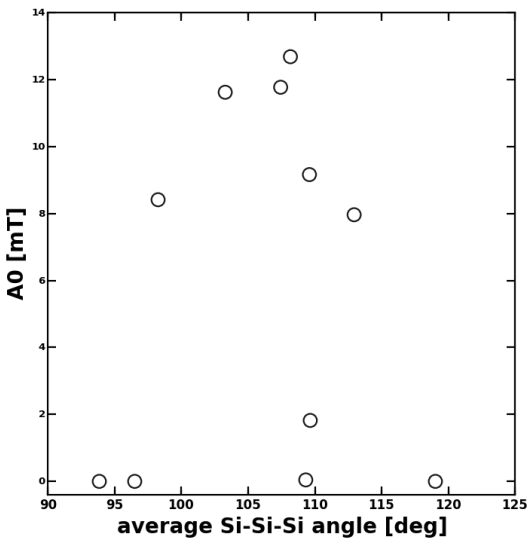

(a) Dimer defect A_0 value as a function of average Si-Si-Si angle

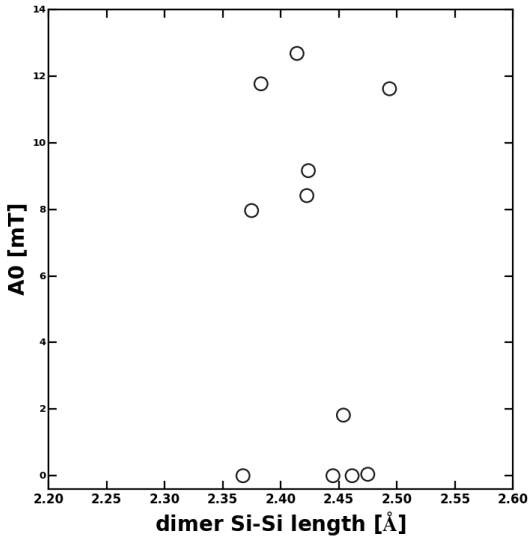

(b) Dimer defect A_0 value as a function of average Si-Si bond length

Figure 6.18: Dependence of dimer dangling bonds A_0 values on structural parameters.These scatter plots aim to show whether a range or a linear dependency between the structural properties of the defect (Si-Si dimer bond length or average angle with the backbonded atoms) and the anisotropic hyperfine A_0 value. In the case of dimer defects no such correlation is observed — neither the average angle with the backbonded Si nor the length of the dimer bond are indicative of a higher or lower A_0 value.

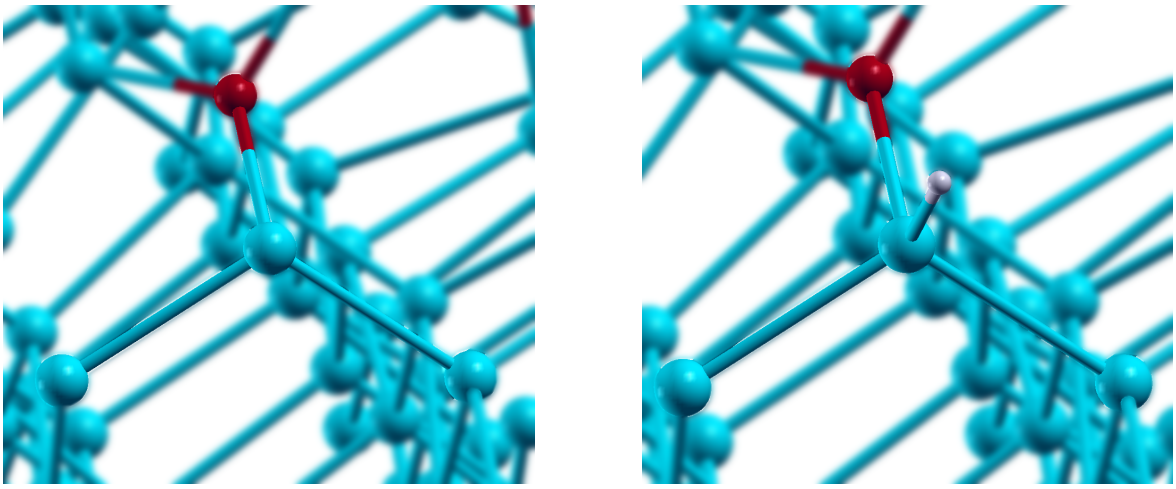

(a) Broken dimer dangling bond

(b) Hydrogen passified broken dimer defect

Figure 6.19: Broken dimer defect configuration. Such defects are present in all the nine structures analysed.

defect Si is bonded to two substrate Si atoms and one oxide O atom, instead of being bonded to a neighbouring surface Si as it is the case of dimer defects. An example of unpassivated and passivated broken dimer structures is shown in figure 6.19. Poindexter *et al* [170] also mentioned such threefold coordinated Si with one O neighbour could be the structure of the P_{b1} defect. All of the structures presented at least one such defect. A total of 14 broken dimer defects were observed in our structures. The O atom of the broken dimer structure doesn't have a restricted position such as the Si atoms in dimer defects. This results in a larger variety in the conformation of broken dimer defects. The Si-O bond can vary in length from 1.6 Å to 1.9 Å.

The distribution of gap states for broken dimer type defects is shown in figure 6.20. Broken dimer defects are not as responsive to hydrogen passivation as dimer defects and E' defects, yet an overall reduction in the DOS is still observed.

Figure 6.21 shows the dependence of the anisotropic A_0 hyperfine parameters as a function of structural parameters. No particular relation exists between the bond lengths of the broken dimer structure and A_0 values. In terms of angles of the broken dimer structure, seemingly high A_0

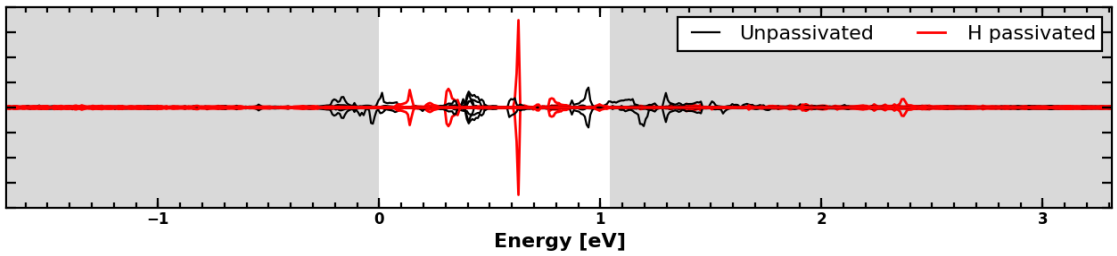

Figure 6.20: Distribution of states in the Si band gap for broken dimer defects. Atom projected DOS plots are shown for the broken dimer defects from the unoxidised Si cells (black line), and their passified equivalents are identified (red line). Shaded areas represent the Si valence band and conduction band, respectively.

values only appear for defects with an average angle in the range $[110^\circ : 113^\circ]$.

6.4.4 Other defects

Several non recurrent or unique defects were identified in our structures. Most of these are Si dangling bonds found in the top two Si slab monolayers or undercoordinated Si from the bulk SiO_2.

Pb_0 defect

A single P_{b0} defect was identified in our structures (cell 2, figure 6.2b). This sp^3 hybridised Si is found in the second monolayer from the interface. The model generally presented in literature shows a P_{b0} defect in an sp^3 hybridised state on the top Si monolayer in Si/SiO_2 interfaces. We argue that such a conformation is less likely, as atoms from the top monolayer have a strong tendency to dimerise. The defect has a localised spin moment and the calculated hyperfine A_0 value for this defect is 5.6 mT. The atom projected density of states for this defect is presented in figure 6.23. Two spin split states are present near the Si valence and conduction bands. Applying a passifying hydrogen effectively removes these two gap states. The fact that we only observed one

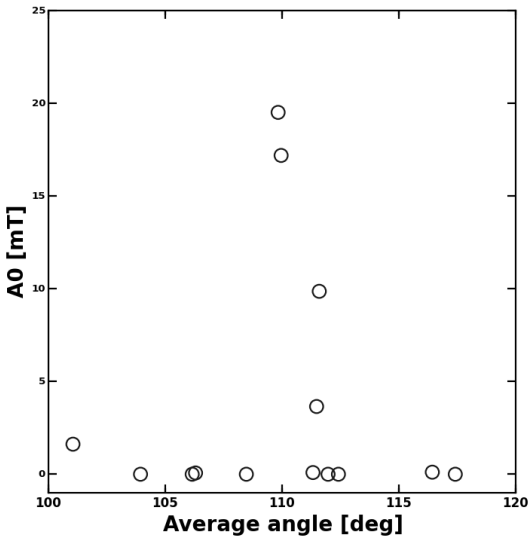

(a) Broken dimer defect A_0 value as a function of average Si-Si-O/Si-Si-Si angle

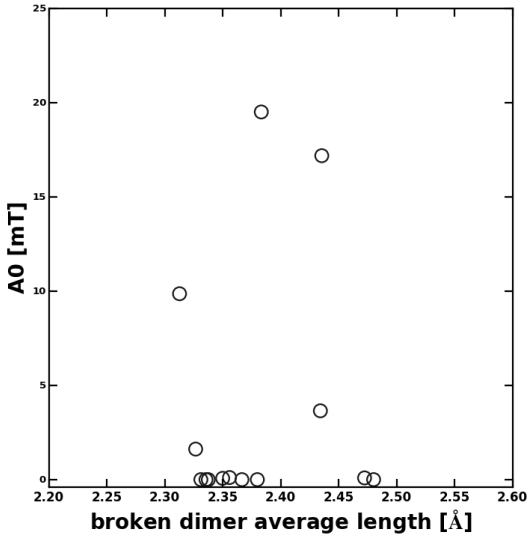

(b) Broken dimer defect A_0 value as a function of average of the Si-O and Si-Si bond lengths

Figure 6.21: Dependence of broken dimer dangling bonds anisotropic hyperfine A_0 values on structural parameters. These scatter plots aim to show whether a range or a linear dependency between the structural properties (average bond length or average angle) between the Si with the dangling bond and the backbonded atoms that together constitute the defect. For broken dimer type defects the average distance between the Si dangling bond and the backbonded atoms does not correlate with the A_0 values. An average angle of roughly $110°$ is indicative of a high anisotropic hyperfine value — this indicates that at a certain buckling of the broken dimer structure the defects would present an EPR signal when not passified with hydrogen (an average angle of $120°$ would mean all the atoms of the defect structure are coplanar).

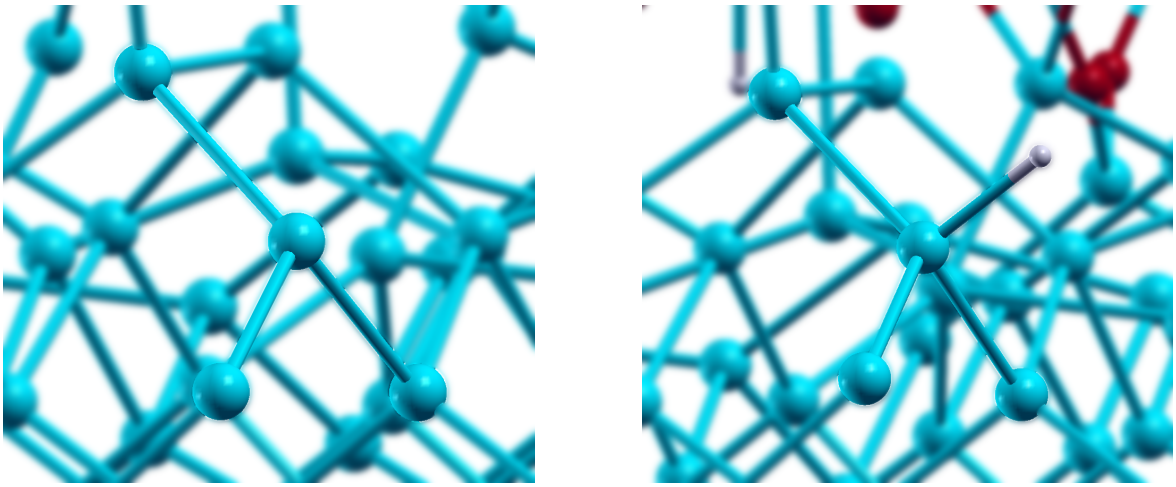

(a) P_{b0} dangling bond (b) Hydrogen passified P_{b0}

Figure 6.22: P_{b0} defect, found in the structure presented in figure 6.2b.

such defect in 1 of the 18 ~ 1.1 nm^2 analysed interfaces (each cell presents 2 Si/SiO_2 interfaces) is in agreement with the low density of 0.01 defects/cm^2 density generally given for P_{b0} defects.

sp^2 hybridised Si

One sp^2 hybridised Si atom was identified in an unoxidised Si cell (cell 3, figure 6.2c). This dangling bond is found in the second Si monolayer from the surface. It shares one bond with an

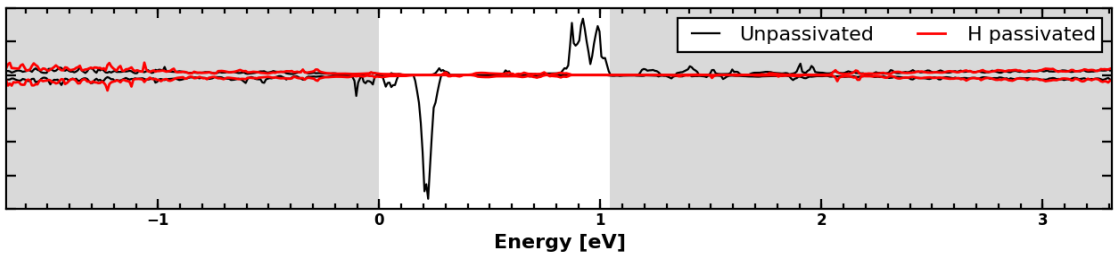

Figure 6.23: PDOS for P_{b0} defect. The red line represents the projected DOS of the hydrogen passified defect. Shaded areas represent the Si valence and conduction bands.

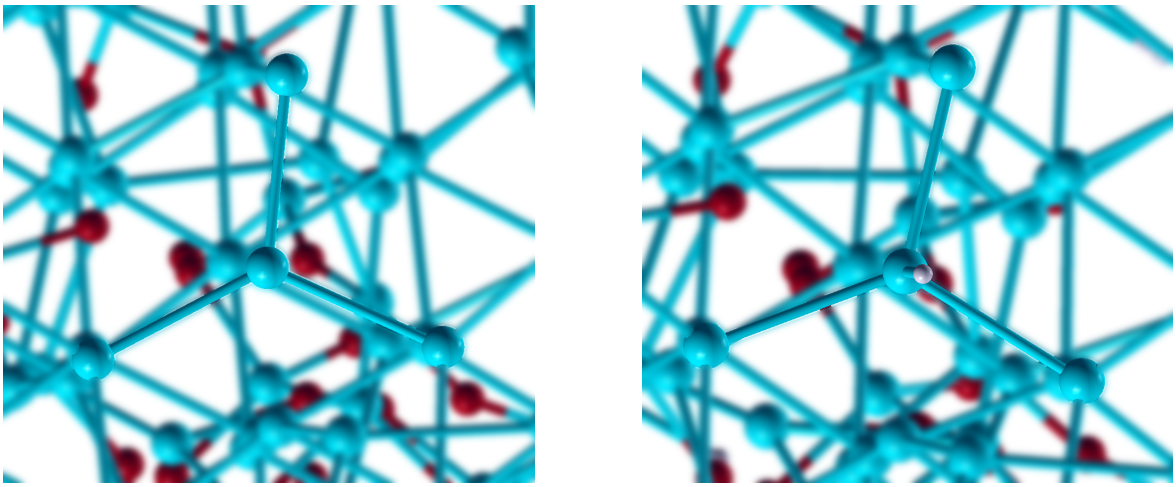

(a) sp^2 hybridised dangling bond

(b) Hydrogen passified sp^2 Si defect

Figure 6.24: sp^2 hybridised Si defect, found in the second interface monolayer of the structure presented in figure 6.2c.

Si from the interface monolayer, and two bonds with atoms from the bulk semiconductor. The defect has a spin moment of $0.49\ \mu_B$. The hyperfine calculated A_0 value is 1.9 mT, an order of magnitude lower than that of E' and broken dimer defects. The hyperfine axis of this defect deviates by only 4° from the $\langle 111 \rangle$ direction of standard P_{b0} defect. The atom projected density of states for this defect reveals delocalised states in the Si band gap, which shift to one very well localised defect in the mid gap region post passivation (shown in figure 6.25).

O-Si-O oxide bridges

A number of 2-fold coordinated Si atoms are observed in the inner oxide layers of our structures. Approximately 1 such defect was found in each structure. It is very likely that this high two-fold coordinated Si in the SiO_2 layer is a consequence of generating the coordinates of the amorphous oxide with the COMB potential. A richer O environment used in experimental techniques could also reduce significantly both the number of O-Si-O oxide bridges and that of E' defects. O-Si-O bridge defects present A_0 values as high as 18.5 mT and result in states in the Si gap. Passivating

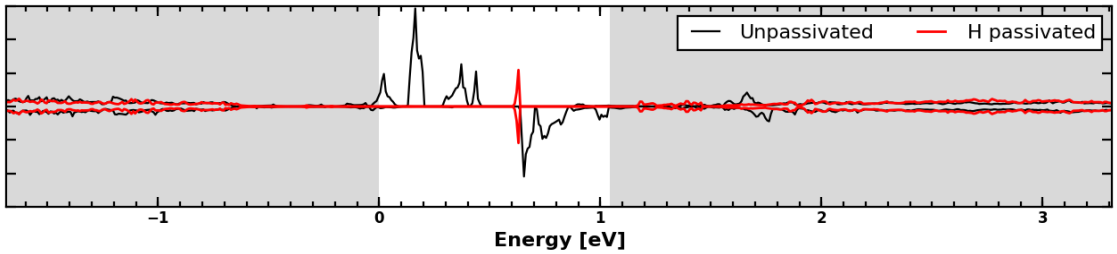

Figure 6.25: PDOS for sp^2 hybridised Si defect. The red line represents the projected DOS of the hydrogen passified defect. Shaded areas represent the Si valence and conduction bands.

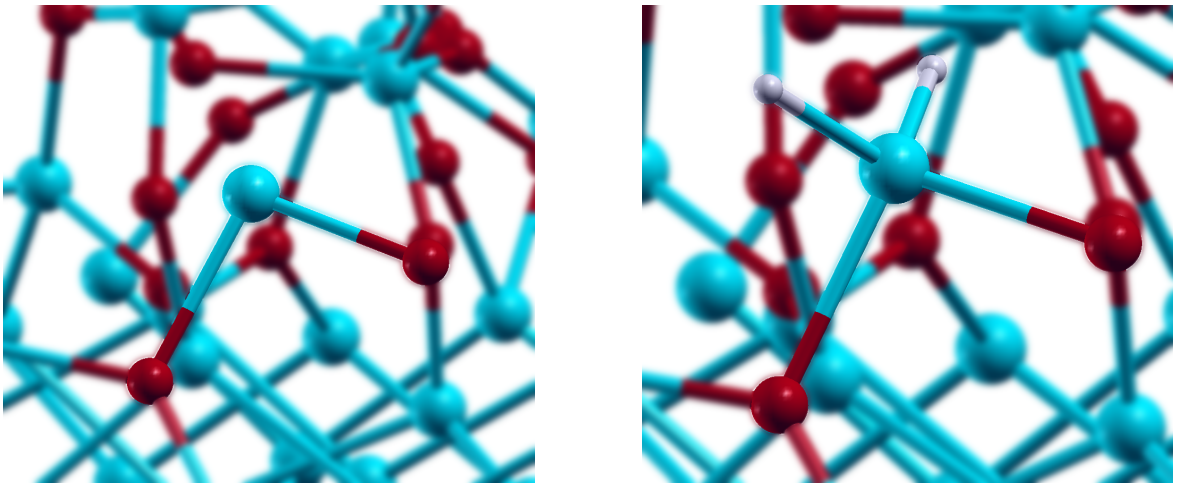

(a) Unpassified O-Si-O bridge

(b) Hydrogen passified O-Si-O bridge

Figure 6.26: O-Si-O oxide bridges found in the SiO_2 layer of our structures. Two hydrogen atoms are required for passifying such a defect

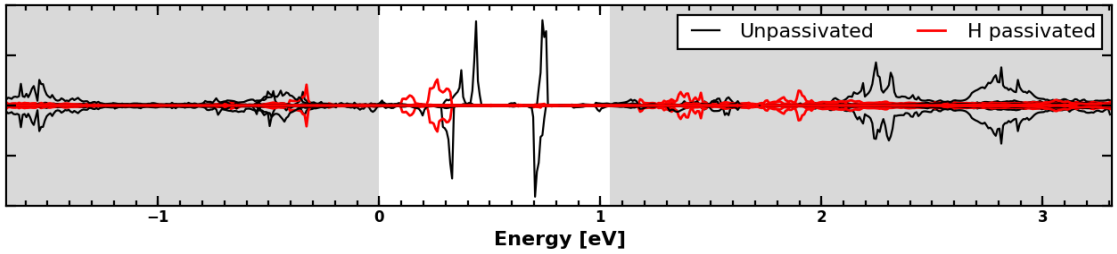

Figure 6.27: Atomic projected density of states for O-Si-O bridges in the SiO_2 oxide layer. The red line marks the PDOS of the passivated Si atoms. Shaded areas represent the Si valence and conduction bands.

such defects requires applying two H atoms in a plane perpendicular to the one determined by the coordinates of the Si atom and its two O neighbours (see figure 6.26).

6.5 Summary and Discussion

To the best of our knowledge the work presented in this chapter presents the first investigation of its kind into the nature of defects at Si/SiO_2 interfaces. The approach resembles the one taken by Giacomazzi and co-workers [21] in hunting down the types of E' defects in bulk amorphous SiO_2. This work also makes a strong case for the prevalence of dangling bonds at Si dimers and "broken dimer" structures — defects that have been discussed before in previous works as potential candidates for the structure of the P_{b1} defect. While the experimental works discussed in Chapter 3 point out that it is unlikely that the P_{b1} structure is either the dimer one or the broken dimer one, dimer and broken dimer defects could have an important effect in charge trapping and negative bias temperature instability phenomena.

The calculation of the effect of hydrogen in clearing the gap states and the relative effect it has on different types of defects at the $(001)Si/SiO_2$ interface is also a novel approach in *ab initio* studies on the Si/SiO_2 system. Theoretical studies dealing with hydrogen passivated defects have been discussed in Chapter 3, but none of them actually showed the effect in clearing the gap states

generated by individual defects.

Si/SiO_2 structures were simulated by generating coordinates for amorphous SiO_2 and manually placing it on top of a (001)Si slab. The geometry of the structures was then optimised using the PBE DFT functional and a single point calculation was run with a 5% hybrid DFT functional.

The aim of these calculations was to study the states localised in the Si gap region caused by point defects appearing at (001)Si/SiO_2 interfaces. As shown in Chapter 3, EPR experiments have clearly identified two types of defect at the Si/SiO_2 interface, P_{b0} and P_{b1}, both Si dangling bonds bonded to three Si atoms. The P_{b0} defect is clearly shown by EPR experiments to be an sp^3 hybridised Si with the dangling bond pointing in the $\langle 111 \rangle$ direction [5]. The P_{b1} defect was identified by Stesmans *et al* to be a threefold coordinated Si dangling bond pointing in the $\langle 211 \rangle$ direction [62]. Stirling *et al* compared three models for the P_{b1} defect, ultimately agreeing on a dangling bond centred on a Si atom bonded to two Si atoms from the semiconducting substrate and one Si from an SiO_3 tetrahedron with two oxygen atoms bonded to the Si surface. Other defects identified that affect the performance of transistors are E' defects – dangling bonds on Si atoms bonded to three O atoms. Several categories of E' have been identified in experiments, but finding their exact structure has been problematic [52, 21]. Another factor we chose to take into account was the influence of hydrogen in eliminating the gap states created by defects at the interface and bulk layers of the Si substrate.

The usual approach in studying defects at the Si/SiO_2 interface taken in the literature is either modelling P_b-type defects after EPR results [92] [98] or creating oxygen vacancies near the interface [88]. Even approaches using MD generated positions for the oxide atoms use a certain amount of manual bond matching between the oxide and the (001)Si interface [96]. Studies on E' defects exist for bulk SiO_2 where the structures are generated through MD techniques and then optimised and analysed with DFT methods [21, 77]. Similar to such studies on bulk SiO_2, we use MD techniques to generate the positions of the amorphous oxide which is then laid on (001)Si to observe the defects that are appearing at the interface during the DFT optimisation. While previous studies have focused on manually trying to replicate defects at Si/SiO_2 interfaces as described by experiments, this work aims to predict which defects are likely to form, and analyse the electronic properties of these defects and the effect hydrogen passivation would have on them.

Our approach does have a few drawbacks. First, the computational scaling of DFT methods requires us to use several small 148-170 atom cells for generating Si/SiO_2 interfaces. Second, we do not take into account the various ways in which the oxide deposition technique could influence the formation of defects. A full scale simulation of atomic layer deposition of chemical vapour deposition techniques are outside of the scope of this work. Previous studies on the oxidation of (2×1) reconstructed (001)Si surfaces do show that during the initial deposition of the oxide O atoms tend to get inserted into the surface Si dimer reconstructions rather than Si backbonds [63, 89]. The initial oxidation of the (001)Si surface was addressed in this work by running a set of calculations on structures which used a Si slab with oxygen inserted in between every pair of neighbouring surface Si. While obviously still no replacement for a full scale simulation of the oxide deposition process, this allowed us to estimate the effect of initial surface oxidation on the formation of defects.

Upon optimising slabs with the PBE functional and calculating the density of states with a hybrid functional, the suboxide density at the interface was compared to the experimental XPS data available in the literature [54]. Passivation of the dangling bonds in our structures required using density of hydrogen two orders of magnitude higher than the ~ 0.1 atoms/nm^{-3} observed in experiment [78]. One possible cause for the high number of defects observed could be the COMB10 [38] potential used in the MD simulation of an annealing process — as the ability of this potential to predict the equilibrium atomic position of atoms is somewhat limited. A second possible cause for the high defect density is lattice stress induced by the small cell size ($10 \times 10 \times 20$ Å). On the other hand, the large number of defects observed in this work allowed the identification of the recurring type of defects.

E'-type defects in the bulk layers of the SiO_2 were the most common defects observed. Their isotropic hyperfine A_0 values as high as 70 mT were obtained. The average Si-O bond distance and the average O-Si-O angle did not influence the A_0 values. E' defects created localised states in the mid-gap region of Si, strongly localised gap states near the Si VBM and states within the Si valence and conduction bands. Adding passifying hydrogen atoms on the E' Si dangling bond results in clearing the gap and valence band states, while still leaving charge traps in the Si conduction band. The diversity of gap states we observed for the E' defects could provide an

explanation for the charge trapping behaviour observed by Grasser *et al* [76], where the time such defects would hold charge trapped would vary by several orders of magnitude.

During optimisation using the PBE DFT functional, dimers at the top Si layers appeared, similar to the ones on clean (2×1) reconstructed (001)Si surfaces — however dimers on clean unoxidised Si surfaces are *not* paramagnetic. Dangling bonds on certain Si dimers from the Si/SiO_2 structures are paramagnetically active (having A_0 values up to 15 mT). Dimer defects in Si/SiO_2 structures can create states throughout the Si gap and localised states in the Si valence and conduction bands near the Si VBM and CBM. Hydrogen passivation effectively cleared out these localised states from the band gap. EPR experiments do not describe such defects. A dimer model was considered as a candidate for the P_{b1} defect by Stirling *et al* [92] but was eventually abandoned in favor of their asymetrically oxidised dimer model. The dimer defects from this work do not appear during the MD simulation with the COMB potential, but only after the PBE-level relaxation. Unoxidised (001)Si surfaces are known to form (2×1) dimer reconstructions, hence it is a reasonable assumption that such structures exist at actual Si/SiO_2 interfaces. Two reasons why EPR studies have failed to find such dimer defects are — (1) oxide deposition methods are incorporate O in most the Si dimers and (2) hydrogen passivation is significantly more effective on such defects than on P_b-type defects, making them invisible in both EPR and CV experiments. As such dimers still appear (though in smaller quantities) in Si/SiO_2 structures where an initially oxidised Si slab was used would indicate that dimer defects should form regardless of the oxide deposition method used.

The "broken dimer" type structure appears when a Si from the top monolayer bonds with one O from the oxide layer instead of a neighbouring surface Si or an O inserted into the (2×1) dimer. While such defects have been suggested in passing by Stathis and Cartier [18], they are not discussed in EPR literature. Our calculations show such defects to be paramagnetically active, having isotropic hyperfine terms up to 20 mT, especially when the average angle of the neighbours with the defect (i.e. two O-Si-Si and one Si-Si-Si angle) is around 110°. Broken dimer defects are less responsive to hydrogen passivation than E' or dimer defects, but hydrogen still removes states near the Si CBM and VBM. As in the case of the dimer defects, the reason broken dimers are not observed in EPR experiments from the literature could be an effect of the initial oxidation conditions used in practice.

Only one P_{b0} defect was observed in our Si/SiO_2 structures and no P_{b1} defect structure like the one described by Stirling *et al* were found. The P_{b0} is found in the second Si monolayer and the defect created two states in the Si band gap near the VBM and CBM regions. Adding a hydrogen on the defect effectively removed these two states. The fact that no Stirling P_{b1} structure is present in our cells leads us to conclude that further study is required into studying the creation of such defects. An initial study was carried out by Kato *et al* [171], but using a fully oxidised crystalline defect free model for Si/SiO_2 interfaces rather than presuming an amorphous oxide layer.

Chapter 7

Si/HfO_2 results

A total of four interface structures were created to analyse the topology of interfaces between crystalline silica and amorphous hafnia. A molecular dynamics simulation was performed to obtain the coordinates of the amorphous HfO_2 layer. The Si/HfO_2 structures were optimised at the DFT level. Hybrid DFT calculations were performed to analyse the electronic properties of the structures. Interface defects and defects from the near interface layer were identified.

7.1 Structure generation

A 96 atom HfO_2 cell was melted in a molecular dynamics process identical to the one described in section 5.3.2. A $2 \times 2 \times 2$ expansion of a 12 atom m-HfO_2 cell was used. The resulting x and y dimensions of the HfO_2 structure where both twice as large as the a and b dimensions of the monoclinic cells, while the z axis was fixed as double the projection of the monoclinic c axis on the normal to the ab plane. The COMB potential [39] was used in a 100 ps melting simulation at 7000 K. Three amorphous HfO_2 snapshots were chosen at random from the ensemble of amorphous structures obtained during the process. One of the snapshots was placed onto a clear 8 monolayer, 64 atom (001)Si slab. All three of the amorphous snapshots were also added

to a 10 monolayer, 72 atom (001)Si slab with inserted O atoms between neighbouring surface Si. The x and y dimensions were equal to 10.83 Å for the unoxidised Si slab and 11.02 Å for the oxidised Si slab. The horizontal x and y dimensions of the amorphous HfO_2 structures were scaled to fit the Si slab that they were placed into contact with. Four Si/HfO_2 interface structures were obtained – one using an unoxidised (001)Si slab and the others using an oxidised (001)Si slab. The unoxidised Si/HfO_2 cell (cell 1) contained 160 atoms in total, while the three oxidised Si Si/HfO_2 cells (cell 1 ox, cell 2 ox and cell 3 ox) contained 168 atoms each. A very short low temperature simulation using the COMB potential was run to relax short bonds before the DFT-level optimisation.

The PBE functional as implemented in the plane-wave CASTEP code [23] was used to optimise the four Si/HfO_2 interface structures. A $4 \times 4 \times 2$ mesh was chosen for the k-space sampling. A spin polarised calculation was performed to optimise the geometry of each slab. The x, y and z dimensions of the cell were allowed to relax while the cell angles were kept fixed at 90°. The amorphous and strained nature of the amorphous-crystalline interface makes it difficult to converge the minimum force between two atomic pairs in the system. Thus an energy stopping criterion of $dE/atom < 5 \times 10^{-4}$ eV was chosen for the geometry optimisation routine. The resulting structures are shown in figure 7.1. Figure 7.1a shows the unoxidised Si/HfO_2 structure while Figures 7.1b, 7.1c and 7.1d show the resulting oxidised interface structures.

As in the case of the Si/SiO_2 interfaces, a CRYSTAL [24] calculation was performed for each structure. The same basis sets used in Chapter 5 on bulk Si, SiO_2 and HfO_2 were chosen for the Si/HfO_2 interface structures [138, 142, 149]. A B3LYP(20%) spin polarised single point calculation was performed for each structure. The stopping criterion for the SCF calculation was a drop in the relative energy of the structures below 10^{-6} Hartree. All the electronic structure results presented in this chapter based these B3LYP self consistent field calculations.

7.2 Structural properties

The four total generated interface structures present a total of 8 interface layers between crystalline Si and amorphous HfO_2 (see figure 7.1). The x and y horizontal dimensions of the structures are slightly smaller than the ones of the Si/SiO_2 interface structures with an average of approximately 10.5 Å. The vertical z axis is 21.67 Å for the unoxidised structures and for the oxidised ones structures – which contain an extra two monolayers of crystalline Si – the z axis ranges between 21.91 Å and 22.74 Å.

Although the same configuration was used for the coordinates of the amorphous HfO_2 layer for cell 1 (figure 7.1a) and cell 1 ox (figure 7.1b) the final configuration of the amorphous oxide layer in the two structures is visibly different. The fact that one structure was created with an unoxidised Si slab and the other with an oxidised Si slab results in a different configuration for the interface atomic layers. This effect was also noticed for Si/SiO_2 interfaces in the previous chapter. This effect could be caused either by the different initial pressure at which the amorphous layer was manually added on the slab, the erratic behaviour of the COMB potential for HfO_2 structures, or the fact that the HfO_2 slab is too thin to present an actual bulk phase.

The density profile for HfO_2 cells was calculated and it is shown in figure 7.2. As in the case of Si/SiO_2 structures the $\rho(z)$ density value vas calculated as the sum of the atomic masses for atoms in the interface structure with the z coordinate in a $[z - dz : z + dz]$ interval and divided by the volume $2 \cdot S \cdot dz$ where $dz = 1.15$ Å and S is the cross section of the interface. A Gaussian smoothing filter of $\sigma = 7.4$ Å on 2.6 Å windows was applied to the graph. The average density of the Si slab for the interface structures follows the average density of bulk Si (2.32 g/cm^{-3}), a smooth transition layer is observed at the interface between the semiconductor and the oxide, and the bulk HfO_2 oxide density varies between that of m-HfO_2 (9.68 g/cm^{-3}) and the density we obtained for the amorphous HfO_2 structure (10.87 g/cm^{-3}) (see section 5.3.2). There is no significant difference in the density profile of the unoxidised Si cell (cell 1) and the density profile of the oxidised cells (cell 1-3 ox) in the semiconductor-oxide region. This could be because oxygen is more mobile inside HfO_2 than inside SiO_2. We observed that, upon optimisation, O atoms in the unoxidised Si cell were adsorbed into the surface Si monolayers. This oxygen exchange from the

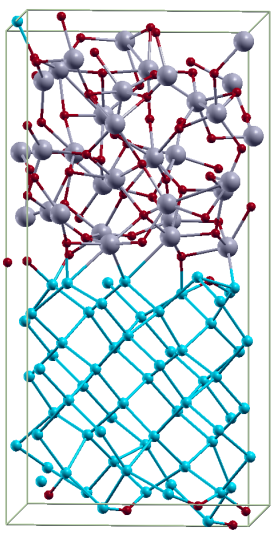

(a) Cell 1

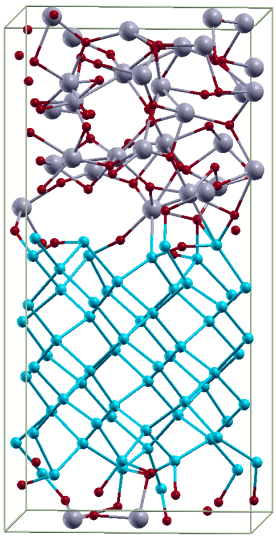

(b) Cell 1 (oxidised)

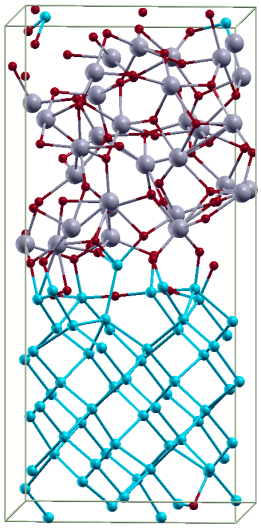

(c) Cell 2 (oxidised)

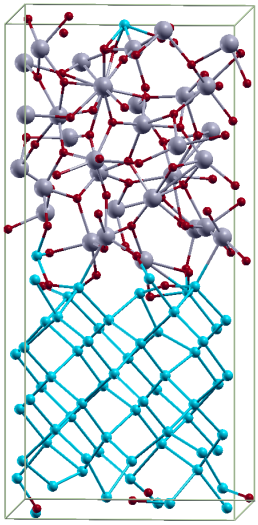

(d) Cell 3 (oxidised)

Figure 7.1: PBE-optimised structures for Si/HfO_2 interface structures. The PBE optimisation created dimers in Cell 1 and Cell 2 (oxidised). A unoxidised Si slab was used for cell 1 (subfigure a) and an initially oxidised Si slab for the cells shown in subfigures b,c and d.

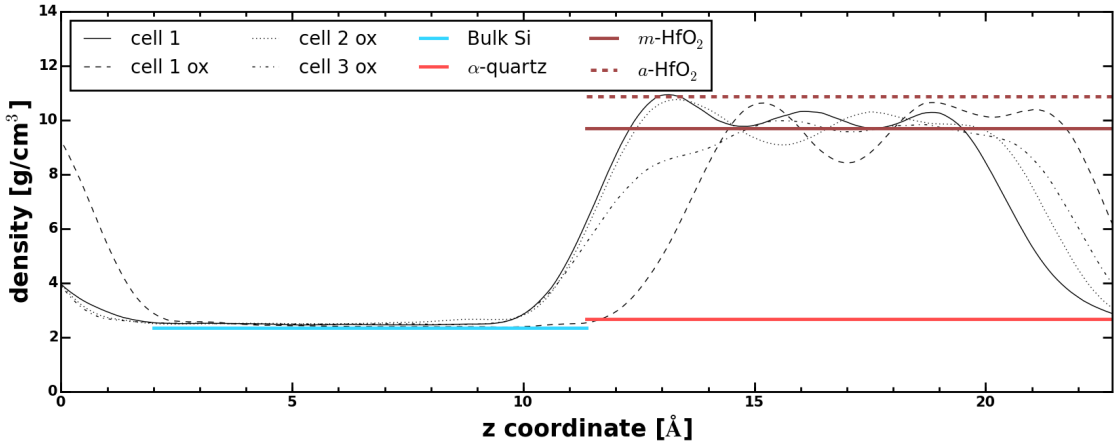

Figure 7.2: Density profile along the vertical z axis for structures created with an initially oxidised surface. The experimental value for the density of Si, α-quartz and m-HfO_2 [144] are shown in blue, red and purple respectively.

HfO_2 layer towards the Si substrate has been experimentally observed [172] [173] and confirmed by theoretical calculations [117] [128].

The coordination of Hf atoms was considered. In monoclinic hafnia, Hf atoms are sevenfold coordinated, each Hf atom having 7 neighbouring oxygen atoms at a distance smaller than 2.4 Å. For our analysis we considered Hf atoms to be N-fold coordinated if they have N O neighbours within a 3 Å radius. We chose a larger coordination sphere for Hf than the previous studies summarised in section 4.2 as we found Hf-Hf interactions to produce gap states, even when the distance between the Hf pair is larger than 2.35 Å. The Hf-O and Hf-Hf coordination number distributions for Si/HfO_2 interface structures and the previously discussed HfO_2 amorphous structure are shown in figure 7.3. A given Hf atom's Hf-X (X is Hf, O or Si) coordination is n if it has exactly n X atoms at a distance < 3 Å. We observe a normal distribution for the Hf-O coordination of the two structures. Hf atoms in bulk amorphous HfO_2 have a higher O coordination than the ones in Si/HfO_2 structures. The coordination of Hf atoms in bulk HfO_2 is consistent with MD calculations on amorphous hafnia (density 10.6 g/cm^{-3}) of Broglia *et al* [125], though Broglia and co-workers did not provide the cut-off radius they used. Chen and Kuo's *ab initio* results on

amorphous HfO_2 on a similar 96 atom cell but having a density of 8.6 g/cm^{-3} show a prevalence of 6-fold coordinated Hf atoms. Kaneta and Yamasaki [122] calculate the average coordination number of Hf in MD melted hafnia to be to be 5.7 for a 2.35 Å cutoff, which is quite similar to the average Hf coordination of 5.6 we obtained using the same cutoff for our bulk HfO_2 cell. The lower average Hf coordination we observe in the Si/HfO_2 interface structures could be attributed either to oxygen adsorption in Si monolayers or a larger volume that the HfO_2 can occupy in an Si/HfO_2 structure — as an extra amount of volume is added to the cell when manually positioning the HfO_2 oxide layer on top of the (001)Si slab. The Hf-Hf coordination distribution is shown in figure 7.3b. While the bulk amorphous HfO_2 structure has only one Hf-Hf pair, such Hf-Hf bonds are far more prevalent in the Si/HfO_2 structures, as more than 30% of the Hf atoms have at least one Hf in the 3 Å coordination shell. As mentioned in Chapter 4, Si has a higher affinity for O than HfO_2 and O tends to get adsorbed at the Si surface leaving oxygen vacancies in the bulk of the oxide.

The radial pair distribution $g(\mathbf{r})$ function was calculated for the four structures. Given that the structures contain three types of atoms, there is a total of six contributions (Hf-Hf, Si-Si, O-O, Hf-O, Hf-Si, Si-O) to the pair distribution. Figure 7.4 shows the total pair distribution function and a breakdown of the contribution of each pair type. The Si-O peak covers the $1.6 - 1.7$ Å region, similar to the pair distribution function of SiO_2 and Si/SiO_2 interface structures. Hf-O peaks are centred in the 2 Å region followed by the Si-Si pair contribution from the bulk Si layer centred around 2.3 Å. O-O pairs are less correlated, and the mark of Hf-Si and Hf-Hf pairs is minute. This shows that no significant Hf-Si bonding across at the Si/HfO_2 interface. As mentioned before, an intermediate layer of Hf silicate is experimentally known to form at interfaces between crystalline silicon and amorphous hafnia. Amorphous HfO_2 is known to crystallise at low temperature, an effect which is averted through the insertion of nitrogen and other impurities that prevent the amorphous HfO_2 structure from reverting back to a crystalline state [99]. While amorphous HfO_2 reverted to a crystalline state when annealing with the COMB potential, DFT optimisations of high temperature snapshots resulted in amorphous structures.

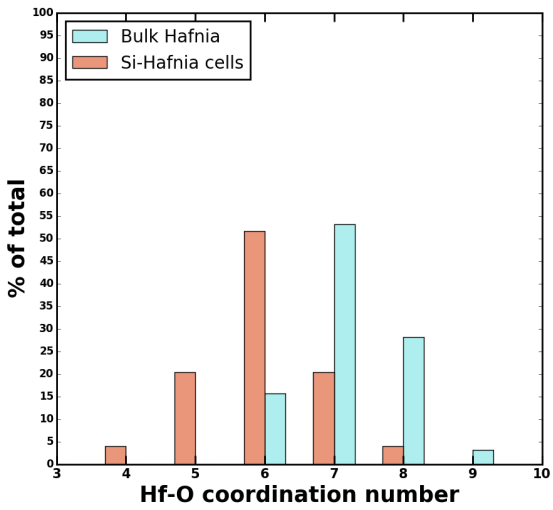

(a) Hf-O coordination represents the number of O atoms found in a 3 Å sphere around a given Hf atom.

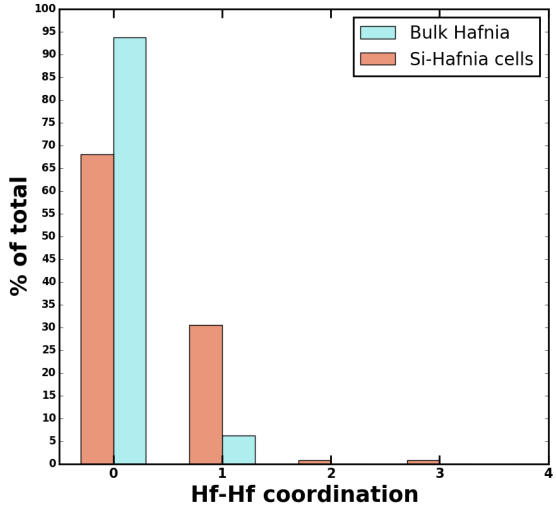

(b) Hf-Hf coordination represents the number of Hf atoms found in a 3 Å sphere around a given Hf atom.

Figure 7.3: Barcharts showing the distribution of Hf coordination in the Si/HfO_2 interface structures and amorphous HfO_2 cell. Figure (a) shows the Hf-O coordination — Hf atoms in the more dense HfO_2 structure tend to have a higher number of O atoms within a 3 Å radius. Figure (b) shows the distribution of Hf neighbours withing a 3 Å radius — our bulk HfO_2 structure only presents one Hf-Hf pair.

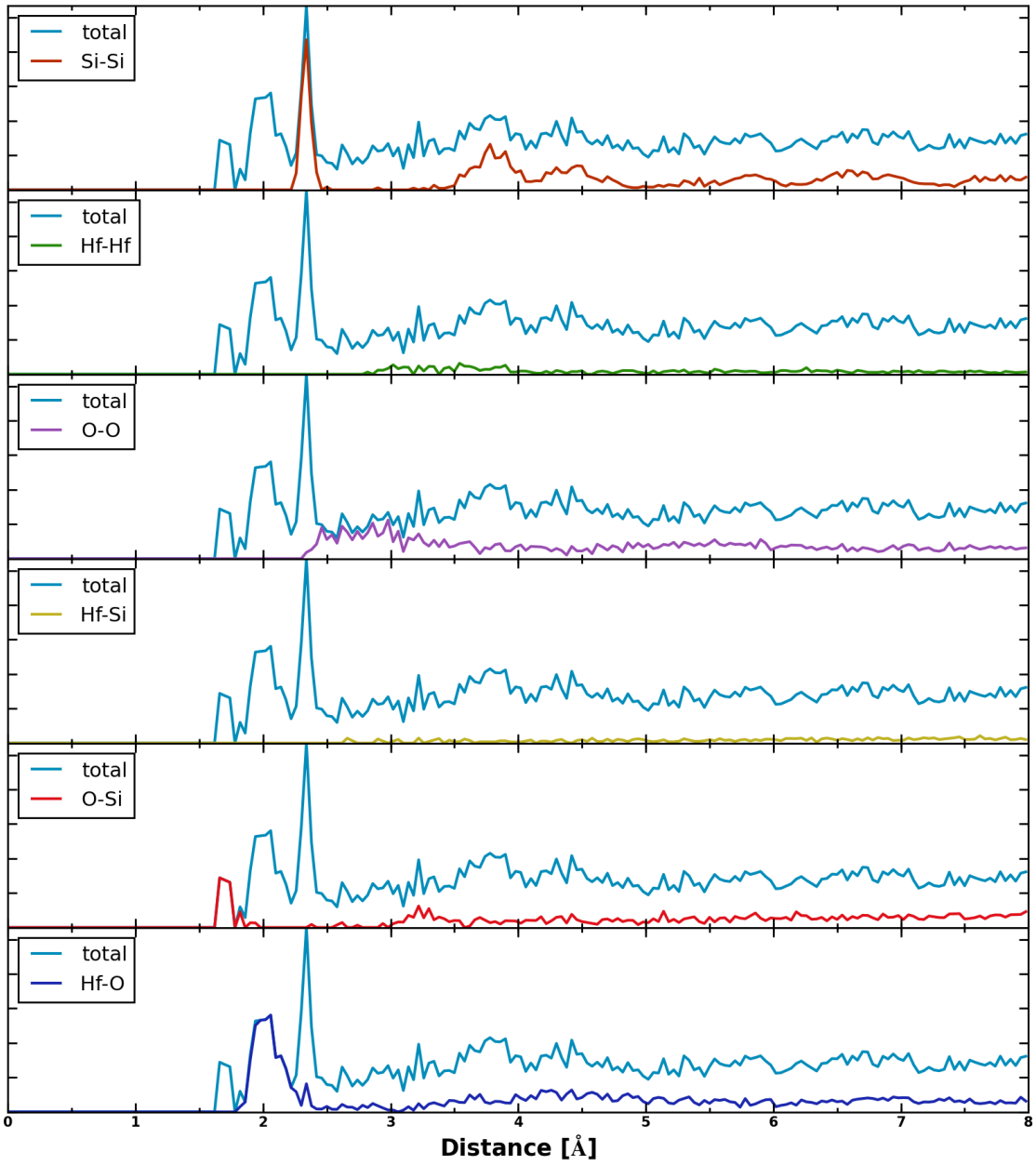

Figure 7.4: Pair distribution function calculated for the Si/HfO_2 structures (see figure 7.1). The contribution of each type of pair to the total pair distribution function is shown.

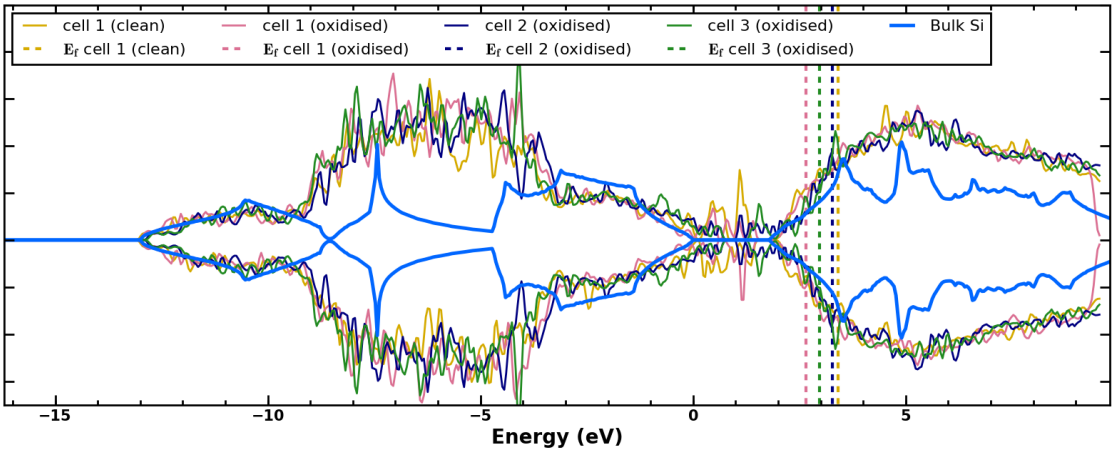

Figure 7.5: Total density of states for Si/HfO_2 structures calculated at the B3LYP(20%) level. The total B3LYP(20%)-level Si DOS is shown for reference. The total DOS presents an offset which forces the gap of interface structures above the conduction band of bulk silicon. For this figure the 0 eV level is set to the Si VBM. The DOS of the Si/HfO_2 interfaces was aligned at the bottom of the Si valence band.

7.3 Electronic properties

The density of states from the B3LYP(20%) calculation with the Figgen basis set was obtained for the four Si/HfO_2 interface structures and it is shown in figure 7.5. We observe that the Fermi level and the band gap for the Si/HfO_2 structure is pushed above that of the bulk Si B3LYP conduction band minimum. This does not seem to be in agreement with the relative offsets of bulk Si, mononclinic and amorphous HfO_2 previously calculated and presented in section 5.3. If controlled for this offset the total DOS of Si/HfO_2 interfaces does reduce to a superposition of the bulk Si, amorphous HfO_2 and defect level gap states, similar to the total DOS of the Si/SiO_2 structures was a superposition of Si, SiO_2 and defect states.

The atom projection of the Si atoms in inner layers of the Si slab is used to determine the valence band maximum (VBM) and the conduction band minimum (CBM) of the interface structures. The density of states for near the gap region for the four Si/HfO_2 structures is shown in figure 7.6.

For reference, the 0 eV level was set at the structure's VBM. The cell 1 and cell 1 ox structures present a spin polarisation while cell 2 ox and cell 3 ox have an identical spin up - spin down density of states. The absolute position of the Fermi level varies from cell to cell by 0.7 eV. It has been shown in Chapter 5 that bulk Si and bulk (monoclinic and amorphous) HfO_2 have a defect free gap region. This leads us to observe that, as was the case for Si/SiO_2 interface structures, the presence of the interface layer causes such gap states to appear. Unlike Si atoms in SiO_2, Hf atoms in HfO_2 have more variability in their O coordination and do not tend to form clear bonding patterns such as the the tetrahedra present in SiO_2. As shown in section 4.2 Hf-Si bonds have also been shown to create interface states, and we should also account for them.

The contributions of Hf atoms with various degrees of O coordination to the total DOS of Si/HfO_2 interface structures is shown in figure 7.7. The summed atom projected DOS contributions of Hf atoms of a given contribution are summed and the 0 eV level is set at the VBM. Sixfold O coordinated Hf atoms are shown to produce the largest number of states above the VBM with clear sharp localised states — however it must be taken into account that sixfold coordinated O atoms appear more frequently than all the other Hf atom coordinations combined. Fivefold coordinated Hf atoms create more diffuse states throughout the gap. As shown in the Hf-O coordination distribution chart from figure 7.3a, the relative frequency of fivefold and sevenfold coordinated Hf atoms is relatively similar. Figure 7.7 shows that fivefold O coordinated Hf atoms are way more likely to produce states throughout the gap region than sevenfold coordinated Hf. Fourfold and eightfold O coordinated atoms also are equally likely to appear in our structures, but a clear symmetry exists in the number of gap states they produce — fourfold O coordinated Hf atoms produce clear localised peaks in the gap region while eightfold coordinated Hf atoms contribute the least to the distribution of gap states.

Clearly having a high O coordination is a significant factor in reducing the number of gap states produced by Hf atoms. In order to accurately determine the effect of various coordination numbers for Hf atoms in producing gap states we computed the relative contributions to the band gap for each individual atom. Figure 7.8 shows the the average integrated atom projected DOS between the VBM and CBM for each individual atom of a given O coordination. The average value of the

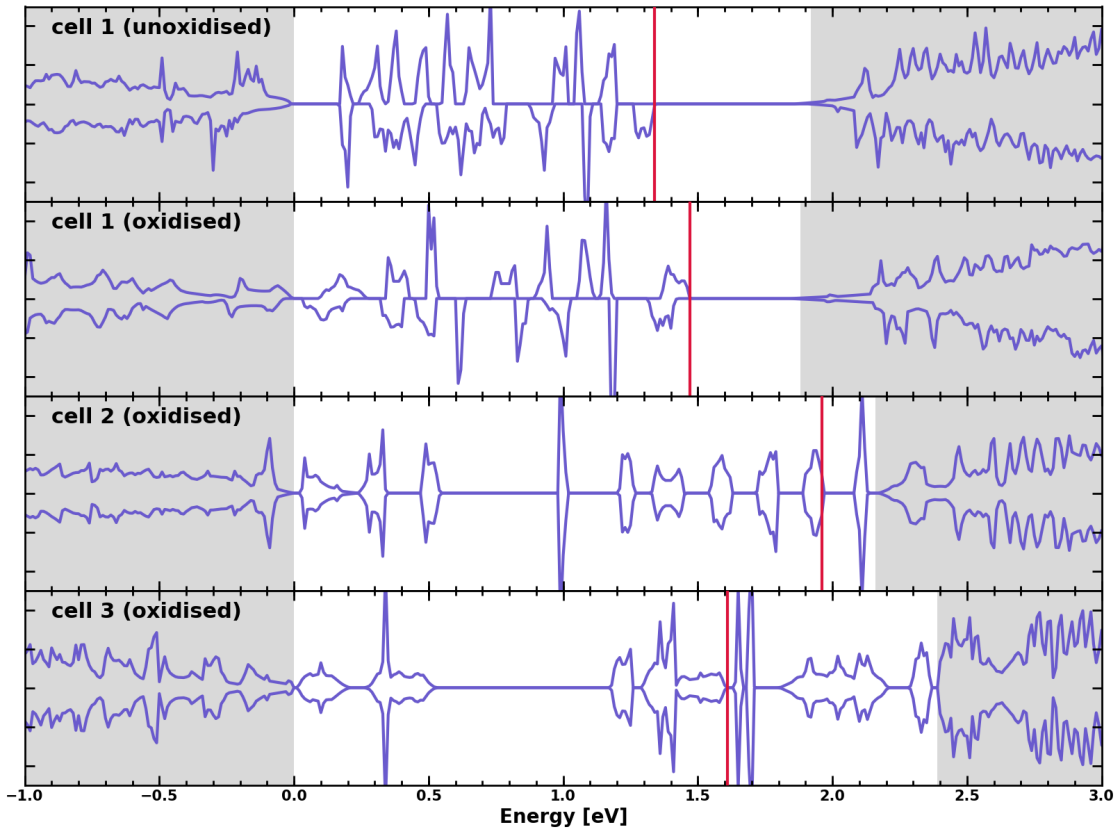

Figure 7.6: Gap density of states for Si/HfO_2 interface structures calculated at the B3LYP(20%) level. The Fermi level for each structure is marked with a red line. The 0 eV level marks the VBM for each individual structure. Shaded areas represend the valence band and the conduction band regions for the Si/HfO_2 interface structures.

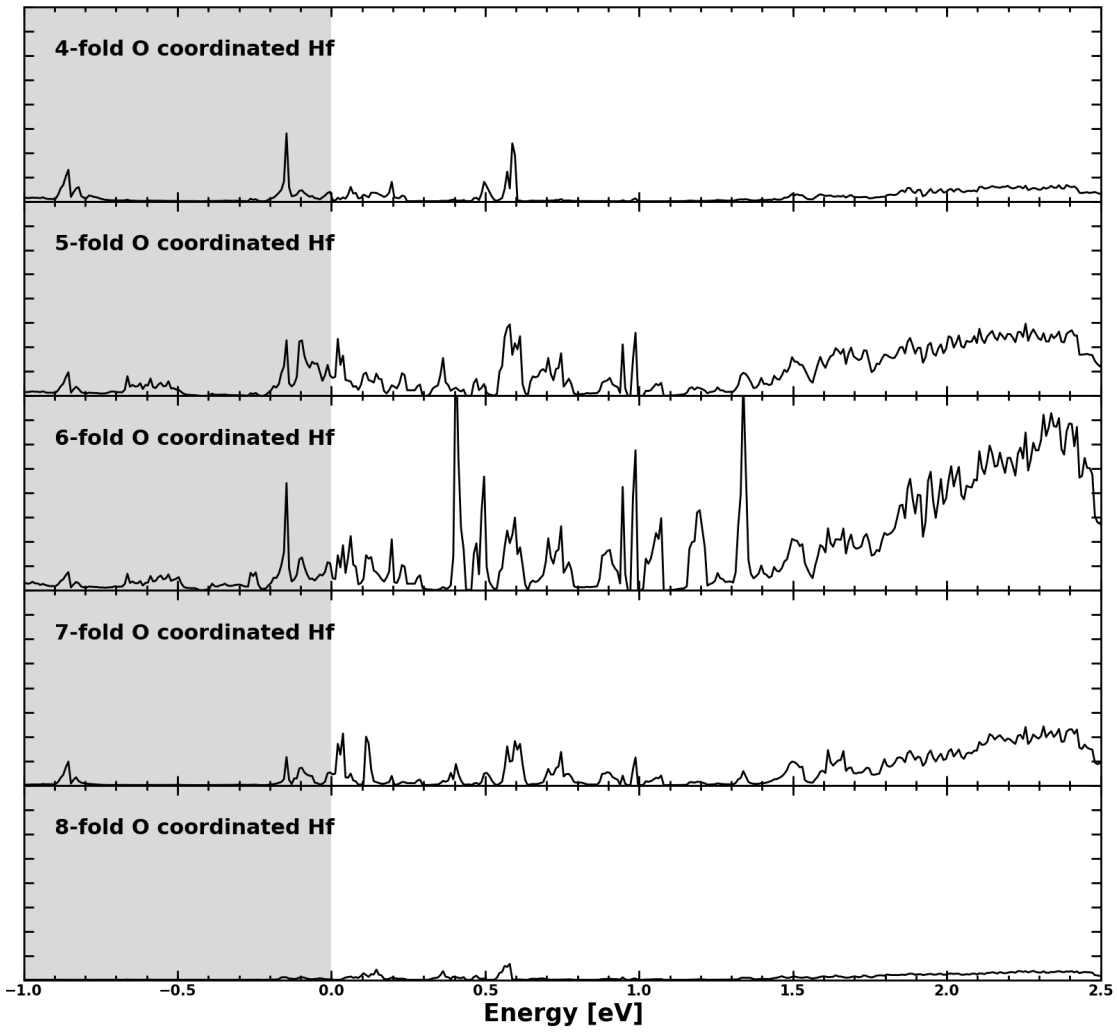

Figure 7.7: Hf DOS contribution for different O coordination values. A coordination sphere of 3 Å is considered around each Hf atom and the coordination number represents the number of O atoms within that sphere. The contribution is summed for each coordination number. The zero eV level represents the VBM for each structure and the shaded area marks the valence band.

integrated dos ($\bar{\Omega}$) for atoms of coordination k[1] is

$$\bar{\Omega} = \frac{1}{N} \sum_{i}^{N} \int_{\mathrm{VBM}}^{\mathrm{CBM}} \mathrm{PDOS}_i(E) \tag{7.1}$$

where the index i iterates over all N atoms of coordination k, averaging over the integrals between the valence band minimum and conduction band maximum of the projected density of states of k-fold coordinated atom i $(\mathrm{PDOS}_i(E))$. It is immediately obvious that having a full oxygen coordination is paramount in decreasing the number of gap states, as the average value of the integrated Hf atom projected gap DOS decreases with higher O coordination numbers. An Hf atom with 4 oxygen atoms in its coordination sphere is very likely to create gap states when having another Hf or Si atom within 3 Å. Hf atoms with an O coordination of 7 or 8 are roughly as likely to produce gap states. Sixfold O coordinations for Hf atoms are also present in amorphous HfO_2 (cf the distribution in figure 7.3a). As bulk amorphous HfO_2 has a clear band gap, this leads to the conclusion that mere sixfold O coordination for Hf atoms is not enough to explain the creation of gap states. The majority of sixfold coordinated Hf atoms that produce states in the band gap above the average level of sevenfold and eightfold coordinated Hf atoms have at least one Hf within their coordination sphere – which leads to the point that for Hf atoms with an O coordination larger than 6 is effective at screening out the interaction with other Hf atoms.

In analysing the effect of Hf-Si bonding for creating interface states we calculated the DOS contribution of Si atoms with at least one Hf atom within a 3 Å coordination shell. We observed that the presence of a Si atom within the 3 Å coordination shell of a Hf atom does not necessarily result in the formation of a gap state. As shown in Chapter 4, theoretical studies on (001)Si interfaces with monoclinic and cubic HfO_2 show that choosing an interface that bonds surface Si to Hf atoms in stead of O atoms from the oxide results in metallic states [127]. During the PBE optimisation oxygen migrates from the HfO_2 layer to the Si surface. Figure 7.10 shows the oxygen mass density profile along the vertical z axis of the interface structures with the oxygen mass density in the amorphous HfO_2 structure shown for reference. The oxygen density in the structures is lower and more spread on the vertical axis than the one in amorphous HfO_2 regardless

[1] i.e. the average number of states generated by an atom of coordination k

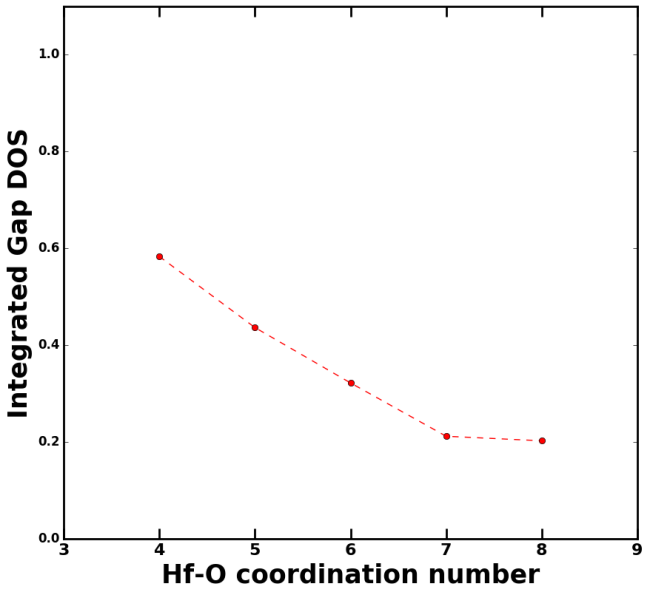

Figure 7.8: Average integrated projected gap DOS for diferent coordinations of Hf atoms as per equation 7.1. Hf atoms are sevenfold coordinated in m-HfO_2. Hf atoms in Si/HfO_2 interface structures are more likely to produce significant gap states if their coordination number is less than 7.

of whether an initially oxidised Si slab was used or not. The immediate conclusion would be that O atoms adsorbed at the Si interface prevent Hf-Si bonds from creating gap states. The O migration does have the effect of favouring the creation of Hf-Hf bonds in the oxide as well as fourfold and fivefold coordinated Hf atoms which are more likely to create gap states.

7.4 Paramagnetic defects

A calculation of the isotropic A_0 hyperfine parameter was run for the four HfO_2 interface structures. Only the cell 1 and the cell 1 ox structures had spin polarised solutions after the B3LYP(20%) SCF optimisation. The distribution of A_0 values for Hf, O and Si atoms is shown in figure 7.11. All the Hf values observed are zero. As previously mentioned in Chapter 4 experiments show that Hf-centred paramagnetic defects exist [110, 111]. Null Fermi contact terms for Hf atoms are obtained because all Hf s-type orbitals are covered by the Hay-Wadt effective core potential used. The valence electrons left treated with the basis set [149] don't have an s-type components, and thus don't contribute to the hyperfine anisotropic term.

A single atom has a significant A_0 value (27.8 mT), and that is a surface Si dangling bond from cell 1 ox (full interface structure shown in figure 7.1b). The atom is a typical broken dimer type structure such as the ones discussed in section 6.4.3, its bonded to two substrate Si atoms and one oxide oxygen. This defect produces one localised mid gap state in the cell 1 ox Si/HfO_2 interface structure DOS.

7.5 Summary and Conclusions

The geometry and electronic properties (001)Si/HfO_2 interfaces was studied. MD techniques were used to generate the atomic positions of the amorphous HfO_2 layer. A total of four Si/HfO_2 interface structures were created and their geometries optimised at the PBE level. A single point B3LYP calculation was run to calculate the density of states for each structure. The B3LYP(20%) functional was chosen because it accurately predicts the band gap of monoclinic and amorphous

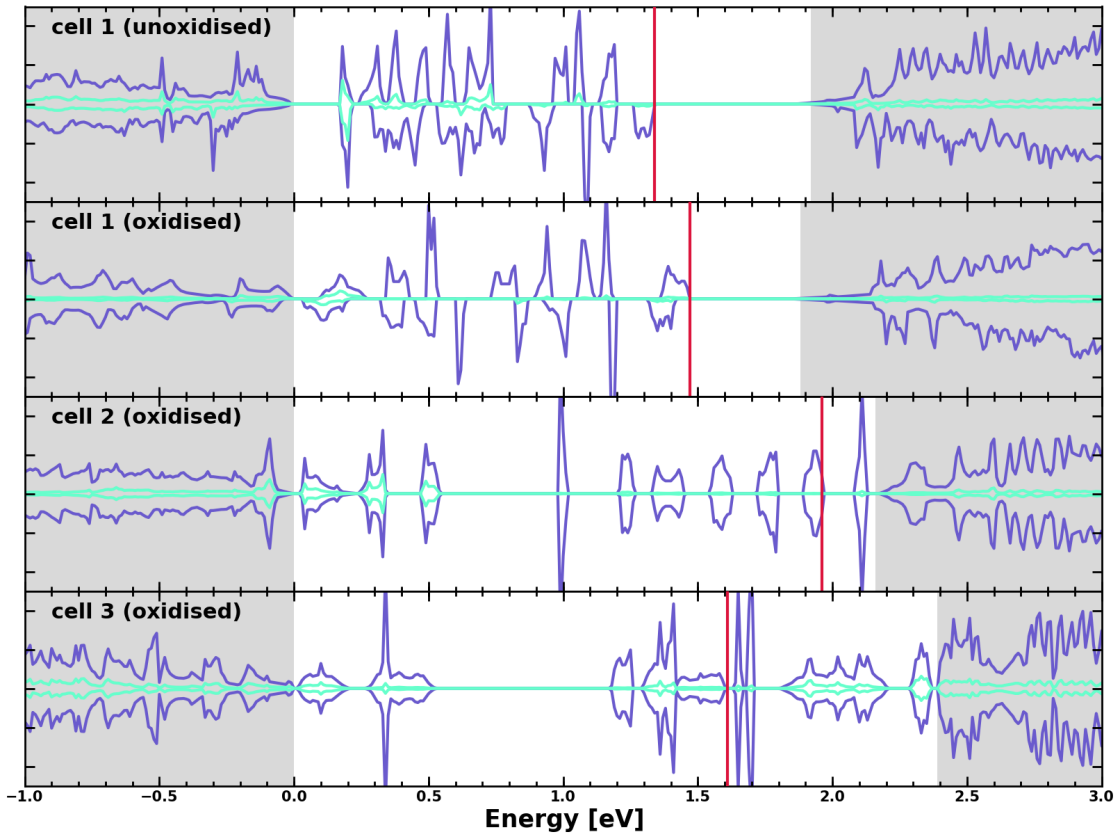

Figure 7.9: Contribution of Si atoms bonded to oxide Hf (i.e. Si atoms with at least one Hf in their 3 Å coordination shell) to the gap density of states for Si/HfO_2 interface structures calculated at the B3LYP level. The Fermi level for each structure is marked with a red line. The 0 eV level marks the VBM for each individual structure. Shaded areas represend the valence band and the conduction band regions for the Si/HfO_2 interface structures.

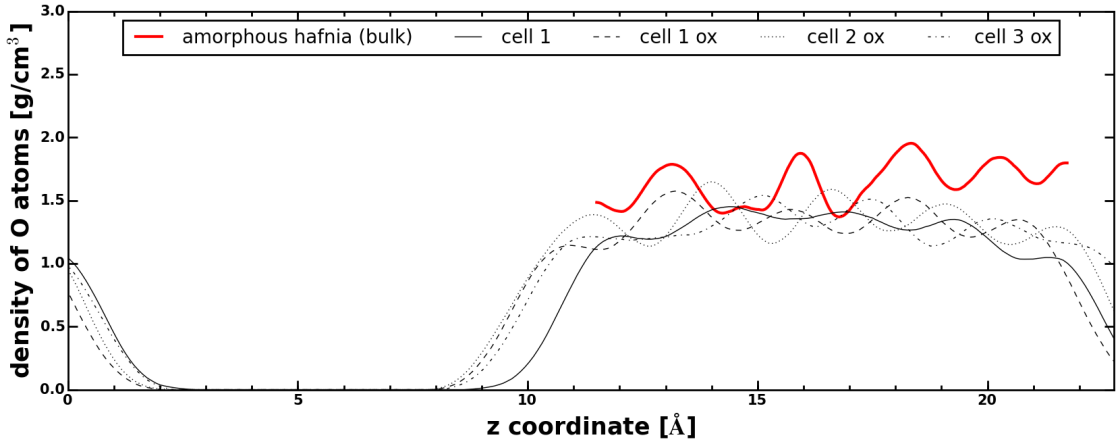

Figure 7.10: Density profile for oxygen atoms along the vertical z direction. The red line shows the oxygen density in our amorphous HfO_2 is shown in red line. Oxygen density is lower than in the bulk HfO_2 structures, as oxygen tends to be adsorbed by the Si slab.

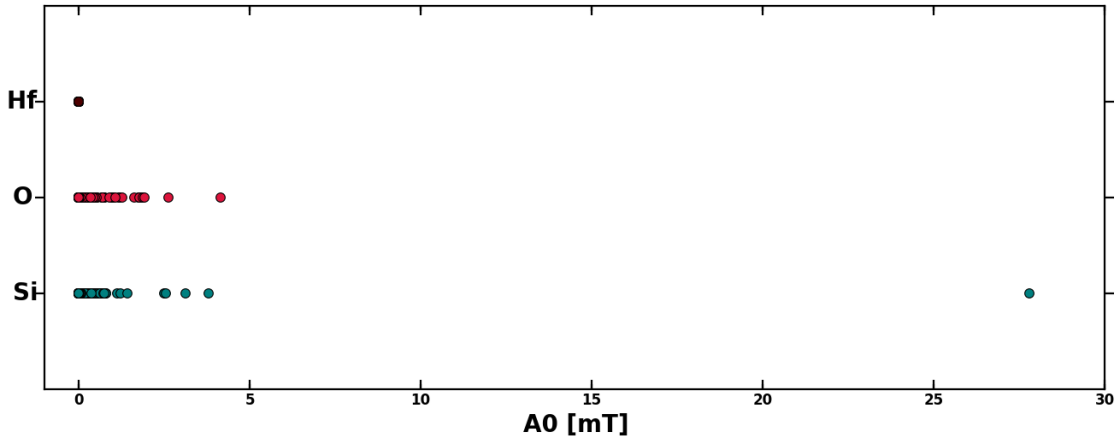

Figure 7.11: Distribution of A_0 values calculated for Si/HfO_2 interface structures. The Hf atoms were treated with a Hay Wadt effective core pseudopotential which covered all the orbitals that would contribute to the isotropic part of the hyperfine tensor.

HfO_2 (see Chapter 5 for details on the calculations).

The aim of these studies was to observe which defects are likely to cause gap states in Si/HfO_2 interfaces. EPR experiments detected only P_{b0} and P_{b1} defects at the interfacial SiO_2 layer forming at the interface between Si and hafnia [105]. The atomic structure of defects from the bulk amorphous HfO_2 has not been identified yet [110, 111]. Previous first principles studies on defects in Si/HfO_2 interfaces focused on calculating formation energies and density of states of different charged states of the oxygen vacancy [129, 131]. As Si/HfO_2 interfaces with no interfacial SiO_2 layer formation have recently been obtained [116], an understanding of the effects of the interface on defect formation is needed.

Atoms in amorphous HfO_2 do not have a strong tendency to form ordered local structures, such as the SiO_2 tetrahedra. A coordination sphere of 3 Å was considered to check the coordination of Hf atoms. A range of O coordination numbers was found for Hf atoms, from fourfold to eightfold, with sixfold O coordinations atoms being most common. 30% of the Hf atoms in our structures had at least one Hf atom in their 3 Å coordination shell, while only one pair of Hf atoms is present in the amorphous HfO_2 structure.

Defect states are present in the band gaps of the Si/HfO_2 interface structures. It was shown in Chapter 5 that bulk Si and bulk HfO_2 structures have a band gap free of defect states. Hf atoms with coordinations lower than 7 are shown to be more likely to create gap states. Sixfold O coordinated Hf atoms that have a larger contribution to gap states than the average for sevenfold and eightfold O coordinated Hf atoms also are more likely to have one Hf in their 3 Å coordination radius. This leads to the conclusion that Hf-Hf coordination is a stronger factor in creating gap states than creating oxygen vacancies in the amorphous hafnia layer.

A single Si atom was found to have a significant Fermi contact term — it formed a defect bond of the "broken dimer" type, where a surface Si from the (001)Si interface is bonded to an O from the oxide rather than form a (2×1) reconstruction with another surface Si, like the defect discussed in section 6.4.3 for Si/SiO_2 interfaces.

Hf atoms with non-zero Si coordination numbers were not more likely to cause gap states than

other Hf atoms. Analysing the atom projected DOS of surface Si with Hf in their 3 Å coordination shell revealed that they only contributed in small part to the overall gap DOS. However, Hf-Si bonds have been shown to create metallic states in Si/HfO_2 interfaces in previous studies [127]. An explanation for this could be the migration of oxygen atoms near the (001)Si surface layer. Oxygen atoms in amorphous HfO_2 have been shown to migrate towards the interface layer [126].

A conclusion is made that higher oxygen affinity of the (001)Si surface relative to the oxide has the effect of absorbing oxygen atoms from the HfO_2 layer and eliminate the surface dangling bonds likely to cause gap states, while also having the negative effect of depleting the hafnia layer of oxygen, resulting in undercoordinated Hf bonds likely to create interface states.

Chapter 8

Conclusion

In this work we investigated the structural and electronic properties of semiconductor oxide interfaces by using Si/SiO_2 and Si/HfO_2 model interface structures using molecular dynamics and first principles methods. The results of this work deepen the understanding of the complex landscape of defects at silicon-silica and silicon-hafnia interfaces. This work shows that defects on (2×1) dimer reconstructions and broken-dimer (O-•Si=Si) type defects are quite common at Si/SiO_2 interfaces. This work also presents a first *ab initio* look into interfaces between crystalline Si and amorphous hafnia and shows that oxygen migration towards the Si/HfO_2 interface leaves undercoordinated Hf atoms in the oxide layer which cause gap states. To the best of our knowledge, this work is also the first to show the individual contribution of various types of defects on the density of states Si/SiO_2 and Si/HfO_2 interface structures.

First the electronic structure of bulk Si and crystalline and and amorphous SiO_2 and HfO_2 were analysed. As our hybrid density functional theory calculations on bulk structures yielded good agreement with previously published experimental and theoretical results we proceeded to analyse full 148-170 atom Si/SiO_2 and Si/HfO_2 structures. Molecular dynamics techniques were used to generate the coordinates of the amorphous oxide layer. The structures were optimised at the PBE level. For the Si/SiO_2 structures a 5% Hartree Fock mix hybrid functional — B3LYP(5%) — was used to analyse the electronic structure. The B3LYP(20%) functional was used to analyse the

electronic structure of the Si/HfO_2 interface structures.

Recurrent defects were identified in the Si/SiO_2 structures. During the PBE-level optimisation (2×1) dimer reconstructions appeared at the (001)Si surface. Inserting oxygen atoms in the Si slab before the optimisation reduces the overall number of interface Si dimers, but does not completely eliminate their formation. The most frequently identified defects in Si/SiO_2 interfaces are E' defects, Si dangling bonds on (2×1) dimer reconstructions and "broken dimer" type structures, where a Si from the top most Si layer bonds with an oxygen atom from the oxide layer instead of forming a dimer with a surface Si. All these defects produce localised states in the Si band gap region. Passivating hydrogen was added on undercoordinated atoms in the Si/SiO_2 interface structures. Hydrogen passivation is extremely effective in clearing the gap states produced by E' type defects within the bulk layer of the oxide and Si dimer dangling bond defects at the (001) Si surface. Hydrogen passivation also reduces the number of gap states produced by broken dimer type defects.

As mentioned in Chapter 3, P_{b0} defects are the only defect clearly identified and assigned experimentally. We only observe one such defect in our structures. It lies in the second Si monolayer from the interface and produces two states near the bulk Si VBM and CBM regions. Adding a passivating hydrogen on the P_{b0} defect results in the removal of these gap states. Experimental data by Stathis *et al* [18] shows that hydrogen passivation is only partially effective against P_{b0} defects. As we only observed one such defect in our structures we cannot determine how different atomic structures found in the vicinity of the defect could affect the hydrogen passivation process. The second most observed defect in experiments on (001)Si/SiO_2 interfaces are P_{b1} type defects, however a clear description of them is lacking. Based on the EPR results of Stesmans *et al* [62] Stirling and co-workers [92] presented a model for the P_{b1} defect. We have not identified any P_{b1} defects such as the ones described by Stirling and co-workers. Such P_{b1} defects could be an effect of special conditions during the oxide deposition process.

We calculated the isotropic hyperfine A_0 values for the Si/SiO_2 defects. E' defects from the amorphous SiO_2 layer presented values up to 70 mT. Broken dimer defects also showed significant isotropic hyperfine A_0 terms that went up to 20 mT. Si dangling bonds on (2×1) (001)Si dimer reconstructions had isotropic hyperfine terms going up to 15 mT. To the best of our knowledge

Si dimer dangling bonds and Si broken dimer type structures have not been clearly identified in (001)Si/SiO_2 interfaces. Given that the gap states created by dimer and broken dimer type defects can be handily eliminated through hydrogen passivation, such defects could be easily overlooked when simply mapping the defects that create localised states in passified structures. Given the recent focus on near bias temperature instability and the likely influence of proton exchange between passified defects at the (001)Si surface and E' defects from the bulk layers of the gate oxide [80] it is quite likely that defects such as dimer defects and broken dimer defects we observed could significantly influence such processes. As Si dimer defects appeared during the PBE-level relaxation, and the (2×1) (001)Si dimer reconstruction is well known to appear on clean surfaces it is quite likely that both dimer defects and broken dimer defects will appear at the interface between (001)Si surfaces and amorphous SiO_2, provided the atomic deposition process does not prohibit the formation of such defects.

Identifying defects in Si/HfO_2 interface structures required a slightly different approach from the one taken for Si/SiO_2 interfaces. Hf atoms in amorphous HfO_2 do not tend to form clearly identifiable tetrahedra and the Hf atoms can have a wider range of coordination numbers. EPR experiments to date have not yet identified clear atomic structures for defects in HfO_2 [111] and studies of defects at silicon-hafnia interfaces are affected by the formation on interfacial SiO_x layers — resulting in the observation of P_b-type defects [105]. For each Hf atom in our structures we calculated the number of O, Hf and Si atoms found within a 3 Å distance and the gap states created by such atoms. A sixfold O coordination was found to be the most common coordination in the Si/HfO_2 structures, while our bulk amorphous Si/HfO_2 structure had more sevenfold and eightfold coordinated Hf atoms. While fourfold and fivefold O coordinations for Hf atoms in the Si/HfO_2 structures were way more likely to produce gap states than other Hf-O coordinations present in our structures, sixfold O coordinated Hf atoms produced the bulk of the gap states, as they appeared more frequently in our structures than all other O coordinations for Hf atoms. Such sixfold coordinated Hf atoms do not produce any gap states in our bulk amorphous HfO_2 structure. However, Hf atoms in bulk HfO_2 tend not to have any neighbouring Hf atoms in their 3 Å coordination sphere. Sixfold O coordinated Hf atoms that create states in the Si/HfO_2 gap above the average of sevenfold and eightfold O coordinated Hf atoms are found to be more likely to have Hf neighbours within the 3 Å coordination shell. This leads us to conclude that an O rich

environment would increase the average Hf coordination number in the HfO_2 layers and result in a cleaning of the Si/HfO_2 gap.

Calculating the isotropic hyperfine A_0 values for Hf defects in Si/HfO_2 interface structures was not possible due to the use of a pseudopotential to describe the Hf core electrons. Si atoms in the interface monolayers of the semiconductor were significantly less likely to have large Fermi contact terms than the dangling bond Si defects identified in the Si/SiO_2 interfaces. One single Si dangling bond had an isotropic hyperfine A_0 value > 5 mT — a Si bonded to two substrate Si atoms and one oxygen from the oxide, namely a broken dimer type defect such as the ones identified in the Si/SiO_2 structures.

As presented in Chapters 3 and 4, *ab initio* calculations on Si/SiO_2, Si/HfO_2 and $Si/SiO_2/HfO_2$ stacks have been performed in the past, some of them even using hybrid functionals that do not underestimate the band gap of insulating materials unlike pure DFT functionals. Such studies generally focused on determining valence and conduction band offsets, oxygen vacancy and interstitial formation energies, dielectric function calculations and hydrogen bond formation energies throughout the oxide. When analysing defects in Si/SiO_2 and Si/HfO_2 interface structures studies so far focused on creating them after the structures have been generated — most often by removing oxygen atoms from the structures. Analyses on defects emerging naturally during molecular dynamics and DFT optimisations in amorphous structures have mainly focused on bulk amorphous SiO_2 [21, 77, 91]. Our study focuses using such methods in finding defects at Si/SiO_2 and Si/HfO_2 interfaces, and pointing out the effect they have on the band gap of materials.

Our structures have a defect density that is significantly higher than those reported in the available literature. This could be caused by approximations of the charge optimised many body potential used, the relatively small size of the cells which could induce strain in the amorphous layer, or simply the fact that we created the interface structures by manually positioning an amorphous oxide layer on top of (001)Si without taking into account the various interface bonding arrangements that could be formed during an atomic layer deposition process. However, as we were able to identify and analyse the electronic properties of several type of defects, nor was it computationally possible to replicate real life anneal times. And we observed that the location of the gap states for defects varies significantly even for defects of the same type, with no immediate simple correlation

observed between the bond lengths or angles of the defect and its hyperfine isotropic contact terms.

Obviously our Si/SiO_2 and Si/HfO_2 interface structures are simplifications of real life devices, which not only contain dopants such as nitrogen to reduce the number of interface defects, but also are subjected to electrostatic potential differences that can induce charge transfers and local geometry modifications in the amorphous oxides. The highly varying degree to which such defects act as charge traps in real life devices [76] mirrors the variability in the observed position of the gap states in our simulated structures.

Clearly, a detailed atom-resolved picture of the bonding patterns at Si/SiO_2 and Si/HfO_2 interfaces has yet to emerge, but a good understanding of these interfaces becomes more crucial as Si/HfO_2 structures with no intermediate silica layer are created [116] and the interfaces themselves become more complicated as the planar interface structure of transistors is abandoned [11, 12]. Perhaps ironically, better future transistor interfaces will provide the computational power needed to simulate larger scale interfaces which would allow for a better description of the electronic properties of intrinsic point defects in Si/SiO_2 and Si/HfO_2 interfaces. While DFT methods are known to be reliable in computing structural parameters, they are somewhat limited in optimising the far from equilibrium structures. This would require either an improvement of the already complex molecular dynamics potentials that can at least describe semiconductor interfaces accurately or in finding numerical optimisations to speed up costly *ab initio* molecular dynamics calculations. A clear and valid theoretical model for simulations of the oxide growth on semiconductor surfaces is needed to determine the bonding patterns of such interfaces. While such tentative studies exist [89, 174] a clear model that would also reproduce the interface defect densities has not yet been agreed upon.

Ultimately all theoretical models require an experimental confirmation. Perhaps advances in X-ray crystallography [175] will provide an experimental technique of mapping the in depth profile of Si/SiO_2 and Si/HfO_2 interface defects or advances in EPR techniques will yield a better resolution picture of the gap defect states and their precise hyperfine axes and g-tensors.

Meanwhile, we hope that the methods and results presented in this thesis will provide the basis

for further studies on interfaces between a crystalline semiconductor and amorphous oxides.

Bibliography

[1] J. Bardeen and W. H. Brattain. The Transistor, A Semi-Conductor Triode. *Phys. Rev.*, 74:230–231, Jul 1948.

[2] R.F. Pierret. *Semiconductor Device Fundamentals*. Addison-Wesley, 1996.

[3] D.A. Neamen. *Electronic circuit analysis and design*. McGraw-Hill, 2001.

[4] Gordon E. Moore. Cramming more components onto integrated circuits. *Electronics*, 38(8), April 1965.

[5] Sokrates T Pantelides. The physics of SiO_2 and its interfaces, Yorktown Heights, New York. In *Proceedings of the International Topical Conference on the Physics of SiO_2 and Its Interfaces Held at the IBM*, March 1978.

[6] John Robertson. High dielectric constant gate oxides for metal oxide Si transistors. *Reports on Progress in Physics*, 69(2):327–396, February 2006.

[7] P. Bai, C. Auth, S. Balakrishnan, M. Bost, R. Brain, V. Chikarmane, R. Heussner, M. Hussein, J. Hwang, D. Ingerly, R. James, J. Jeong, C. Kenyon, E. Lee, S.-H. Lee, N. Lindert, M. Liu, Z. Ma, T. Marieb, A. Murthy, R. Nagisetty, S. Natarajan, J. Neirynck, A. Ott, C. Parker, J. Sebastian, R. Shaheed, S. Sivakumar, J. Steigerwald, S. Tyagi, C. Weber, B. Woolery, A. Yeoh, K. Zhang, and M. Bohr. A 65nm logic technology featuring 35nm gate lengths, enhanced channel strain, 8 Cu interconnect layers, low-k ILD and 0.57 μm^2 SRAM cell. In *Electron Devices Meeting, 2004. IEDM Technical Digest. IEEE International*, pages 657–660, December 2004.

[8] G. D. Wilk, R. M. Wallace, and J. M. Anthony. High-k gate dielectrics: Current status and materials properties considerations. *Journal of Applied Physics*, 89(10):5243–5275, May 2001.

[9] M.T. Bohr, R.S. Chau, T. Ghani, and K. Mistry. The High-k Solution. *IEEE Spectrum*, 44(10):29–35, October 2007.

[10] Robert Chau, Brian Doyle, Suman Datta, Jack Kavalieros, and Kevin Zhang. Integrated nanoelectronics for the future. *Nature Materials*, 6(11):810–812, November 2007.

[11] Satish Damaraju, Varghese George, Sanjeev Jahagirdar, Tanveer Khondker, Robert Milstrey, Sanjib Sarkar, Scott Siers, Israel Stolero, and Arun Subbiah. *A 22nm IA multi-CPU and GPU System-on-Chip*, volume 44, pages 56–57. IEEE, 2012.

[12] A. Nalamalpu, N. Kurd, A. Deval, C. Mozak, J. Douglas, A. Khanna, F. Paillet, G. Schrom, and B. Phelps. Broadwell: A family of IA 14nm processors. In *2015 Symposium on VLSI Circuits (VLSI Circuits)*, pages C314–C315, June 2015.

[13] P. M. Lenahan and J. F. Conley Jr. What can electron paramagnetic resonance tell us about the Si/SiO_2 system? *Journal of Vacuum Science & Technology B*, 16(4):2134–2153, July 1998.

[14] H. Zhu, C. Tang, L. R. C. Fonseca, and R. Ramprasad. Recent progress in ab initio simulations of hafnia-based gate stacks. *Journal of Materials Science*, 47(21):7399–7416, May 2012.

[15] Susan B. Sinnott and Donald W. Brenner. Three decades of many-body potentials in materials research. *MRS Bulletin*, 37:469–473, 4 2012.

[16] P. Hohenberg and W. Kohn. Inhomogeneous electron gas. *Phys. Rev.*, 136:B864–B871, Nov 1964.

[17] W. Kohn and L. J. Sham. Self-consistent equations including exchange and correlation effects. *Phys. Rev.*, 140:A1133–A1138, Nov 1965.

[18] J. H. Stathis and E. Cartier. Atomic hydrogen reactions with P_b centers at the (100) Si/SiO_2 interface. *Physical Review Letters*, 72(17):2745–2748, April 1994.

[19] J. H. Stathis. Electrically detected magnetic resonance study of stress induced leakage current in thin SiO_2. *Applied Physics Letters*, 68(12):1669–1671, March 1996.

[20] J. H. Stathis and S. Zafar. The negative bias temperature instability in MOS devices: A review. *Microelectronics Reliability*, 46(2–4):270–286, February 2006.

[21] Luigi Giacomazzi, L. Martin-Samos, A. Boukenter, Y. Ouerdane, S. Girard, and N Richard. EPR parameters of E' centers in v$-SiO_2$ from first-principles calculations. *Physical Review B*, 90(1):014108, July 2014.

[22] Steve Plimpton. Fast Parallel Algorithms for Short-Range Molecular Dynamics. *Journal of Computational Physics*, 117(1):1–19, March 1995.

[23] Stewart J. Clark, Matthew D. Segall, Chris J. Pickard, Phil J. Hasnip, Matt I. J. Probert, Keith Refson, and Mike C. Payne. First principles methods using CASTEP. *Zeitschrift für Kristallographie*, 220(5/6/2005):567–570, May 2005.

[24] Roberto Dovesi, Bartolomeo Civalleri, Carla Roetti, Victor R. Saunders, and Roberto Orlando. *Ab Initio Quantum Simulation in Solid State Chemistry*, pages 1–125. John Wiley & Sons, Inc., 2005.

[25] Charles H Patterson. Exciton: a code for excitations in materials. *Molecular Physics*, 108(21-23):3181–3188, 2010.

[26] Mike P Allen and Dominic J Tildesley. *Computer simulation of liquids*. Oxford university press, 1989.

[27] Loup Verlet. Computer "experiments" on classical fluids. I. thermodynamical properties of lennard-jones molecules. *Phys. Rev.*, 159:98–103, Jul 1967.

[28] C.W. Gear. *Numerical initial value problems in ordinary differential equations*. Prentice-Hall series in automatic computation. Prentice-Hall, 1971.

[29] Shuichi Nose. A unified formulation of the constant temperature molecular dynamics methods. *The Journal of Chemical Physics*, 81(1):511–519, 1984.

[30] William G. Hoover. Canonical dynamics: Equilibrium phase-space distributions. *Phys. Rev. A*, 31:1695–1697, Mar 1985.

[31] Glenn J Martyna, Douglas J Tobias, and Michael L Klein. Constant pressure molecular dynamics algorithms. *The Journal of Chemical Physics*, 101:4177, 1994.

[32] Steven J. Plimpton and Aidan P. Thompson. Computational aspects of many-body potentials. *MRS Bulletin*, 37:513–521, 4 2012.

[33] Yun Kyung Shin, Tzu-Ray Shan, Tao Liang, Mark J. Noordhoek, Susan B. Sinnott, Adri C.T. van Duin, and Simon R. Phillpot. Variable charge many-body interatomic potentials. *MRS Bulletin*, 37:504–512, 4 2012.

[34] Frank H. Stillinger and Thomas A. Weber. Computer simulation of local order in condensed phases of silicon. *Phys. Rev. B*, 31:5262–5271, Apr 1985.

[35] J. Tersoff. Empirical interatomic potential for silicon with improved elastic properties. *Phys. Rev. B*, 38:9902–9905, Nov 1988.

[36] Akio Yasukawa. Using an extended Tersoff interatomic potential to analyze the static-fatigue strength of SiO_2 under atmospheric influence. *JSME International Journal. Series A, Mechanics and Material Engineering*, 39(3):313–320, 1996.

[37] Jianguo Yu, Susan Sinnott, and Simon Phillpot. Charge optimized many-body potential for the si/SiO2 system. *Physical Review B*, 75(8):085311, February 2007.

[38] Tzu-Ray Shan, Bryce D. Devine, Travis W. Kemper, Susan B. Sinnott, and Simon R. Phillpot. Charge-optimized many-body potential for the hafnium/hafnium oxide system. *Physical Review B*, 81(12):125328, March 2010.

[39] Tzu-Ray Shan, Bryce D. Devine, Jeffery M. Hawkins, Aravind Asthagiri, Simon R. Phillpot, and Susan B. Sinnott. Second-generation charge-optimized many-body potential for Si/SiO_2 and amorphous silica. *Physical Review B*, 82(23):235302, December 2010.

[40] D. Wolf, P. Keblinski, S. R. Phillpot, and J. Eggebrecht. Exact method for the simulation of coulombic systems by spherically truncated, pairwise r^{-1} summation. *The Journal of Chemical Physics*, 110(17):8254–8282, 1999.

[41] Richard M. Martin. *Electronic Structure: Basic Theory and Practical Methods (Vol 1)*. Cambridge University Press, April 2004.

[42] D. Sholl and J.A. Steckel. *Density Functional Theory: A Practical Introduction*. Wiley, 2011.

[43] J. C. Slater. The theory of complex spectra. *Phys. Rev.*, 34:1293–1322, Nov 1929.

[44] Fabien Tran, Robert Laskowski, Peter Blaha, and Karlheinz Schwarz. Performance on molecules, surfaces, and solids of the wu-cohen gga exchange-correlation energy functional. *Phys. Rev. B*, 75:115131, Mar 2007.

[45] John P. Perdew, Matthias Ernzerhof, and Kieron Burke. Rationale for mixing exact exchange with density functional approximations. *The Journal of Chemical Physics*, 105(22):9982–9985, December 1996.

[46] Feliciano Giustino, Angelo Bongiorno, and Alfredo Pasquarello. Atomistic models of the Si(100)–SiO_2 interface: structural, electronic and dielectric properties. *Journal of Physics: Condensed Matter*, 17(21):S2065, June 2005.

[47] Axel D Becke. Density-functional thermochemistry. III. The role of exact exchange. *The Journal of Chemical Physics*, 98(7):5648–5652, 1993.

[48] J. Muscat, A. Wander, and N.M. Harrison. On the prediction of band gaps from hybrid functional theory. *Chemical Physics Letters*, 342(3–4):397 – 401, 2001.

[49] John A Weil and James R Bolton. *Electron paramagnetic resonance: elementary theory and practical applications*. John Wiley & Sons, 2007.

[50] S David Jackson and Justin SJ Hargreaves. *Metal oxide catalysis*. John Wiley & Sons, 2008.

[51] Goran Kovačević and Branko Pivac. Structure, defects, and strain in silicon-silicon oxide interfaces. *Journal of Applied Physics*, 115(4):043531, January 2014.

[52] R. A. Weeks, R. H. Magruder III, and Andre Stesmans. Review of some experiments in the 50 year saga of the E′ center and suggestions for future research. *Journal of Non-Crystalline Solids*, 354(2–9):208–216, January 2008.

[53] Goran Kovačević and Branko Pivac. Modeling the interface between crystalline silicon and silicon oxide polymorphs. *Physica Status Solidi (A)*, 210(4):717–722, April 2013.

[54] G. Hollinger and F. J. Himpsel. Probing the transition layer at the SiO_2-si interface using core level photoemission. *Applied Physics Letters*, 44(1):93–95, January 1984.

[55] F. J. Himpsel, F. R. McFeely, A. Taleb-Ibrahimi, J. A. Yarmoff, and G. Hollinger. Microscopic structure of the SiO_2/Si interface. *Physical Review B*, 38(9):6084–6096, September 1988.

[56] D. A. Muller, T. Sorsch, S. Moccio, F. H. Baumann, K. Evans-Lutterodt, and G. Timp. The electronic structure at the atomic scale of ultrathin gate oxides. *Nature*, 399(6738):758–761, June 1999.

[57] M. L. Green, T. W. Sorsch, G. L. Timp, D. A. Muller, B. E. Weir, P. J. Silverman, S. V. Moccio, and Y. O. Kim. Understanding the limits of ultrathin SiO_2 and SiON gate dielectrics for sub-50 nm CMOS. *Microelectronic Engineering*, 48(1–4):25–30, September 1999.

[58] R. a. B. Devine. Structural nature of the Si/SiO_2 interface through infrared spectroscopy. *Applied Physics Letters*, 68(22):3108–3110, May 1996.

[59] K. T. Queeney, M. K. Weldon, J. P. Chang, Y. J. Chabal, A. B. Gurevich, J. Sapjeta, and R. L. Opila. Infrared spectroscopic analysis of the Si/SiO_2 interface structure of thermally oxidized silicon. *Journal of Applied Physics*, 87(3):1322–1330, February 2000.

[60] W. Daum, H.-J. Krause, U. Reichel, and H. Ibach. Identification of strained silicon layers at Si-SiO_2 interfaces and clean Si surfaces by nonlinear optical spectroscopy. *Physical Review Letters*, 71(8):1234–1237, August 1993.

[61] A. Stesmans and V. V. Afanas'ev. Electron spin resonance features of interface defects in thermal (100)Si/SiO_2. *Journal of Applied Physics*, 83(5):2449–2457, March 1998.

[62] A. Stesmans, B. Nouwen, and V. Afanas'ev. P_{b1} interface defect in thermal (100)Si/SiO_2: ^{29}Si hyperfine interaction. *Physical Review B*, 58(23):15801–15809, December 1998.

[63] Takahiro Yamasaki, Koichi Kato, and Tsuyoshi Uda. Oxidation of the Si(001) Surface: Lateral Growth and Formation of P_{b0} Centers. *Physical Review Letters*, 91(14):146102, October 2003.

[64] R. A. Weeks. Paramagnetic Resonance of Lattice Defects in Irradiated Quartz. *Journal of Applied Physics*, 27(11):1376–1381, November 1956.

[65] G. Buscarino, S. Agnello, and F. M. Gelardi. ^{29}Si Hyperfine Structure of the E' Center in Amorphous Silicon Dioxide. *Physical Review Letters*, 97(13):135502, September 2006.

[66] Gianfranco Pacchioni, Linards Skuja, and David Griscom. *Defects in SiO_2 and Related Dielectrics: Science and Technology; [proceedings of the NATO Advanced Study Institute on Defects in SiO_2 and Related Dielectrics: Science and Technolgy, Erice, Italy, April 8-20, 2000]*, volume 2. Springer Science & Business Media, 2000.

[67] J. P. Campbell and P. M. Lenahan. Density of states of P_{b1} Si/SiO_2 interface trap centers. *Applied Physics Letters*, 80(11):1945–1947, March 2002.

[68] Gary J. Gerardi, Edward H. Poindexter, Philip J. Caplan, and Noble M. Johnson. Interface traps and P_b centers in oxidized (100) silicon wafers. *Applied Physics Letters*, 49(6):348–350, August 1986.

[69] A Stesmans and V V Afanas'ev. Undetectability of the P_{b1} point defect as an interface state in thermal (100)Si/SiO_2. *Journal of Physics: Condensed Matter*, 10(1):L19, 1998.

[70] G. Groeseneken, H.E. Maes, N. Beltran, and R.F. De Keersmaecker. A reliable approach to charge-pumping measurements in MOS transistors. *IEEE Transactions on Electron Devices*, 31(1):42–53, January 1984.

[71] Yuegang Zhao. How to get accurate trap density measurements using charge pumping. *Keithley Instruments, March*, 2004.

[72] J. Maserjian and N. Zamani. Behavior of the Si/SiO_2 interface observed by Fowler-Nordheim tunneling. *Journal of Applied Physics*, 53(1):559–567, 1982.

[73] Steven C. Witczak, John S. Suehle, and Michael Gaitan. An experimental comparison of measurement techniques to extract $Si\text{-}SiO_2$ interface trap density. *Solid-State Electronics*, 35(3):345 – 355, 1992.

[74] B. Keramati and J. N. Zemel. Confirmation of hydrogen surface states at the $Si\text{-}SiO_2$ interface. In Sokrates T. Pantelides, editor, *The Physics of SiO2 and its Interfaces*, pages 459–463. Pergamon, 1978.

[75] A. M. Stoneham, J. L. Gavartin, and A. L. Shluger. The oxide gate dielectric: do we know all we should? *Journal of Physics: Condensed Matter*, 17(21):S2027, June 2005.

[76] T. Grasser, M. Wahl, W. Goes, Y. Wimmer, A.-M. El-Sayed, A.L. Shluger, and B. Kaczer. On the volatility of oxide defects: Activation, deactivation, and transformation. In *Reliability Physics Symposium (IRPS), 2015 IEEE International*, pages 5A.3.1–5A.3.8, April 2015.

[77] Al-Moatasem El-Sayed, Yannick Wimmer, Wolfgang Goes, Tibor Grasser, Valery V. Afanas'ev, and Alexander L. Shluger. Theoretical models of hydrogen-induced defects in amorphous silicon dioxide. *Physical Review B*, 92(1):014107, July 2015.

[78] A. Stesmans. Passivation of pb0 and pb1 interface defects in thermal (100) si/sio2 with molecular hydrogen. *Applied Physics Letters*, 68(15):2076–2078, Apr 1996.

[79] Hao Jin, K. J. Weber, N. C. Dang, and W. E. Jellett. Defect generation at the Si–SiO2 interface following corona charging. *Applied Physics Letters*, 90(26):262109, June 2007.

[80] Dieter K. Schroder. Negative bias temperature instability: What do we understand? *Microelectronics Reliability*, 47(6):841–852, June 2007.

[81] J.P. Campbell, P.M. Lenahan, A.T. Krishnan, and Srikanth Krishnan. Observations of nbti-induced atomic-scale defects. *Device and Materials Reliability, IEEE Transactions on*, 6(2):117–122, June 2006.

[82] T. Grasser, B. Kaczer, W. Goes, T. Aichinger, P. Hehenberger, and M. Nelhiebel. A two-stage model for negative bias temperature instability. In *Reliability Physics Symposium, 2009 IEEE International*, pages 33–44, April 2009.

[83] J. T. Ryan, P. M. Lenahan, T. Grasser, and H. Enichlmair. Observations of negative bias temperature instability defect generation via on the fly electron spin resonance. *Applied Physics Letters*, 96(22):–, 2010.

[84] Iwao Ohdomari, Hiroyuki Akatsu, Yukio Yamakoshi, and Koji Kishimoto. Study of the interfacial structure between si (100) and thermally grown SiO_2 using a ball-and-spoke model. *Journal of Applied Physics*, 62(9):3751–3754, November 1987.

[85] Alfredo Pasquarello, Mark S. Hybertsen, and Roberto Car. Interface structure between silicon and its oxide by first-principles molecular dynamics. *Nature*, 396(6706):58–60, November 1998.

[86] Ryszard Buczko, Stephen Pennycook, and Sokrates Pantelides. Bonding arrangements at the si-SiO_2 and SiC-SiO_2 interfaces and a possible origin of their contrasting properties. *Physical Review Letters*, 84(5):943–946, January 2000.

[87] Alejandra B. Gurevich, Boris B. Stefanov, Marcus K. Weldon, Yves J. Chabal, and Krishnan Raghavachari. Heterogeneous nucleation of oxygen on silicon: Hydroxyl-mediated interdimer coupling on Si(100)-2x1. *Physical Review B*, 58(20):R13434–R13437, November 1998.

[88] Katsuhiro Kutsuki, Tomoya Ono, and Kikuji Hirose. First-principles study on electronic structure of Si/SiO_2 interface—effect of interface defects on local charge density. *Science and Technology of Advanced Materials*, 8(3):204 – 207, 2007.

[89] A. Hemeryck, A. J. Mayne, N. Richard, A. Estève, Y. J. Chabal, M. Djafari Rouhani, G. Dujardin, and G. Comtet. Difficulty for oxygen to incorporate into the silicon network during initial O_2 oxidation of Si(100)-(2x1). *The Journal of Chemical Physics*, 126(11):114707, mar 2007.

[90] Mauro Boero, Alfredo Pasquarello, Johannes Sarnthein, and Roberto Car. Structure and

Hyperfine Parameters of E' Centers in Quartz and in Vitreous SiO_2. *Physical Review Letters*, 78(5):887–890, February 1997.

[91] Mauro Boero, Atsushi Oshiyama, and Pier Luigi Silvestrelli. E' Centers in alpha Quartz in the Absence of Oxygen Vacancies: A First-Principles Molecular-Dynamics Study. *Physical Review Letters*, 91(20):206401, November 2003.

[92] András Stirling, Alfredo Pasquarello, J.-C. Charlier, and Roberto Car. Dangling bond defects at Si-SiO_2 interfaces: Atomic structure of the P_{b1} center. *Physical Review Letters*, 85(13):2773–2776, September 2000.

[93] J. Neaton, D. Muller, and N. Ashcroft. Electronic Properties of the Si/SiO_2 Interface from First Principles. *Physical Review Letters*, 85(6):1298–1301, August 2000.

[94] Pierre Carrier, Laurent Lewis, and M. Dharma-wardana. Optical properties of structurally relaxed Si/SiO_2 superlattices: The role of bonding at interfaces. *Physical Review B*, 65(16):165339, April 2002.

[95] Feliciano Giustino, Angelo Bongiorno, and Alfredo Pasquarello. Atomistic models of the Si(100)–SiO_2 interface: structural, electronic and dielectric properties. *Journal of Physics: Condensed Matter*, 17(21):S2065, 2005.

[96] Sanliang Ling, Al-Moatasem El-Sayed, Francisco Lopez-Gejo, Matthew B. Watkins, V.V. Afanas'ev, and Alexander L. Shluger. A computational study of Si-H bonds as precursors for neutral centres in amorphous silica and at the Si/SiO_2 interface. *Microelectronic Engineering*, 109(0):310 – 313, 2013. Insulating Films on Semiconductors 2013.

[97] Adri CT Van Duin, Alejandro Strachan, Shannon Stewman, Qingsong Zhang, Xin Xu, and William A Goddard. ReaxFFSiO reactive force field for silicon and silicon oxide systems. *The Journal of Physical Chemistry A*, 107(19):3803–3811, 2003.

[98] L. Tsetseris and S. Pantelides. Migration, incorporation, and passivation reactions of molecular hydrogen at the Si-SiO_2 interface. *Physical Review B*, 70(24):245320, December 2004.

[99] J. Robertson. High dielectric constant oxides. *The European Physical Journal Applied Physics*, 28(3):265–291, December 2004.

[100] Onise Sharia, Alexander A Demkov, Gennadi Bersuker, and Byoung Hun Lee. Theoretical study of the insulator/insulator interface: Band alignment at the SiO_2/HfO_2 junction. *Physical Review B*, 75(3):035306, 2007.

[101] R. Rios and N.D. Arora. Determination of ultra-thin gate oxide thicknesses for CMOS structures using quantum effects. In *Electron Devices Meeting, 1994. IEDM '94. Technical Digest., International*, pages 613–616, December 1994.

[102] H. R. Huff, A. Hou, C. Lim, Y. Kim, J. Barnett, G. Bersuker, G. A. Brown, C. D. Young, P. M. Zeitzoff, J. Gutt, P. Lysaght, M. I. Gardner, and R. W. Murto. High-k gate stacks for planar, scaled CMOS integrated circuits. *Microelectronic Engineering*, 69(2–4):152–167, September 2003.

[103] K. Mistry, C. Allen, C. Auth, B. Beattie, D. Bergstrom, M. Bost, M. Brazier, M. Buehler, A. Cappellani, R. Chau, C.-H. Choi, G. Ding, K. Fischer, T. Ghani, R. Grover, W. Han, D. Hanken, M. Hattendorf, J. He, J. Hicks, R. Huessner, D. Ingerly, P. Jain, R. James, L. Jong, S. Joshi, C. Kenyon, K. Kuhn, K. Lee, H. Liu, J. Maiz, B. Mcintyre, P. Moon, J. Neirynck, S. Pae, C. Parker, D. Parsons, C. Prasad, L. Pipes, M. Prince, P. Ranade, T. Reynolds, J. Sandford, L. Shifren, J. Sebastian, J. Seiple, D. Simon, S. Sivakumar, P. Smith, C. Thomas, T. Troeger, P. Vandervoorn, S. Williams, and K. Zawadzki. A 45nm Logic Technology with High-k+Metal Gate Transistors, Strained Silicon, 9 Cu Interconnect Layers, 193nm Dry Patterning, and 100% Pb-free Packaging. In *Electron Devices Meeting, 2007. IEDM 2007. IEEE International*, pages 247–250, December 2007.

[104] V. V. Afanas'ev, A. Stesmans, F. Chen, X. Shi, and S. A. Campbell. Internal photoemission of electrons and holes from (100)Si into HfO_2. *Applied Physics Letters*, 81(6):1053–1055, August 2002.

[105] A. Stesmans and V.V. Afanasev. Si dangling-bond-type defects at the interface of (100)Si with ultrathin HfO_2. *Applied Physics Letters*, 82(23):4074–4076, June 2003.

[106] Y. G. Fedorenko, L. Truong, V. V. Afanas'ev, and A. Stesmans. Interface state energy distribution in (100)Si/HfO_2. *Materials Science in Semiconductor Processing*, 7(4–6):185–189, 2004.

[107] K. Choi, H. Temkin, H. Harris, S. Gangopadhyay, L. Xie, and M. White. Initial growth of interfacial oxide during deposition of HfO_2 on silicon. *Applied Physics Letters*, 85(2):215–217, July 2004.

[108] Ragesh Puthenkovilakam and Jane P. Chang. An accurate determination of barrier heights at the HfO_2/Si interfaces. *Journal of Applied Physics*, 96(5):2701–2707, September 2004.

[109] M. Modreanu, J. Sancho-Parramon, O. Durand, B. Servet, M. Stchakovsky, C. Eypert, C. Naudin, A. Knowles, F. Bridou, and M.-F. Ravet. Investigation of thermal annealing effects on microstructural and optical properties of HfO_2 thin films. *Applied Surface Science*, 253(1):328 – 334, 2006.

[110] A. Y. Kang, P. M. Lenahan, and J. F. Conley Jr. Electron spin resonance observation of trapped electron centers in atomic-layer-deposited hafnium oxide on Si. *Applied Physics Letters*, 83(16):3407–3409, October 2003.

[111] Sandra Wright and R. C. Barklie. EPR characterization of defects in m-HfO_2. *Journal of Materials Science: Materials in Electronics*, 18(7):743–746, February 2007.

[112] K. Cherkaoui, S. Monaghan, M. A. Negara, M. Modreanu, P. K. Hurley, D. O'Connell, S. McDonnell, G. Hughes, S. Wright, R. C. Barklie, P. Bailey, and T. C. Q. Noakes. Electrical, structural, and chemical properties of HfO_2 films formed by electron beam evaporation. *Journal of Applied Physics*, 104(6):064113, September 2008.

[113] E. Bersch, M. Di, S. Consiglio, R. D. Clark, G. J. Leusink, and A. C. Diebold. Complete band offset characterization of the HfO_2/SiO_2/Si stack using charge corrected X-ray photoelectron spectroscopy. *Journal of Applied Physics*, 107(4):043702, February 2010.

[114] Xiaolei Wang, Kai Han, Wenwu Wang, Jinjuan Xiang, Hong Yang, Jing Zhang, Xueli Ma, Chao Zhao, Dapeng Chen, and Tianchun Ye. Band alignment of HfO_2 on SiO_2/Si structure. *Applied Physics Letters*, 100(12):122907, March 2012.

[115] Xiuyan Li, Takeaki Yajima, Tomonori Nishimura, and Akira Toriumi. Study of Si kinetics in interfacial SiO_2 scavenging in HfO_2 gate stacks. *Applied Physics Express*, 8(6):061304, June 2015.

[116] P.C. Jamison, T. Tsunoda, Tuan Anh Vo, Juntao Li, H. Jagannathan, S.R. Shinde, V.K. Paruchuri, and D. Gall. SiO_2 Free HfO_2 Gate Dielectrics by Physical Vapor Deposition. *IEEE Transactions on Electron Devices*, 62(9):2878–2882, September 2015.

[117] A. S. Foster, F. Lopez Gejo, A. L. Shluger, and R. M. Nieminen. Vacancy and interstitial defects in hafnia. *Physical Review B*, 65(17):174117, May 2002.

[118] K. Xiong, J. Robertson, M. C. Gibson, and S. J. Clark. Defect energy levels in HfO_2 high-dielectric-constant gate oxide. *Applied Physics Letters*, 87(18):183505, October 2005.

[119] D. Muñoz Ramo, J. L. Gavartin, A. L. Shluger, and G. Bersuker. Spectroscopic properties of oxygen vacancies in monoclinic HfO_2 calculated with periodic and embedded cluster density functional theory. *Physical Review B*, 75(20):205336, May 2007.

[120] Peter Broqvist and Alfredo Pasquarello. Oxygen vacancy in monoclinic HfO_2: A consistent interpretation of trap assisted conduction, direct electron injection, and optical absorption experiments. *Applied Physics Letters*, 89(26):262904, December 2006.

[121] Rui Wu, Bo Zhou, Qian Li, ZhenYi Jiang, WenBo Wang, WenYan Ma, and XiaoDong Zhang. Elastic and vibrational properties of monoclinic HfO_2 from first-principles study. *Journal of Physics D: Applied Physics*, 45(12):125304, 2012.

[122] C. Kaneta and T. Yamasaki. Oxygen-related defects in amorphous HfO_2 gate dielectrics. *Microelectronic Engineering*, 84(9–10):2370–2373, September 2007.

[123] Wanderlei. Scopel, Antônio J. R. da Silva, and A. Fazzio. Amorphous HfO_2 and $Hf_{1-x}Si_xO$ via a melt-and-quench scheme using ab initio molecular dynamics. *Physical Review B*, 77(17):172101, May 2008.

[124] Tsung-Ju Chen and Chin-Lung Kuo. First principles study of the structural, electronic, and dielectric properties of amorphous HfO_2. *Journal of Applied Physics*, 110(6):064105, September 2011.

[125] G. Broglia, G. Ori, L. Larcher, and M. Montorsi. Molecular dynamics simulation of amorphous HfO_2 for resistive RAM applications. *Modelling and Simulation in Materials Science and Engineering*, 22(6):065006, September 2014.

[126] J. L. Gavartin, L. Fonseca, G. Bersuker, and A. L Shluger. Ab initio modeling of structure and defects at the HfO_2/Si interface. *Microelectronic Engineering*, 80:412–415, June 2005.

[127] P. W. Peacock, K. Xiong, K. Tse, and J. Robertson. Bonding and interface states of Si:HfO_2 and Si:ZrO_2 interfaces. *Physical Review B*, 73(7):075328, February 2006.

[128] M. H. Hakala, A. S. Foster, J. L. Gavartin, P. Havu, M. J. Puska, and R. M. Nieminen. Interfacial oxide growth at silicon/high-k oxide interfaces: First principles modeling of the Si–HfO_2 interface. *Journal of Applied Physics*, 100(4):043708, August 2006.

[129] J. L. Gavartin and A. L. Shluger. Modeling the HfO_2/SiO_2/Si interface. *Microelectronic Engineering*, 84(9–10):2412–2415, September 2007.

[130] Julien Godet, Peter Broqvist, and Alfredo Pasquarello. Hydrogen in Si(100)/SiO_2/HfO_2 gate stacks: Relevant charge states and their location. *Applied Physics Letters*, 91(26):262901–262901–3, December 2007.

[131] C. Tang and R. Ramprasad. Oxygen defect accumulation at Si:HfO_2 interfaces. *Applied Physics Letters*, 92(18):182908, May 2008.

[132] Byungki Ryu and K. J. Chang. Defects responsible for the Fermi level pinning in n+ poly-Si/HfO_2 gate stacks. *Applied Physics Letters*, 97(24):242910, December 2010.

[133] Xinyuan Zhao and David Vanderbilt. First-principles study of structural, vibrational, and lattice dielectric properties of hafnium oxide. *Phys. Rev. B*, 65:233106, Jun 2002.

[134] Hannu-Pekka Komsa, Peter Broqvist, and Alfredo Pasquarello. Alignment of defect levels and band edges through hybrid functionals: Effect of screening in the exchange term. *Phys. Rev. B*, 81:205118, May 2010.

[135] Marie C. Cheynet, Simone Pokrant, Frans D. Tichelaar, and Jean-Luc Rouviere. Crystal structure and band gap determination of HfO_2 thin films. *Journal of Applied Physics*, 101(5):054101, 2007.

[136] John P. Perdew, Adrienn Ruzsinszky, Lucian A. Constantin, Jianwei Sun, and Gábor I. Csonka. Some fundamental issues in ground-state density functional theory: A guide for

the perplexed. *Journal of Chemical Theory and Computation*, 5(4):902–908, 2009. PMID: 26609599.

[137] Manish Jain, James R. Chelikowsky, and Steven G. Louie. Reliability of Hybrid Functionals in Predicting Band Gaps. *Physical Review Letters*, 107(21):216806, November 2011.

[138] Fabien Pascale, Claudio M. Zicovich-Wilson, Roberto Orlando, Carla Roetti, Piero Ugliengo, and Roberto Dovesi. Vibration Frequencies of $Mg_3Al_2Si_3O_12$ Pyrope. An ab Initio Study with the CRYSTAL Code. *The Journal of Physical Chemistry B*, 109(13):6146–6152, April 2005.

[139] Hendrik J. Monkhorst and James D. Pack. Special points for Brillouin-zone integrations. *Physical Review B*, 13(12):5188–5192, June 1976.

[140] Leslie Ernest Sutton. *Tables of Interatomic Distances and Configuration in Molecules and Ions: Supplement 1956-59*. Number 18. Chemical Society, 1965.

[141] Ben G Streetman and Sanjay Banerjee. *Solid state electronic devices*. Upper Saddle River, N.J. : Prentice Hall, 5th ed edition, 2000. Includes bibliographical references and index.

[142] M. D. Towler, N. L. Allan, N. M. Harrison, V. R. Saunders, W. C. Mackrodt, and E. Aprà. Ab initio study of MnO and NiO. *Physical Review B*, 50(8):5041–5054, August 1994.

[143] Egon Wiberg, Nils Wiberg, and b. 1859. Lehrbuch der anorganische Chemie Holleman, A. F. (Arnold Frederick). *Inorganic chemistry*. San Diego : Academic Press ; Berlin ; New York : De Gruyter, 1st english ed. / [edited] by nils wiberg edition, 2001.

[144] David R Lide. *CRC handbook of chemistry and physics*. CRC press, 2004.

[145] Laurence AJ Garvie, Peter Rez, Jose R Alvarez, Peter R Buseck, Alan J Craven, and Rik Brydson. Bonding in alpha-quartz (SiO_2): A view of the unoccupied states. *American Mineralogist*, 85(5-6):732–738, 2000.

[146] Adrian C. Wright. Neutron scattering from vitreous silica. V. The structure of vitreous silica: What have we learned from 60 years of diffraction studies? *Journal of Non-Crystalline Solids*, 179:84–115, November 1994.

[147] Z. A. Weinberg, G. W. Rubloff, and E. Bassous. Transmission, photoconductivity, and the experimental band gap of thermally grown SiO_2 films. *Physical Review B*, 19(6):3107–3117, March 1979.

[148] J. Wang, H. P. Li, and R. Stevens. Hafnia and hafnia-toughened ceramics. *Journal of Materials Science*, 27(20):5397–5430, January 1992.

[149] Detlev Figgen, Kirk A. Peterson, Michael Dolg, and Hermann Stoll. Energy-consistent pseudopotentials and correlation consistent basis sets for the 5d elements Hf–Pt. *The Journal of Chemical Physics*, 130(16):164108, April 2009.

[150] Peter Broqvist and Alfredo Pasquarello. Band gaps and dielectric constants of amorphous hafnium silicates: A first-principles investigation. *Applied Physics Letters*, 90(8):082907, February 2007.

[151] P. Jeffrey Hay and Willard R. Wadt. Ab initio effective core potentials for molecular calculations. Potentials for the transition metal atoms Sc to Hg. *The Journal of Chemical Physics*, 82(1):270–283, January 1985.

[152] Davide Ceresoli and David Vanderbilt. Structural and dielectric properties of amorphous ZrO_2 and HfO_2. *Phys. Rev. B*, 74:125108, Sep 2006.

[153] JL Lyons, A. Janotti, and CG Van de Walle. The role of oxygen-related defects and hydrogen impurities in HfO_2 and ZrO_2. *Microelectronic Engineering*, 2011.

[154] Raiford E. Hann, Paul R. Suitch, and Joseph L. Pentecost. Monoclinic crystal structures of ZrO_2 and HfO_2 refined from X-ray powder diffraction data. *Journal of the American Ceramic Society*, 68(10):C–285–C–286, 1985.

[155] Lorenzo Maschio, Bernard Kirtman, Michel Rérat, Roberto Orlando, and Roberto Dovesi. Ab initio analytical Raman intensities for periodic systems through a coupled perturbed Hartree-Fock/Kohn-Sham method in an atomic orbital basis. II. Validation and comparison with experiments. *The Journal of Chemical Physics*, 139(16):164102, October 2013.

[156] M. Veithen, X. Gonze, and Ph. Ghosez. Nonlinear optical susceptibilities, raman efficiencies, and electro-optic tensors from first-principles density functional perturbation theory. *Phys. Rev. B*, 71:125107, Mar 2005.

[157] Yin Wang, Ferdows Zahid, Jian Wang, and Hong Guo. Structure and dielectric properties of amorphous high-k oxides: HfO_2, ZrO_2, and their alloys. *Physical Review B*, 85(22):224110, June 2012.

[158] T. V. Perevalov, V. A. Gritsenko, S. B. Erenburg, A. M. Badalyan, Hei Wong, and C. W. Kim. Atomic and electronic structure of amorphous and crystalline hafnium oxide: X-ray photoelectron spectroscopy and density functional calculations. *Journal of Applied Physics*, 101(5):053704, March 2007.

[159] Hideki Takeuchi, Daewon Ha, and Tsu-Jae King. Observation of bulk HfO_2 defects by spectroscopic ellipsometry. *Journal of Vacuum Science & Technology A*, 22(4):1337–1341, July 2004.

[160] S. D. Kosowsky, P. S. Pershan, K. S. Krisch, J. Bevk, M. L. Green, D. Brasen, L. C. Feldman, and P. K. Roy. Evidence of annealing effects on a high-density Si/SiO_2 interfacial layer. *Applied Physics Letters*, 70(23):3119–3121, June 1997.

[161] Feliciano Giustino. *Infrared properties of the Si-SiO_2 interface from first principles*. PhD thesis, SB, Lausanne, 2005.

[162] A. Stesmans and V. V. Afanas'ev. Paramagnetic defects at the interface of ultrathin oxides grown under vacuum ultraviolet photon excitation on (111) and (100) Si. *Applied Physics Letters*, 77(10):1469–1471, September 2000.

[163] Eric K. Chang, Michael Rohlfing, and Steven G. Louie. Excitons and Optical Properties of α-Quartz. *Physical Review Letters*, 85(12):2613–2616, September 2000.

[164] Yong-nian Xu and W. Y. Ching. Electronic and optical properties of all polymorphic forms of silicon dioxide. *Physical Review B*, 44(20):11048–11059, November 1991.

[165] C. R. Helms and E. H. Poindexter. The silicon-silicon dioxide system: Its microstructure and imperfections. *Reports on Progress in Physics*, 57(8):791, August 1994.

[166] T. E. Tsai, D. L. Griscom, and E. J. Friebele. Mechanism of Intrinsic Si E'-Center Photogeneration in High-Purity Silica. *Physical Review Letters*, 61(4):444–446, July 1988.

[167] Peter E. Blöchl. First-principles calculations of defects in oxygen-deficient silica exposed to hydrogen. *Physical Review B*, 62(10):6158–6179, September 2000.

[168] J. Ihm, Marvin L. Cohen, and D. J. Chadi. (2 x 1) reconstructed Si(001) surface: Self-consistent calculations of dimer models. *Physical Review B*, 21(10):4592–4599, May 1980.

[169] Davide Colleoni, Giacomo Miceli, and Alfredo Pasquarello. Origin of Fermi-level pinning at GaAs surfaces and interfaces. *Journal of Physics: Condensed Matter*, 26(49):492202, December 2014.

[170] Edward H. Poindexter, Philip J. Caplan, Bruce E. Deal, and Reda R. Razouk. Interface states and electron spin resonance centers in thermally oxidized (111) and (100) silicon wafers. *Journal of Applied Physics*, 52(2):879–884, February 1981.

[171] Koichi Kato, Takahiro Yamasaki, and Tsuyoshi Uda. Origin of p_{b1} center at SiO_2/(001)Si interface: First-principles calculations. *Physical Review B*, 73(7):073302, February 2006.

[172] L.V. Goncharova, M. Dalponte, T. Feng, T. Gustafsson, E. Garfunkel, P.S. Lysaght, and G. Bersuker. Diffusion and interface growth in hafnium oxide and silicate ultrathin films on Si(001). *Physical Review B*, 83(11):115329, March 2011.

[173] S. Ferrari and M. Fanciulli. Diffusion Reaction of Oxygen in HfO_2/SiO_2/Si Stacks. *The Journal of Physical Chemistry B*, 110(30):14905–14910, August 2006.

[174] Maxim Deminsky, Andrei Knizhnik, Ivan Belov, Stanislav Umanskii, Elena Rykova, Alexander Bagatur'yants, Boris Potapkin, Matthew Stoker, and Anatoli Korkin. Mechanism and kinetics of thin zirconium and hafnium oxide film growth in an ALD reactor. *Surface Science*, 549(1):67–86, January 2004.

[175] Jianwei Miao, Tetsuya Ishikawa, Ian K. Robinson, and Margaret M. Murnane. Beyond crystallography: Diffractive imaging using coherent X-ray light sources. *Science*, 348(6234):530–535, 2015.